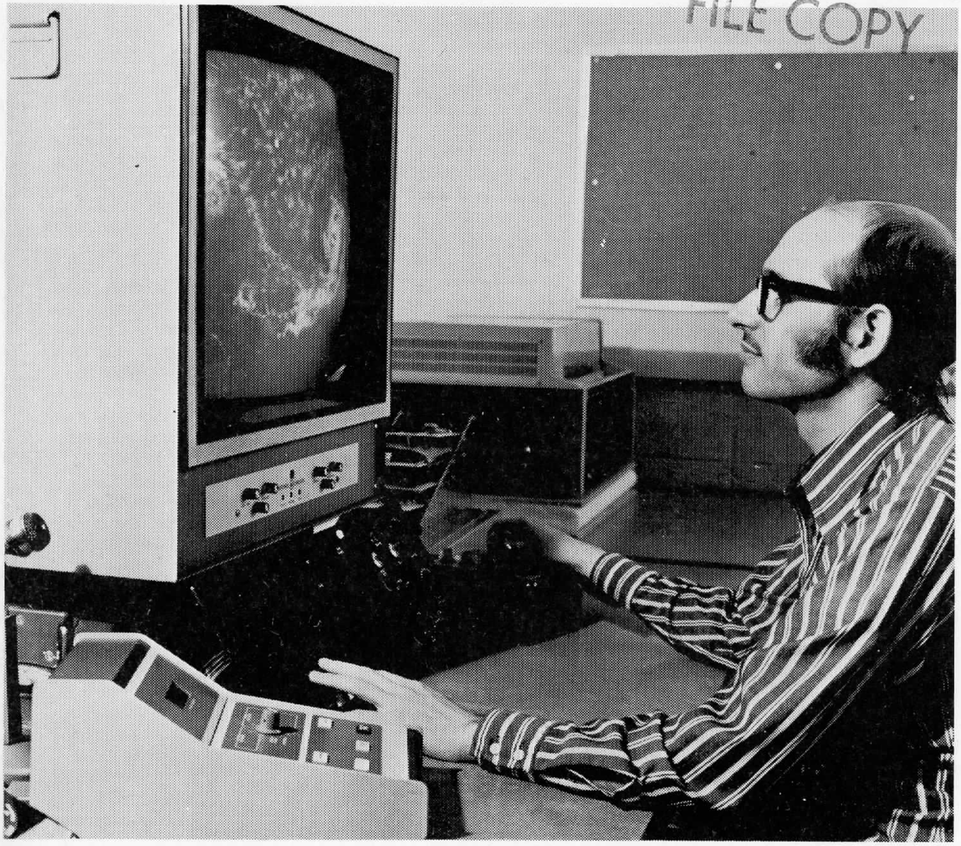

Annual Report
1972

STUDIES OF THE ATMOSPHERE USING AEROSPACE PROBES

Space Science and Engineering Center
University of Wisconsin
Madison, Wisconsin

The Cover Picture

The cover of the report shows the display and control console for a prototype hardware development described in the paper by Terry Schwalenberg. This equipment has successfully demonstrated a means to access image matrix information so that meteorological parameters of interest such as cloud motion, sunglint, cloud dynamics, etc., can be extracted. The fact that the display is a standard TV monitor and that the console is very simple is not accidental. They provide the stimulus and response capabilities that enable a human to interact with, and to control a computer which searches, selects, measures and analyzes the parameters of interest. By maintaining full compatibility with US commercial TV standards, the system also provides exciting growth prospects on an economic and effective basis.

Space Science and Engineering Center
The University of Wisconsin
Madison, Wisconsin

STUDIES OF THE ATMOSPHERE USING AEROSPACE PROBES

Annual Report on

NOAA Grant 1-36036

1972

The research reported in this document has been supported by the
National Oceanic and Atmospheric Administration

December, 1972

Preface

This report contains papers which cover a broad range of topics. The data for these contributions came from many sources not limited to satellites alone. Most of the data were reduced and analyzed laboriously by hand. The WINDCO development described herein will lead directly to a data access and processing system which will greatly reduce the labor involved in future studies of this type.

Again, it is my pleasure to acknowledge the important contributions of these authors and to express for them our gratitude for the support furnished by NOAA.

Table of Contents

Page

The Windco Display System, by Terry Schwalenberg 1

A Filtered View of Fluctuating Cloud Patterns in the Tropical Pacific, by John A. Young and D D. N. Sikdar 16

The Lifetime of Subtropical Convective Clouds Above the Ocean, by Glenn B. Dick 37

Upper Tropospheric Isobaric Temperature and Height Fields over the Tropical Atlantic From Satellite Infrared Spectrometer Soundings, by D. N. Sikdar and R. S. Cram 68

Some Empirical Findings on the Release of Latent Heat in Tropical Cloud Clusters of the Pacific, by D. N. Sikdar 90

A Linear Model of Boundary Layer Airflow During the St. Patrick's Day Storm of 1965, by Richard J. Naistat and John A. Young 102

A Numerical Study of the Pressure Response to Liquid-water Drag in a Three-dimensional Convective System, by Robert Abbey and J. A. Young 140

THE WINDCO DISPLAY SYSTEM

Terry W. Schwalenberg

System Description

The WINDCO display is a system having the capability of converting digital data into standard TV images, storing up to 600 of these images, displaying them in sequence, and indicating the exact coordinates of any data point in terms of the original digital data.

The system utilizes a Raytheon 440 (a small computer) for data formatting and control, an Ampex DR-10 analog disk recorder for TV frame storage and monitor refresh, a standard TV monitor for viewing, a standard electronic TV pointer for flagging data, and a specially designed fast storage unit for doing the necessary time base translation.

The system has two modes of operation. In the load mode, the system under complete control of the computer transfers data from the computer to the analog disk and converts it from digital data to standard 525-line TV frames. In the playback mode, the TV frames are presented to the monitor one at a time, or in sequence at variable rates, under the control of the operator. In this mode the computer is not used.

In addition, the system timing is such that the location of each of the $525 \times 768 \simeq 400{,}000$ pixels of each TV frame is known at all times, with respect to the original digital data loaded from the computer.

It should be emphasized that the WINDCO display generates standard 525-line TV video frames which are stored on the Ampex DR-10 analog disk. These signals are compatible with the TV industry and can be put on the air through any TV station.

The TV compatibility also allows for the use of the standard line of video instrumentation hardware which exists. This line includes video analyzers, video plotters, video processors (enhancers), video quantizers, etc. This instrumentation is available without need for development and is reasonably priced. Also, it can be used at the display system itself or after a distribution has been accomplished. In short, using standard TV format allows the operator to draw upon an existing industry of hardware and expertise in order to maximize his interaction with the data.

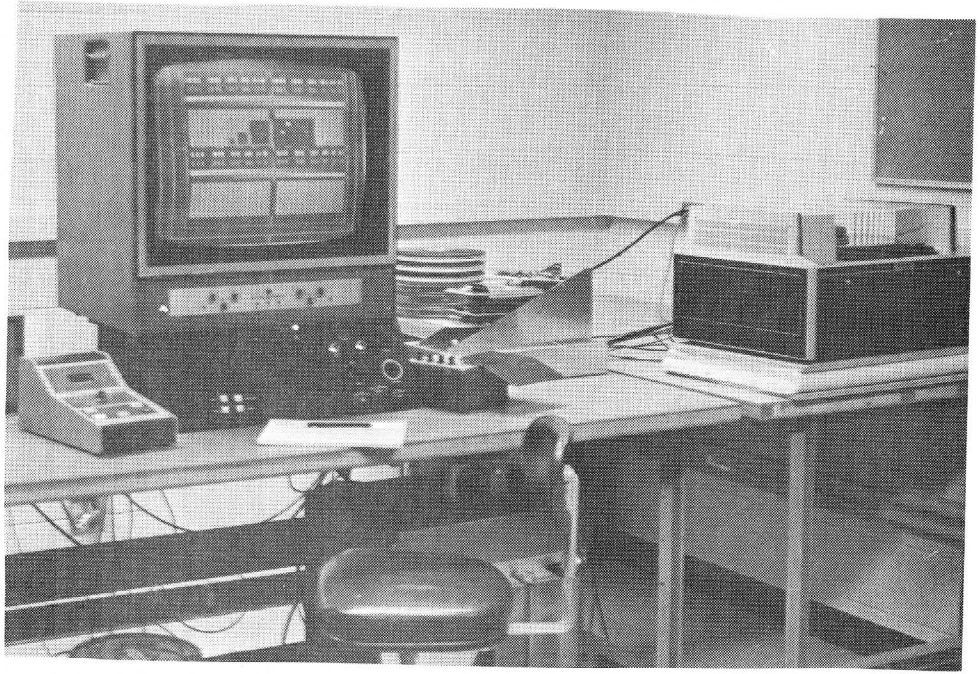

WINDCO Display System

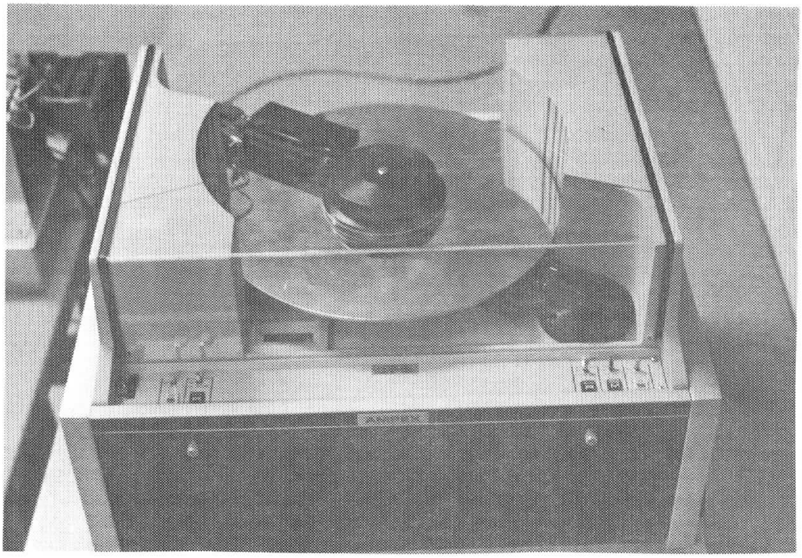

AMPEX DR-10 Video Disk Recorder

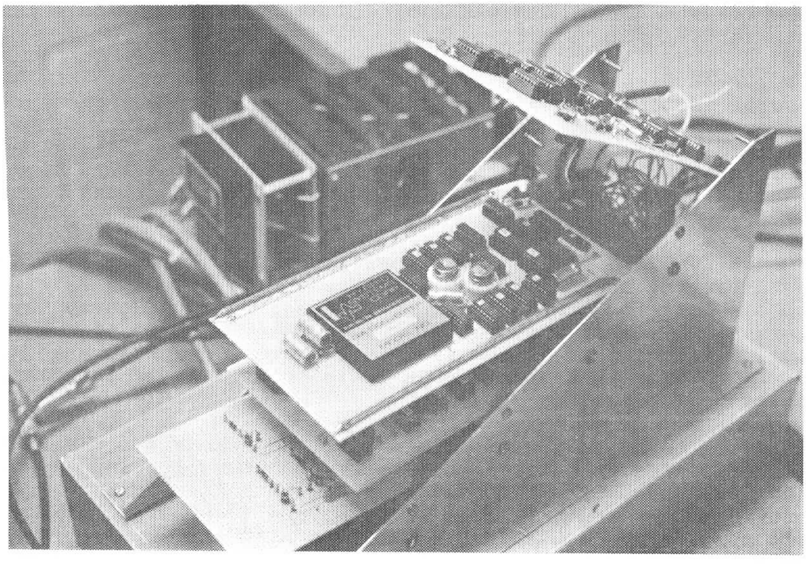

Fast Storage Unit

Theory of Operation

Analog Disk

The heart of the WINDCO display system is an Ampex DR-10 analog disk recorder. The disk recorder is a unique recording device utilizing a magnetic coating on the surface of an aluminum disk instead of magnetic tape. As the disk is rotated, the head traverses a circular track on the disk surface. The main advantage of this method of recording is that once a track has been recorded, it can be played back repeatedly—once for every revolution of the disk. In particular, if the video from a TV frame is recorded on one track and if the disk rotation rate is 30 rps (revolutions per second), the video signal will be played back at the proper rates to refresh a TV monitor.

This is exactly what Ampex has done in their DR-10. Their disk is made of 3/16-inch thick aluminum with a nickel-cobalt magnetic coating, and a rhodium protective coating. By rotating a 14-inch diameter disk at 30 rps, a head-to-disk speed of about 1000 ips (inches per second) is achieved. With this head-to-disk speed, an FM signal modulated with TV video can be recorded on the disk. The 30 rps speed of the disk means one TV frame is recorded for each revolution of the disk. It also means that on playback a single TV frame can be presented to a TV monitor at the 30 frames per second rate it needs for proper refresh. The ferrite heads used have dual gaps, one for record/reproduce and the other for erase. The erase gap precedes the record/reproduce gap over the disk surface, and therefore the track is erased just prior to being recorded. The frequency modulation (FM) recording method is used to avoid the problems of amplitude instability inherent in the magnetic recording process. Ampex achieves a useful bandwidth of 4.2 MHz in their DR-10 which is adequate for TV.

The DR-10 disk recorder also has the ability to move its heads in steps or increments radially along the disk surface. Each step causes the head to traverse a new circular path or track. By this method, more than one TV frame can be recorded on the disk. In fact, the DR-10 utilizes both sides of the disk, with one movable head on each surface. This configuration allows over 600 TV frames to be recorded.

The DR-10 contains all the signal processing circuitry necessary to allow the recording and reproducing of a standard TV signal. It also contains the control circuitry necessary to properly move the heads along the disk surfaces during record and reproduce. In addition, all functions of the DR-10 are remotely controllable, and in the WINDCO display system the DR-10 is controlled by the computer and the control panel.

In order to be fully compatible with the standard format, the DR-10 incorporates an optical tachometer mechanically tied to the disk and its drive. The tachometer, along with associated electronics, provides the proper TV sync signals. Horizontal and vertical drive, composite sync, blanking as well as a TV frame start, and a high tach signal are all provided. The frame start signal indicates the start of a new TV frame as opposed to the vertical drive which indicates TV fields, and the high tach signal has 10 cycles for each TV line or horizontal sync pulse. These last two signals are not standard TV signals but are useful with interfacing to the disk.

The WINDCO display system uses the DR-10 as a storage device (up to 600 TV frames) and as a TV refresh device. A TV frame can be considered a data storage block or matrix, consisting of 525 lines with the resolution of each line limited by the available bandwidth. Television has a theoretical aspect ratio of four to three (horizontal to vertical). Thus, if a TV frame is 525 lines vertically, it should be 525 × 4/3 = 700 lines horizontally and can therefore be considered a 525 × 700 matrix of almost 400,000 elements. We call these elements "pixels" or "TV pixels," because they are the elements of a TV picture. For practical purposes seen later, we consider each TV line to have 768 pixels instead of the theoretical 700.

Also note that each pixel position has associated with it a brightness or gray level. Although a TV monitor can only display about 64 discernible gray levels (or 6 bits) the grayscale potential of the DR-10 is greater than 6 bits because its signal-to-noise ratio is specified at 40 db. The computer provides the DR-10 with 8-bit brightness information so that each TV frame can be considered a matrix of 525 by 768 eight-bit words. Looking at it from a digital point of view, each TV frame represents a storage capacity of 400,000 eight-bit words or 3.2 megabits; and a fully loaded disk of 600 TV frames represents a total storage capacity of 240 million eight-bit words, or approximately 2 billion bits.

In order to make use of this storage capacity and to allow the computer to produce a TV image, it is necessary that the location of each TV pixel be known. The DR-10 provides most of the necessary timing with its tachometer signals; the TV frame rate signal identifies each TV frame, the vertical sync signal identifies each TV field, and the horizontal sync signal identifies each TV line. In order to identify each of the 768 pixels within each line, a gated oscillator was added to the DR-10. The oscillator is free running at a little greater than 768 times the horizontal sync signal, and it is gated by the horizontal sync signal so that each TV line is broken up into 768 parts. Because the frame rate signal and the horizontal sync signal are generated from the optical tachometer which is physically tied to the disk, these signals define actual physical angular sections of each track on the disk surfaces. (See Figure 1.) The pixel clock, however, is a free-running oscillator, tied to the disk only where it is phased to the horizontal sync signal. The pixel clock will define physical angular sections of each track only if the oscillator is stable with time and if the disk rotation rate is also stable with time. The oscillator is crystal controlled, and its stability is well within tolerances. The basic stability of the disk is specified by Ampex, and measured by us to be less than 1/4 pixel. Consequently, a physical angular section exists for each 400,000 pixel in each of the 600 tracks on the disk. Not only do these sections exist, but by monitoring track number, frame rate

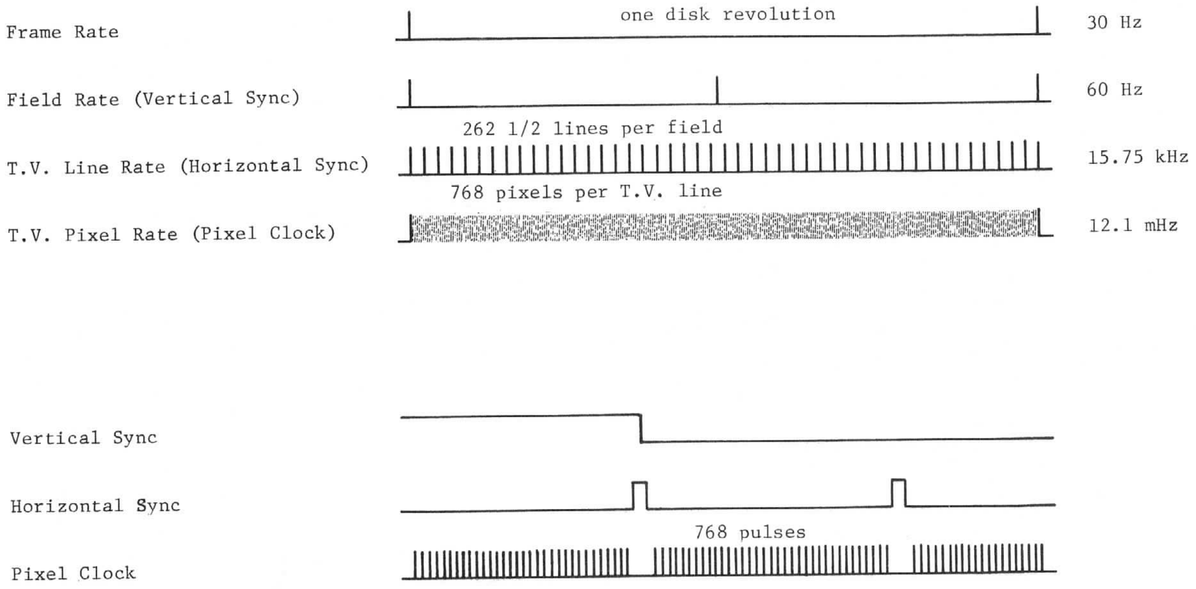

Figure 1 Clock Timing

signal, horizontal sync signal and pixel clock, it is known which pixel each head is reading or writing at every instant in time.

In general, then, the Ampex DR-10 disk recorder provides addressable locations arranged as six hundred 525-line by 768-pixel TV frame matrices. In each of these locations it can store a brightness level corresponding to an eight-bit word, and each of the 525 by 768 matrices of brightness levels can be read out at the proper rate and with the proper bandwidth and timing signals to be displayed on a standard TV monitor in standard TV format.

Coordinate Unit

The Ampex DR-10 disk recorder can store up to six hundred 525 by 768 TV frame matrices, and a physical angular section of a track exists on the surface of the disk for each element or pixel within these frames. By monitoring the track number, frame rate signal, horizontal sync signal and pixel clock, it is possible to determine which pixel a head is reading or writing at every instant in time. Part of the function of the coordinate unit is to continuously provide the TV frame number, TV line number and TV pixel number of the head as it scans the disk surface. These numbers are the "coordinates" of the head and are updated each time the head advances to a new pixel location.

The DR-10 includes a track number indicator which provides both a numerical readout and a BCD output of the track being interrogated. The TV line number is generated by counting the horizontal sync signal which puts out one pulse at the beginning of each TV line. This counter is reset to zero at the beginning of each TV frame by the frame rate signal and, therefore, contains the line number being displayed at every instant in time. Likewise, the TV pixel counter counts the pixel clock and is reset at the beginning of each TV line by the horizontal sync signal. These counters are all synchronous BCD counters implemented with standard TTL logic and contain the instantaneous coordinates of the TV spot as it generates the TV image.

When the operator looks at the TV screen, he sees an entire frame or image. This TV image is generated as the TV spot traverses the standard TV raster at the same time the head traverses a track on the disk, pixel by pixel. Because the coordinates of the head are known at all times, the coordinates of every pixel in the image are also always known. This means the operator could flag any point of interest in a TV image if he had a means to indicate that point.

An electronic TV pointer is used to superimpose a cursor over the video to act as an indicator for the operator. The cursor takes the form of a rectangle on the screen with adjustments that allow the operator to control its height, width and brightness independently. The cursor is produced by adding a series of pulses to the video feeding the monitor. The exact position in which the cursor appears within the TV frame is determined by the operator with the use of a joystick control.

A joystick is a mechanical contrivance which ties two controls to a finger-held stick which can be moved - in a two-dimensional plane - in such a way that the output electrical signals represent the rectilinear coordinates of the position of the stick. The electrical signals generated by the joystick control the time duration of two monostable delays. One delay is triggered by the vertical sync signal to produce the vertical position of the cursor, and the other is triggered by the horizontal sync to produce the horizontal position of the cursor. These two delays then position the cursor within the TV frame dependent upon the position of the joystick. By watching the screen and moving the joystick, the operator can position the cursor to any point of interest in the TV image quickly and easily.

The pulse which produces the cursor by being added to the video signal is also used to instantaneously transfer the contents of the counters which contain the continuously updated coordinates of the TV spot into holding registers. The numbers in these registers then are the coordinates of the point of interest that the cursor is flagging. These numbers relate directly to the pixel locations on the disk and therefore to the original digital data in the computer. These coordinates are displayed to the operator by means of readouts on the control panel and are presented to a paper tape punch where they are stored for future entry into the computer for analysis purposes.

It should be noted that because the cursor is superimposed on the video, the coordinates are accurate regardless of how the TV monitor may distort the signal or regardless of whether the raster scan is linear or not. Also, no parallax errors are introduced into the operator's ability to position the cursor.

In short, the coordinate unit allows the operator to flag any point of interest within any TV image and get accurate coordinates of that point in terms of the original digital data loaded on the disk by the computer.

Fast Storage

The Ampex DR-10 disk recorder provides 240 million addressable locations arranged as six hundred 525-line by 768-pixel TV frame matrices. In each of these locations it can store a brightness level corresponding to an eight-bit word. Each of these TV frames can be read out at the proper rate and with the proper bandwidth and timing signals to be displayed in standard TV format. This means that an entire TV frame must be presented 30 times per second, and since a TV frame contains 525 lines, the line rate is 30 × 525 = 15.75 KHz. Also, since there are 768 pixels per line, the pixel rate is 15.75 KHz × 768 = 12.1 MHz. This is the pixel clock frequency and also the rate at which the eight-bit brightness levels or words are read out of the disk. However, it is also the rate at which the words must be presented to the disk when data are being loaded from the computer. The Raytheon 440 computer used in the

WINDCO display system is not capable of even approaching this data transfer rate. It has a maximum transfer rate of 30 KHz for 16-bit words. Thus, in order to load the disk, a time base translator is necessary.

The fast storage unit provides the necessary time base translation by accepting 768 words (one TV line) from the computer at its 30 KHz rate and presenting them to the DR-10 disk recorder at the necessary 12 MHz rate. It is a short-term integrated circuit memory capable of storing 768 eight-bit words. It is implemented with six quad 256-bit dynamic shift registers. Each chip can store 256 four-bit words and, by arranging the six in a 3 × 2 matrix, the necessary 768 eight-bit word capacity is realized.

At the time the WINDCO display system was being built, the ability to move digital words around at a 10 MHz rate was just being developed. Standard core memory was limited to about 1 MHz and bipolar registers, although fast enough, were small, the largest being about 100 bits per chip. The advent of the MOS technology gave the capacity of 1024 bits per chip but generally could not meet the 10 MHz clock rate specification. However, a few manufacturers were just starting to produce the dynamic shift registers with both the capacity and the speed to make the fast storage possible.

We used the Signetics SN2502B quad 256-bit MOS, two-phase clock dynamic shift registers. They are guaranteed to operate over the range of 500 Hz to 10 MHz clock rate, and typically operate over the range of 10 Hz to 18 MHz. The 10 Hz lower clock frequency limit means that the effective maximum storage time of the fast storage is 100 msec. This is adequate because the maximum time the data have to be stored when loading is one revolution of the disk which takes 33 msec.

The only drawback of the SN2502B was that it had a fairly large clock input capacitance of 150 pf per clock phase per chip. This meant that each of the two clock drivers would have to drive 6 × 150 pf = 900 pf at the 12.1 MHz rate. This requires a total drive capacity for all six chips of more than 0.5 amp. Fortunately, National Semiconductor makes a clock driver, the NH0012C, which is designed to drive MOS shift registers beyond 10 MHz and with peak currents to 1 amp. With one of these drivers for each clock phase, the SN2502B's are being adequately driven. It should be pointed out that with the high currents and high frequencies represented in this fast storage, good decoupling, by-passing and shielding techniques are necessary.

In actual load operation the fast storage unit is under the control of the computer and sequentially loads the 768 eight-bit words according to a clock bit sent from the computer.

At the same time this loading is going on, the computer presents a track number to the load control. This number represents the TV line number (000 to 524) these data are to comprise. Because of the DR-10 timing signals and the coordinate unit, each TV line and each of the 768 pixels within this line has a specified angular section on the track allotted to it, and the single TV line number sent by the computer addresses these sections on the track. When all 768 eight-bit words are loaded into fast storage, the computer sends an execute command to the load control. The load control waits until the appropriate section of the track is being interrogated by the head and then sequentially unloads the fast storage unit at the 12.1 KHz word rate.

The Ampex DR-10 disk recorder is an analog recorder and utilizes an FM system to record an analog signal with a bandwidth of 4.2 MHz. This means that the eight-bit digital words must be converted to an analog signal. We use the model 390-10 digital-to-analog converter (DAC) made by Hybrid Systems Corporation. It is made for high speed conversions and has a settling time of less than 50 msec.

The signal from the DAC is routed to the DR-10 record electronics with a theoretical maximum signal bandwidth of 6 MHz. The first thing the DR-10 does to this signal is to bandlimit it to 4.2 MHz, thereby reducing the horizontal resolution of the data stored on the disk and therefore of the TV image on the monitor. The signal is then processed and clamped and applied to an FM modulator.

A difficulty arose in this signal processing stage due to the fact that computer data do not have the same average levels as standard composite TV signals do. This caused the A.C. coupled amplifiers and the video clamp circuits to distort the computer brightness data badly. The problem was solved by applying the bandlimited signal directly to the FM modulator as a D.C. coupled signal and by eliminating the video clamp circuit. With direct coupled computer data, the video clamp is unnecessary. These modifications resulted in a good signal being recorded on the disk.

On playback, however, some of the same problems showed up in the TV monitor. The problems here were not so serious because monitors are not as critical as FM recording systems, but if a high amplitude fiducial mark was placed on the data, for instance, the A.C. amplifiers within the monitor would cause the average brightness of the data after the fiducial to be higher than the data before. This did show up in the TV image as an undesirable brightness shading. A solution to the problem came with a change in the computer software which redefined a fiducial as a white pulse immediately followed by a black pulse of the same duration. This made the average fiducial brightness zero and therefore the monitor was no longer adversely affected. Note that it was not necessary to modify the monitor.

The fast storage unit, then, provides the time base translation necessary to allow the computer to load the DR-10 disk recorder in standard TV format.

Control Panel

The control panel provides the interface between the WINDCO display system and the operator. (See Figure 2.) From the control panel, the operator can select the track to be displayed or recorded, he can set up a playback loop, and he can control the new frame rate at which the loop is to be displayed. He can add a cursor to the display, control its size, and position it anywhere within the TV image. He can also cause the coordinates of the cursor to be punched on paper tape for future use by the computer.

The most prominent part of the control panel is the TV monitor. It is a 23-inch Setchell-Carlson Monochrome Video Monitor (Model 3M912). The unit is all solid state and of good quality. This monitor has not been modified in any way; however, we do operate it with external sync provided by the DR-10. This eliminates the need for the computer to generate a composite video signal when it loads the disk. More than one monitor could be operating at one time simply by looping them. Also, the contrast and brightness controls on the monitor provide the operator with a useful enhancement capability.

A track number indicator was purchased with the DR-10 disk recorder as an option. It is shown in Figure 3, and uses LED readents to display which track is being interrogated. It indicates from 1 through 600. To move the heads, the operator first places the system in the manual mode with the mode switch (see Figure 4) and then chooses the direction—either to larger numbered or smaller numbered track. He then can advance the heads in this direction either one track at a time by pushing the single step button or at a 30 steps/sec rate by holding down the "fast step" button.

Once a track has been selected, the image appears on the monitor and the operator can work with that image, or he can place the system into the load or automatic playback mode with the mode switch. If he wishes to load a TV frame onto that track, he switches the mode switch to load. In this mode, the system is completely under the control of the computer and will load a TV frame as previously explained. If he wishes, the operator can put the system into the automatic playback mode in which a loop of up to 16 TV frames or images will be displayed in sequence, starting from the selected track and advancing to higher numbered tracks. When the appropriate number of tracks have been displayed, the loop will retrace and repeat. Using the loop size control, the operator can set the number of frames in the loop from 2 to 16, and with the loop rate control he can adjust the new frame rate from 10 per second to one every two seconds. This range includes the rate which the operator will perceive as continuous motion. The monitor refresh rate of 30 frames per second is not changed, but how often it steps tracks is controlled. The operator also has control of how retrace is accomplished. He can select retrace at the same speed as advance or at a 30 frames/sec fast retrace rate.

Figure 2. Control Panel with Monitor

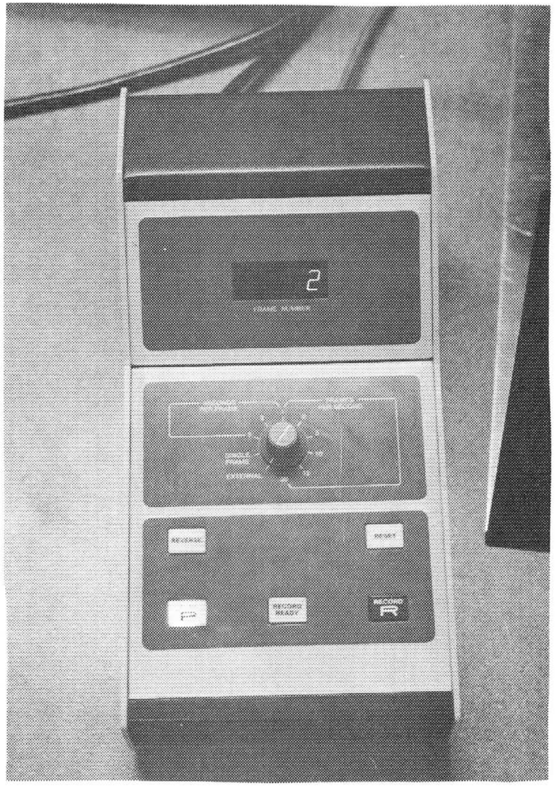

Figure 3. Track Number Indicator

The cursor is generated with a Raytheon electronic TV pointer. This unit superimposes a cursor on the TV image and allows the operator to control its size, brightness and position. As seen in Figure 5, the pointer contains a joystick and three controls. One control is for the vertical height of the rectangular cursor. It is adjustable from one TV line to about 25 lines. Another control is for the horizontal width of the cursor. It is for the cursor brightness. It allows adjustment from zero to brighter than any possible video level. With these controls, the cursor can be adjusted to be compatible with the data and pleasing to the operator. The joystick provides a convenient way for the operator to position the cursor anywhere on the TV screen.

The primary purpose of the cursor is to provide the operator with a means of extracting the coordinates of any point of interest within a TV frame. Once the cursor is properly positioned, the operator pushes the punch button, one of the buttons within the fingertip control cluster (see Figure 4), and the coordinates of its position are punched on paper tape for future access by the computer. The coordinates contain the track number, TV line number and TV pixel number in terms of the original digital data loaded from the computer. It should be added that the coordinates of the cursor are continuously displayed to the operator on the control panel whether or not the information is punched on paper tape (see Figure 4).

Figure 4 also shows that the control panel includes a set of fingertip switches as an aid to rapid selection of features. Two of these switches control the automatic playback mode when the select switch is set properly. The "loop" button causes the loop to be displayed as long as it is depressed and stops it whenever it is in the loop when the button is released. The "advance" button advances the loop one frame each time it is depressed. The "punch/step" button causes the paper tape punch to record the coordinates of the cursor when it is depressed, and advances the loop one frame when it is released. The fourth button is the "punch" button which causes the coordinates to be recorded each time it is depressed.

The paper tape punch is a standard tally punch. We built an interface between the WINDCO display system and the punch in order to convert the parallel BCD data to the standard eight-bit character format of the punch. (See Figure 6.)

Thus, the control panel allows the operator to interact quickly, easily and accurately with the data.

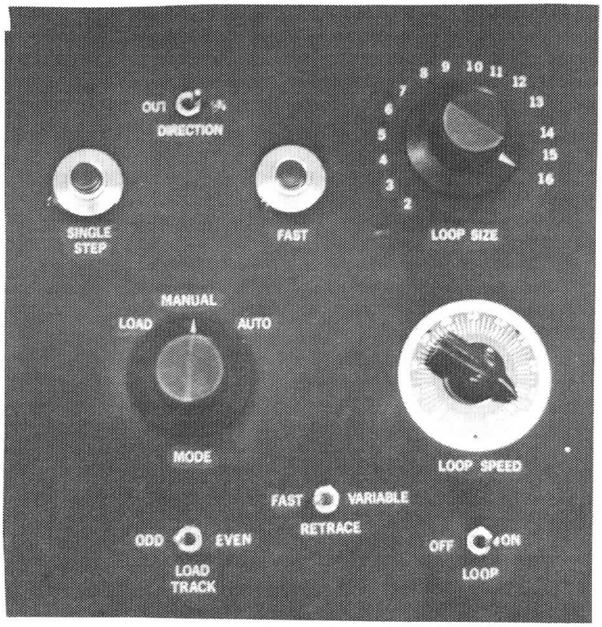

Figure 4a. Control Panel

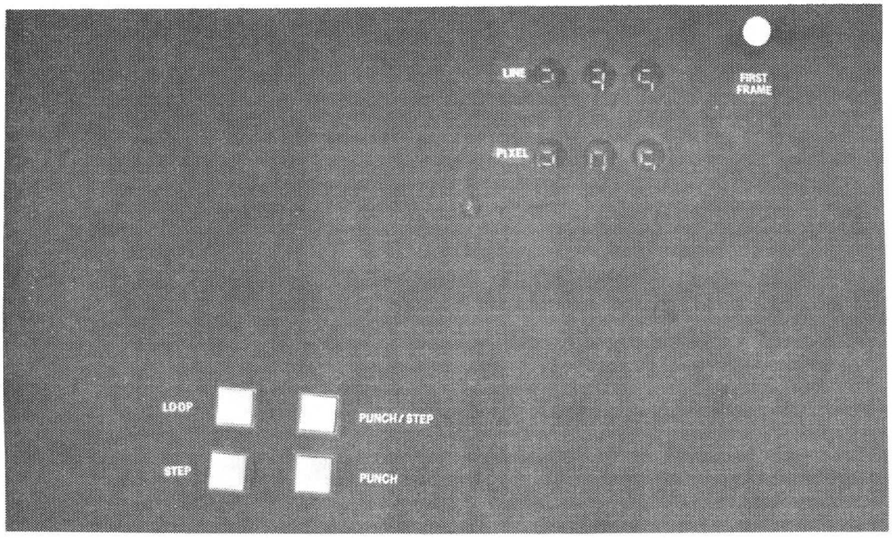

Figure 4b. Control Panel

Figure 5. Electronic TV Pointer

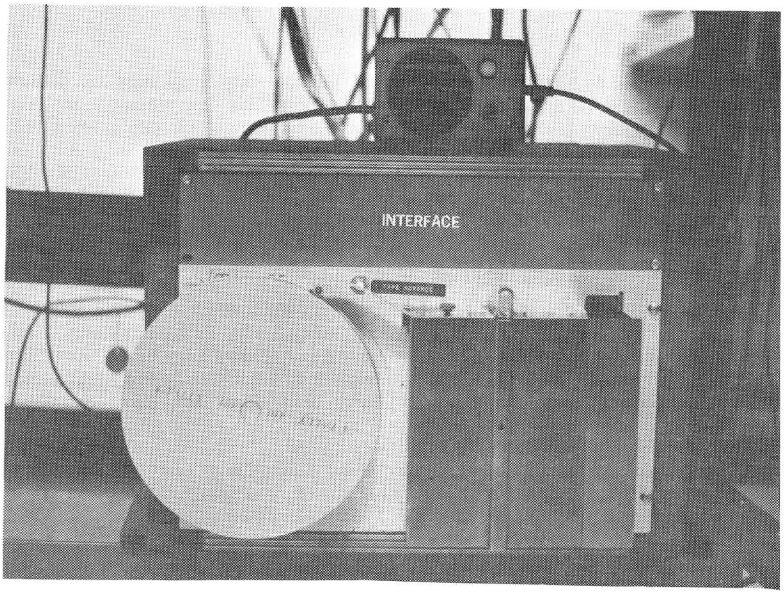

Figure 6. Paper Tape Punch and Interface

A FILTERED VIEW OF FLUCTUATING CLOUD PATTERNS IN THE TROPICAL PACIFIC

John A. Young and D. N. Sikdar

ABSTRACT:

Patterns of fluctuating cloud amount in the tropical Pacific are decomposed into individual frequency bands and presented in longitude-time and latitude-time sections. The natural variability of propagating "clusters" is identified by considering zonal deviation fields, while patterns closer to planetary scale are studied in the zonal means for this limited domain. Periods of both regular and irregular transient activity are made apparent as a function of location. Regimes of "regular" activity are found to differ in direction of cloud propagation, horizontal scale and waveform tilts.

1. Introduction

A considerable amount of attention has been given to studying the synoptic-scale disturbances of the tropics in recent years. This work initially focused on statistical studies of conventional meteorological data where it was found useful to express the results in a time-spectral framework. The obvious advantages of utilizing satellite cloud data to provide a more complete geographical coverage were not long overlooked; initial pictures of propagating cloud patterns were presented by Chang (1970) and Wallace (1970), and quantitative spectral results soon followed (Sikdar, et al. (1972)). These latter results were useful because the patterns were decomposed into both persistent and transient modes of different periods. In addition, statistical estimates of apparent longitudinal scales were derived, although inspection of the longitude-time sections of Chang (1970) and Wallace (1970) gives the impression that a single statistic does not provide an adequate description of the complex cloud patterns.

The purpose of this paper is to present a view of tropical cloud patterns which consists of the full variety of spatial patterns but restricts consideration to individual frequencies. The retention of a spectral type of approach is logical for two reasons: 1) it is an established procedure for characterizing fluctuating systems, especially when typical wavelengths, speeds and frequencies seem to be identifiable, and 2) most theoretical explanations are cast into a simple spectral form. On the other hand, it is recognized that individual disturbances are poorly represented by a single wavelength and period, suggesting that a narrow spectral description is inadequate. It follows that the spectral tool must be less restrictive and this has led us to utilize a procedure based upon 1) time filtering using relatively broad bands, and 2) separation of the spatial patterns into zonal mean and deviation components.

There are several improvements in flexibility offered by this technique. Band-pass filtering allows a quasiperiodic variation of relatively brief duration to be identified, so that intermittent activity and even a limited group of waveforms could be tracked. Slow seasonal changes in, for example, disturbances with periods of a few days may become quite apparent. Since there are no restrictions on the spatial patterns, their degree of organization for each frequency band may be determined at different geographical locations. For those systems which appear organized, regions of prominent activity and wavelength estimates can be made when appropriate.

The remaining sections consist of various longitude-time and latitude-time views of filtered cloud data for the tropical Pacific. From these the reader may gain an improved concept of the degree of organization and behavior of tropical cloud systems for the various time and space scales.

2. Data Analysis

The data set for this study consists of estimates of percentage cloud cover for rectangular sectors measuring 5° latitude by 10° longitude over the Central Pacific Ocean. To facilitate comparison with the work of Chang and the statistical results of Sikdar, et al., the study focuses on the period 1 April - 31 July, 1967 over an area extending from 140°E to 120°W and from 20°S to 20°N. As discussed in Sikdar, et al., the sensitivity of the results to gross changes in the brightness of the daily ESSA-III mosaics is lessened by considering the percent coverage by minimally bright systems.

The time series have been analyzed by computing the time mean and band-pass filtering of the un-normalized data. The band-widths for these 15-point Gaussian filters are chosen to be relatively great, as seen in Figure 1. These choices allow a decomposition of information into different primary periods in a way that allows a power response greater than about one-third for the entire range of periods from 3.5 to 20 days. The modest overlap of the "six-day" band is not considered to be a detriment to the qualitative interpretations of this data study. This does serve as a reminder that the information content of the raw cloud data and its subsequent spectral decomposition act to limit the amount of significant detail. Thus only the most obvious relationships involving amplitude and phase can give reliable conclusions.

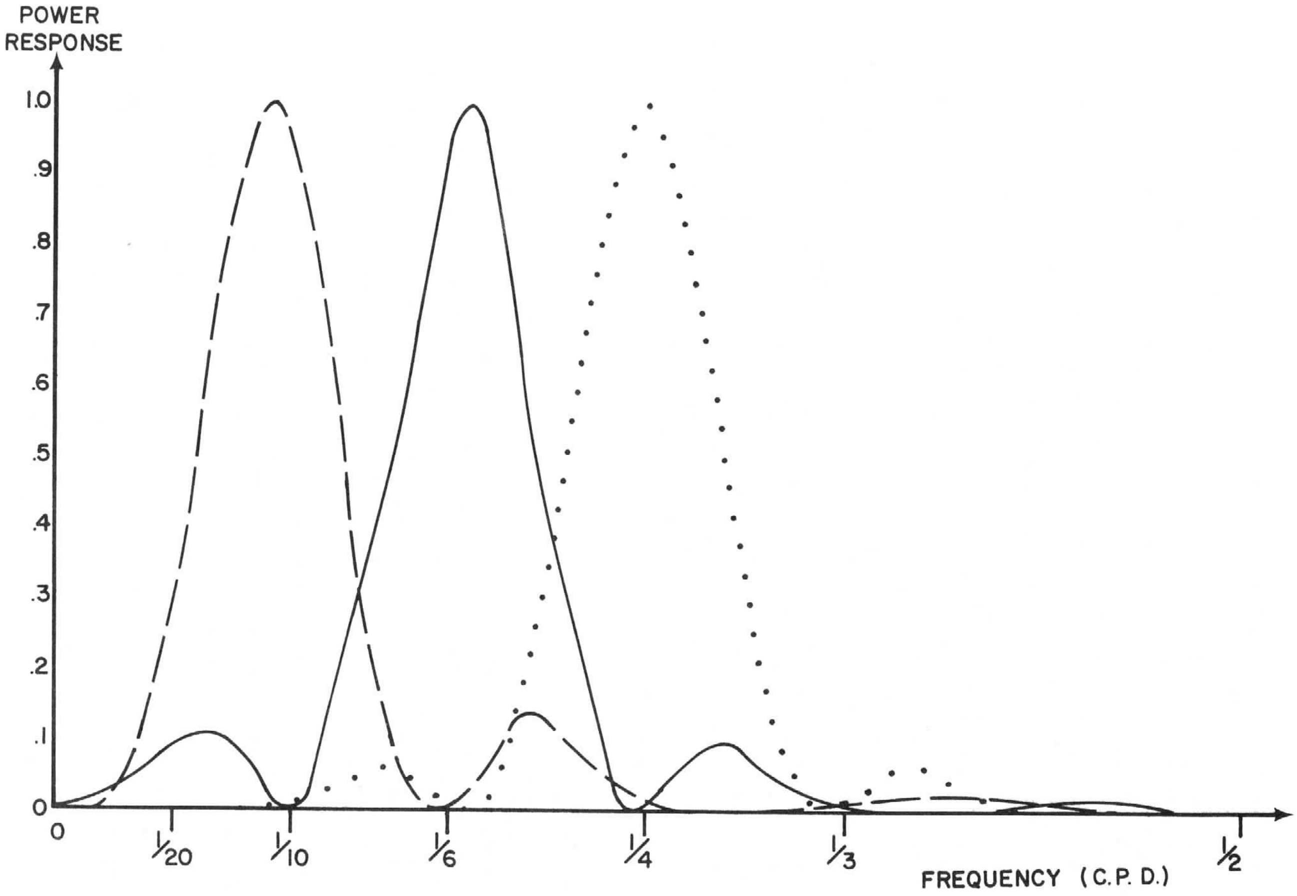

Figure 1. Spectral response functions for the three band-pass filters used in this study. Peak periods are centered near days 4, 6 and 10.

Some advantages of using relatively wind-band filters are demonstrated in the spectral decomposition of time series of total cloud amount in the Northern and Southern Hemisphere portion of the domain (Figure 2). For example, a comparatively short-lived period of "ten-day" activity contained in the original Southern Hemispheric series emerges quite clearly at about 50 days. This intermittent behavior would not be as distinct if a narrow filter were used, in which case only slow seasonal variations of quasiperiodic activity would be obvious. While the original series for the Northern Hemisphere shows a clear seasonal increase, the filtered data for six and ten days exhibit only slow changes. Curiously the four-day oscillations in total cloud amount seem to decrease as the summer period sets in; during the earlier active period the two hemispheres seem to be out of phase.

3. Zonal Means

Inspection of satellite cloud photographs indicates that cloud activity in the tropics appears to be a mixture of longitudinal scales as well as time scales. For example, the older picture of the ITCZ as a zonally elongated region of clouds is occasionally seen on individual days as well as in time mean pictures (Kornfield, et al. (1967)). The newer picture of zonally propagating "cloud clusters" is always seen either as distinct cells or irregularities in the ITCZ band on the scale of the "easterly wave." As an attempt to separate these two modes of activity we have further separated the data into a "zonal mean" averaged over 100° of longitude along a latitudinal circle and a "zonal deviation" from this mean. It is clear that the zonal mean isolates those fluctuations which appear in phase with one another and which are longitudinally extensive. Thus, planetary scales would be reflected in this zonal mean, as opposed to small scale clusters. However, it does not follow that a planetary-scale pattern is excluded from the "zonal deviation" field defined for this limited study area. Figure 3 shows that the contributions of several of the planetary scale cloud patterns (represented as step-functions with amplitude 0 or 1.0) to the zonal mean may be quite large. The actual contribution is variable (shaded area) since it depends upon the phase of the pattern relative to the domain. The upper and lower bounds of the shaded region indicate that the maximum and minimum possible zonal deviations may also be quite variable.

In summary, it is important to remember that time fluctuations in the "zonal mean" or "zonal deviation" fields may result from
a) both amplitude and phase changes in planetary patterns, and
b) primarily from amplitude changes for the cluster scales.

The latitude-time behavior of the zonal means is shown in Figure 4. The transient character of the ITCZ belt in the Northern Hemisphere is evident in the unfiltered ("observed") data and the time mean as well as the persistent location of strongest activity in the filtered picture, especially at four days. Seasonal trends in the four-day activity are not evident, but three periods of maximum activity are noted at about days 25, 50 and 80. Interestingly,

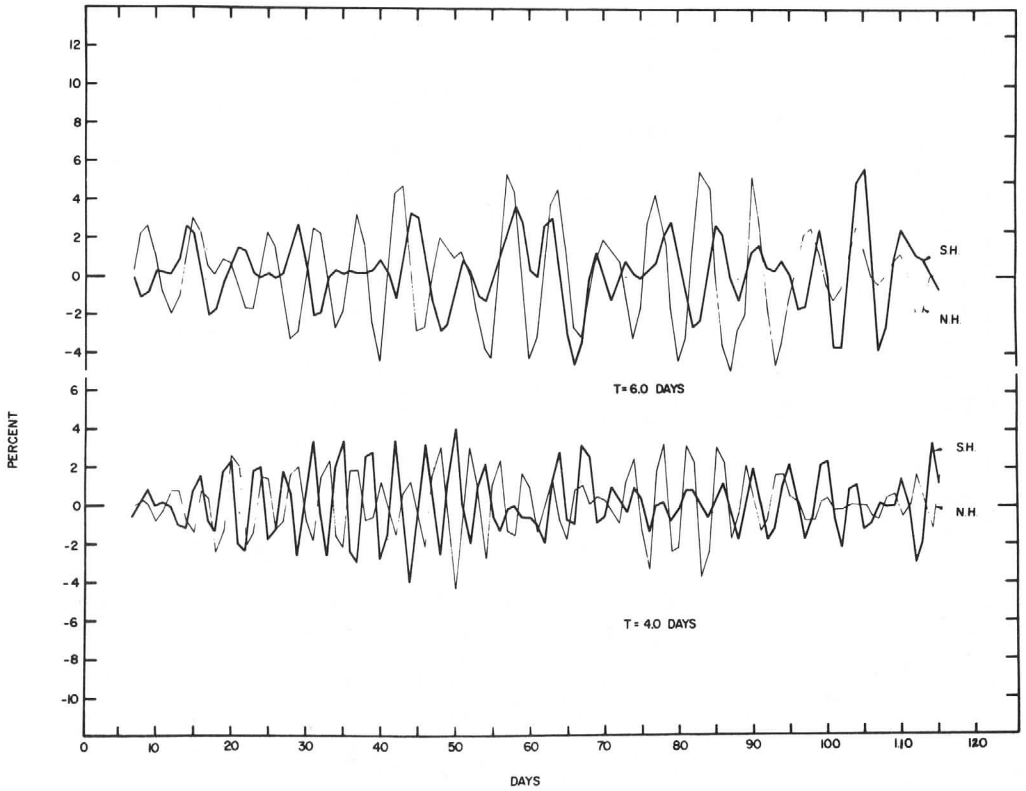

Figure 2. Time series of total cloud amount in the northern (N.H.) and southern (S.H.) halves of the study domain. (a) Unfiltered original data and filtered data for periods centered on ten days. Day 1 is April 1, 1967.

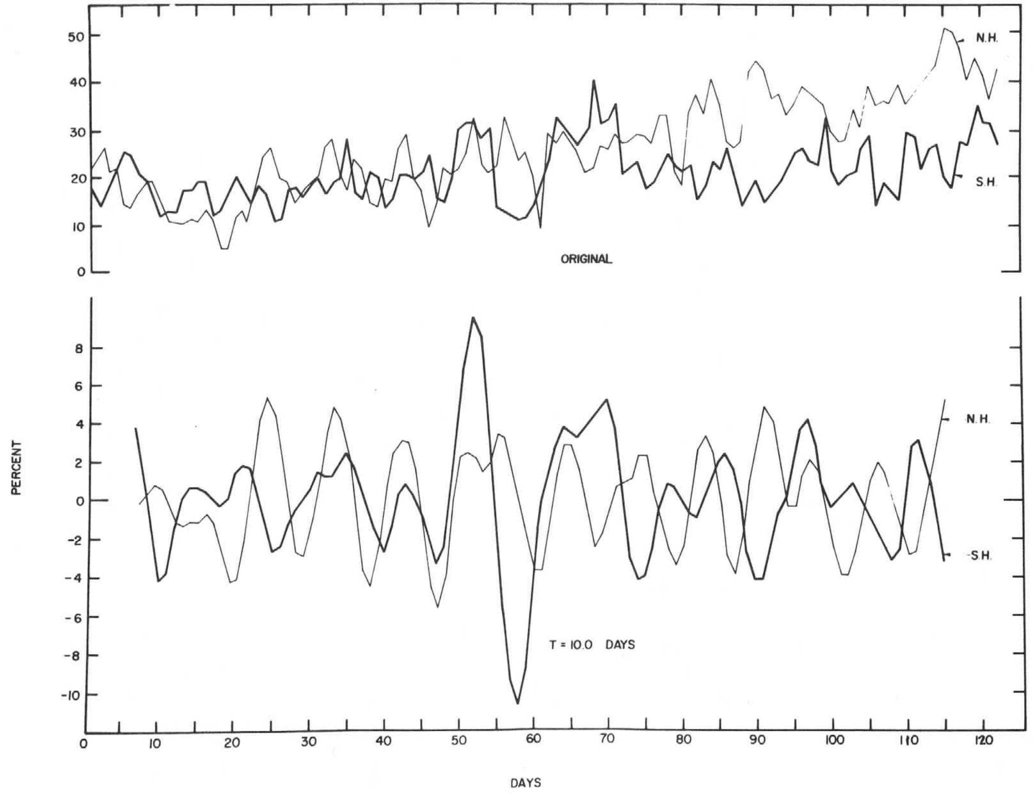

Figure 2. Time series of total cloud amount in the northern (N.H.) and southern (S.H.) halves of the study domain. (b) Filtered data for four- and six-day periods. Day 1 is April 1, 1967.

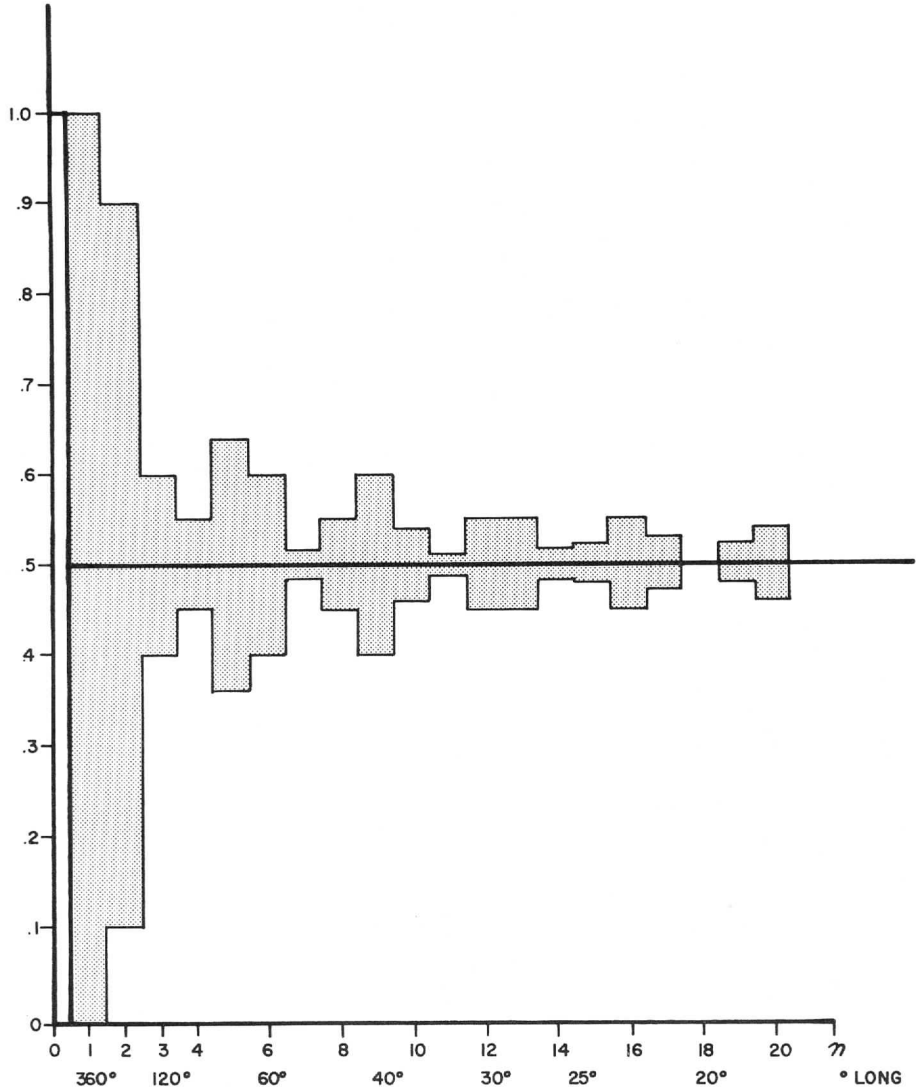

Figure 3. Contributions of various scales of longitudinal cloud variations to the "zonal mean" calculated in this study. The abscissa represents the integral number of periodic step-function patterns contained in the circumference of the earth (i.e., earth "wave-numbers"). The heavy line represents the exact contributions for a hypothetical study domain extending completely around the earth. The shaded area indicates the actual range of contributions for each n when all possible phases are considered.

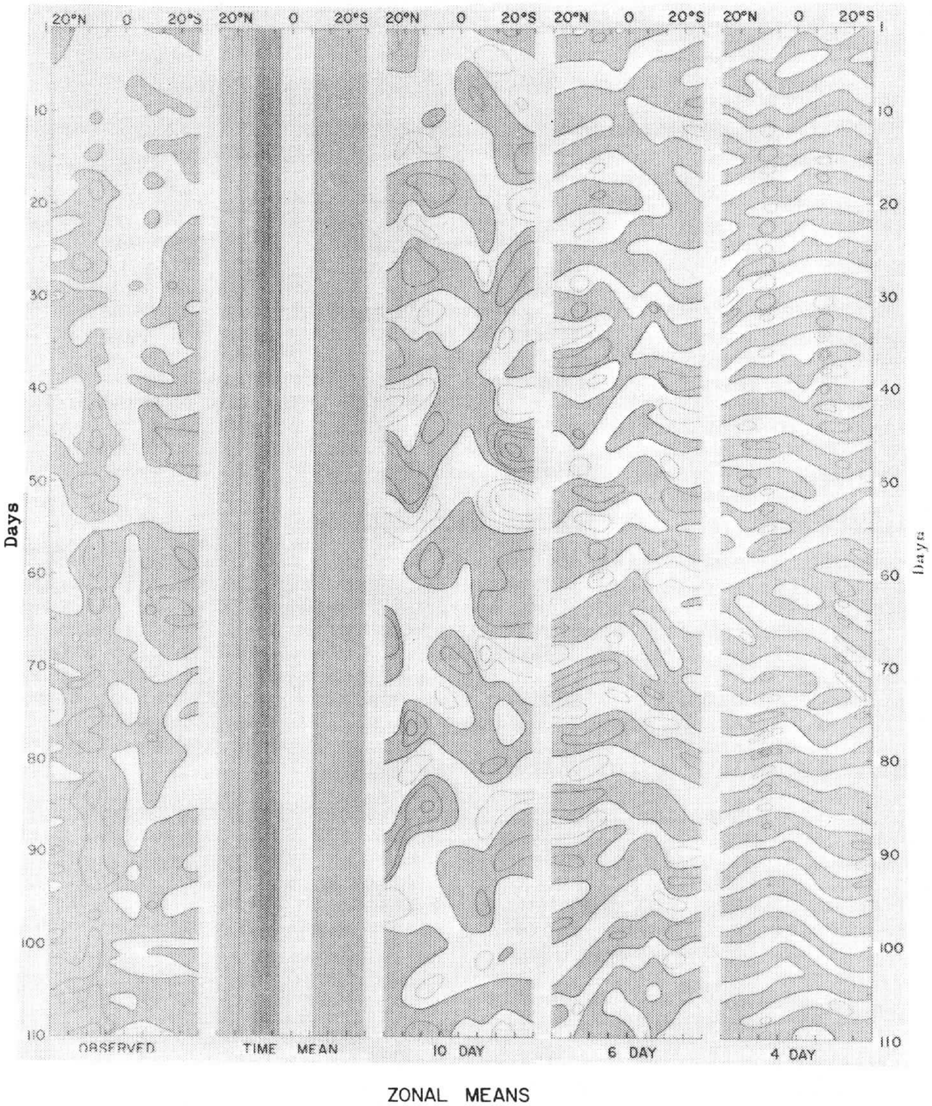

Figure 4. Latitude-time diagrams for zonal means of original and filtered amount data. Medium shading denotes values in excess of 10% for original unfiltered and time mean data and positive deviations for filtered data. Heavy shading for time means denotes values in excess of 15%. Solid isoline intervals are 10% for the unfiltered observed data, 2.5% for the time means and 5% for the filtered data. Day 1 is April 7, 1967.

a single active period near the equator in the Southern Hemisphere occurs at day 37. Longer periods are not particularly important near the mean ITCZ.

The patterns of light and shaded areas must be interpreted cautiously. Since each diagram consists of eight separate time series, it follows that the latitudinal slopes of the shaded regions would be very chaotic if there were no true spatial coupling (i.e., if the data were pure noise). On the other hand, smooth patterns of shading would imply a distinct spatial coupling. Examination of the six- and ten-day patterns suggests that a combination of noise and latitudinally organized fluctuations (especially in the Northern Hemisphere) is present. The four-day patterns appear more organized to the eye, but this is partly a result of the time scale compression. Nevertheless, the four-day and six-day patterns suggest a tendency for propagation of systems away from the equator in both hemispheres. Dominant "wavelengths" are in the range 25° - 30°. Thus, the results indicate a degree of organization linking the zonally averaged activity near the ITCZ with that of higher latitudes. Also seen in Figure 4 is a significant propagation from one hemisphere to another, e.g., propagation northward from about 10°S for the first 30 days and southward from about 10°N for the last 30 days.

4. Longitude-Time Diagrams for Zonal Deviations

The ten time series for each 5° latitude band have been used to calculate a time mean and three filtered time series. These have been plotted in longitude-time sections in each of Figures 5-12. The raw data labeled "observed" consists approximately of a superposition of the four-, six- and ten-day sections oscillating about the "time mean" pattern. Each figure allows study of: a) variable regimes on a seasonal or shorter time scale; b) individual or statistical variations with longitude; and c) individual or comparative behavior classified by frequency. Separate figures may be compared to determine latitudinal differences.

Many of the time filtered patterns show banded structures whose slope and spacing imply a sense and speed of propagation for a simple traveling wave. Any pure "standing wave" component, such as that suggested by Wallace (1971), would appear as a rectangular "checkered" array. A combination of these two would have the appearance of an irregular traveling system with occasional periods of reversal in direction.

To consider an example, Figure 5 shows that these characteristics may be quite variable for a given frequency band. Like most other latitudes, westward propagation is often present. However, a prominent period of eastward motion with four-day periods occurs around day 35; it lasts about two weeks and yet extends only over the eastern region. In this sense the dateline area seems to be a source of activity; in reality it may be related to an upper level or higher latitude regime. Interestingly, the longer periods do not exhibit similar clear-cut activity, except in the sense that all frequencies show more westward propagation during the summer months.

Many of the gross characterizations of the patterns have been stated in Sikdar, et al. Table 1 summarizes the main conclusions regarding apparent longitudinal wavelengths. The westward propagating systems are typically of "easterly wave" scales, with a longer (75°) wavelength also in evidence for the four-day periods. Eastward propagation systems tend to be on a somewhat larger scale. Planetary wavelengths do not appear in this tally since they are partly filtered out of the zonal deviation field. A tally of propagation speeds for all frequencies and longitudes showed median speeds of about 12.5 m/sec. Longitudinal differences in wavelength estimates are not particularly noticeable, although the four- and six-day periods show some tendency to possess longer wavelengths in the eastern portion of the domain.

These statistical results are kept usefully in mind when examining Figures 5-12. Most details are left to the reader's imagination, but it is additionally helpful to note that:

a) westward propagation at all frequencies is most consistent at 10° - 15° N;

b) activity in the ITCZ (5° - 10° N) is particularly well organized as high-frequency westward propagation in the last month, but the lower frequency (ten day) propagation is in the opposite sense;

c) contrasts between high- and low-frequency motions are most distinct in the dry zone (0° - 5°S).

5. Latitudinal Structure of Zonal Deviations

Instead of arranging the time strip data for different longitudes next to one another (as in Section 4), one may choose to place time strips for different latitudes together. In this way the latitude-time structure of the zonal deviations which are dominantly wave-like components) can be examined for separate longitudes. The results of Section 4 suggest the usefulness of this approach in view of the different propagation regimes noted at different latitudes and their longitudinal variations. Figure 13 shows such diagrams for longitudes representing the western, central, and eastern portions of the study domain.

The various portions of Figure 13 give the impression of a latitudinally organized component to the fluctuations. The slopes of the shaded patterns indicate that apparent northward propagation is evident for many frequencies and longitudes in both hemispheres; such propagation corresponds to a southwest to northeast tilt of the axis of a waveform traveling toward the west. For the case of eastward wave propagation, the wave tilt implied by "northward propagation" is of course reversed.

This tendency for propagation across the equator contrasts to the behavior of the zonal means, suggesting that Figure 13 reflects activity of a medium-scale wave mode. The apparent latitudinal

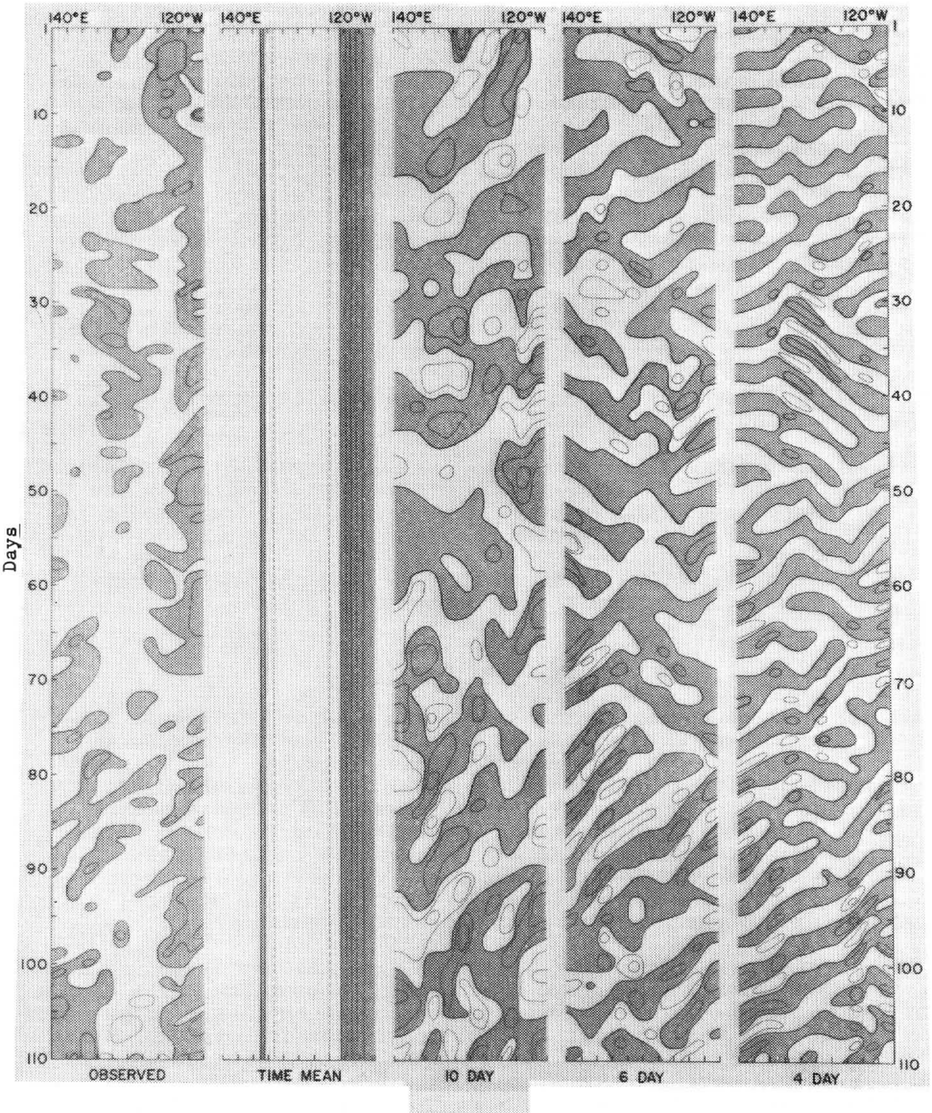

Figure 5. Longitude-time diagrams for zonal deviations of cloud amount data for the latitude band 15°N - 20°N. Shaded areas denote positive deviations. Solid isoline intervals are 20% for unfiltered observed data, 5% for the time mean and 10% for the filtered data. Dashed isolines for the time mean denote intermediate values. Day 1 is April 7, 1967.

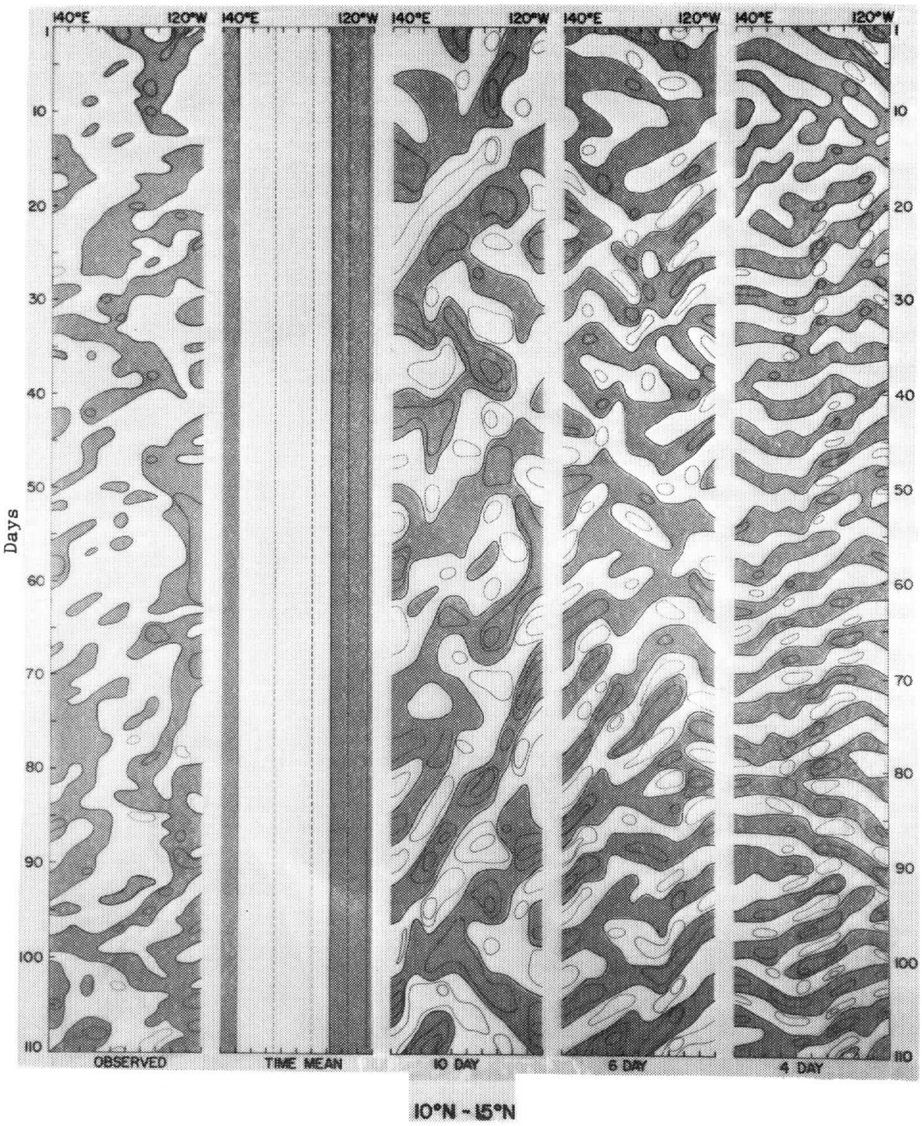

Figure 6. Same as Figure 5, except for latitude band 10°-15°N.

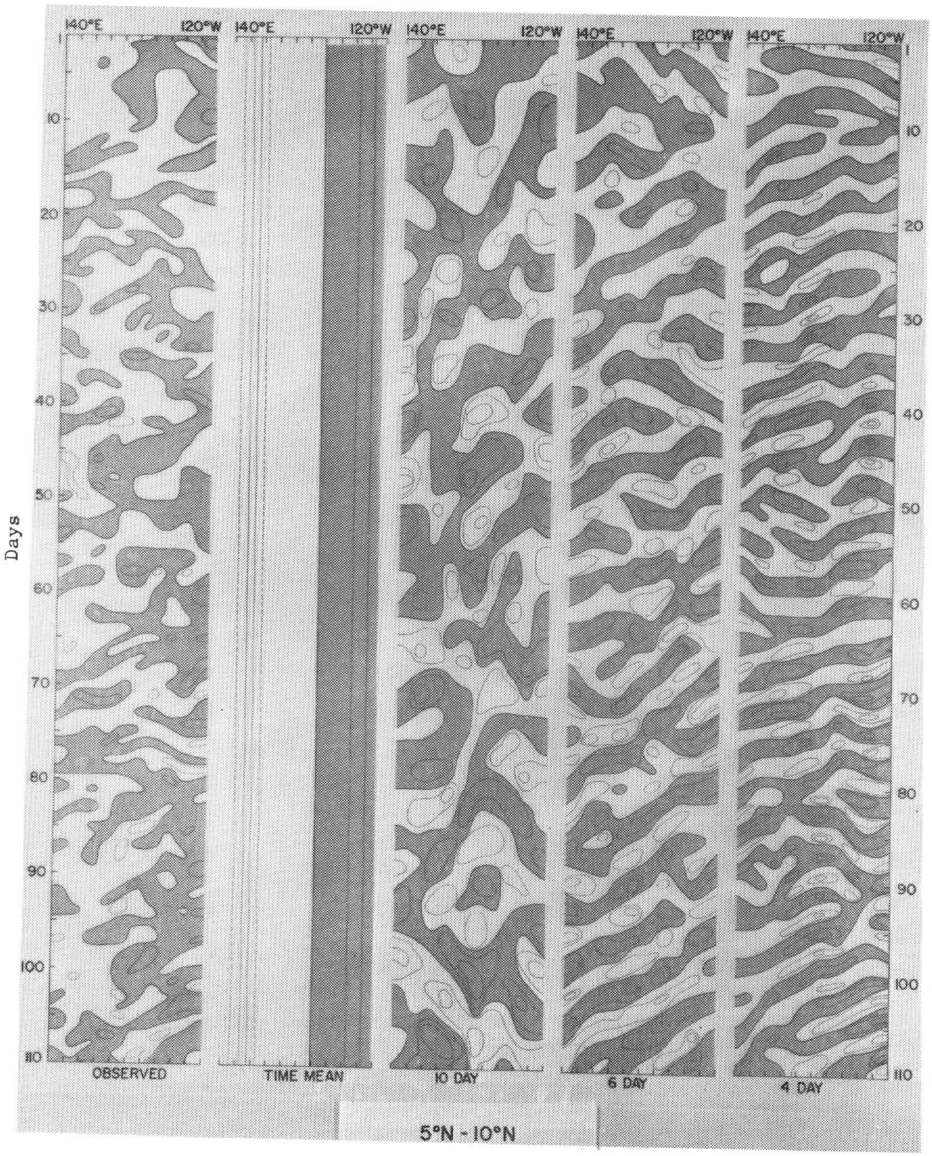

Figure 7. Same as Figure 5, except for latitude band 5°-10°N.

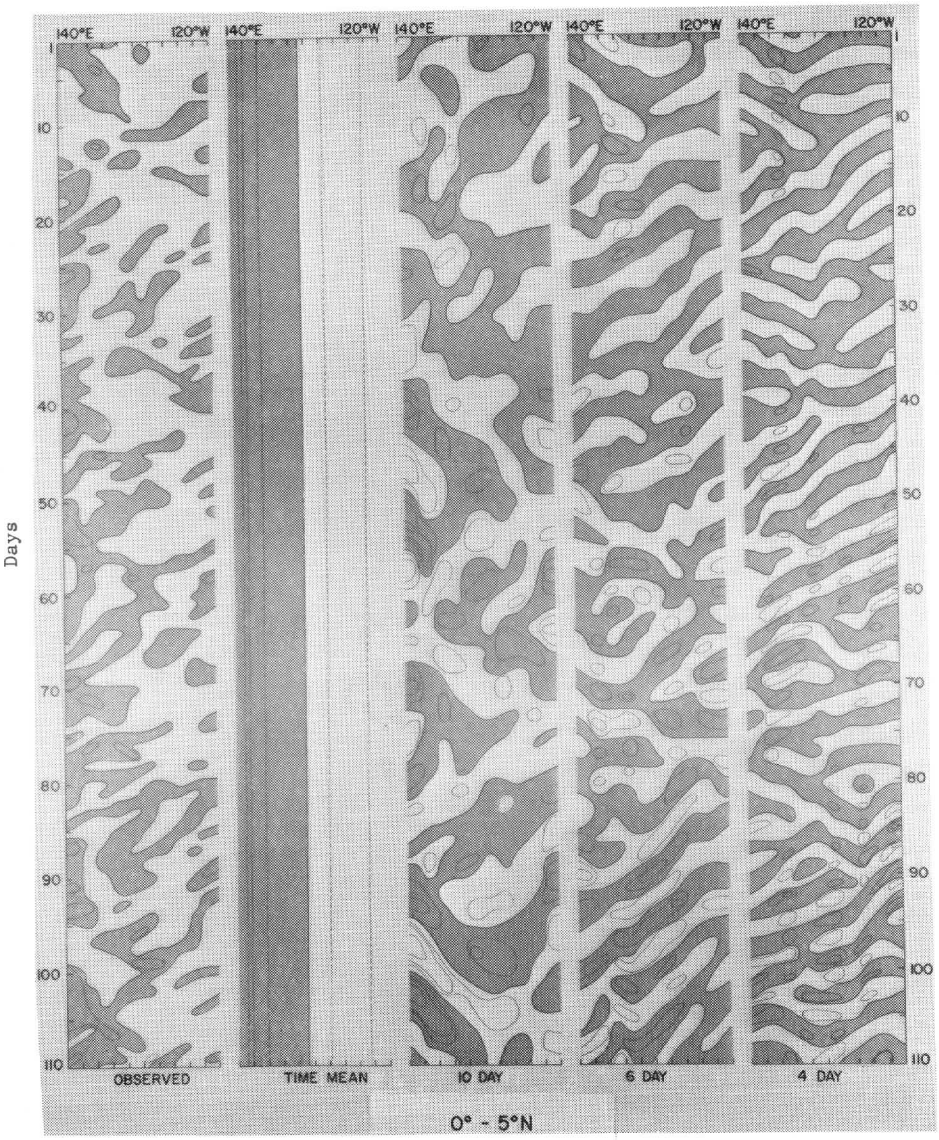

Figure 8. Same as Figure 5, except for latitude band 0°-5°N.

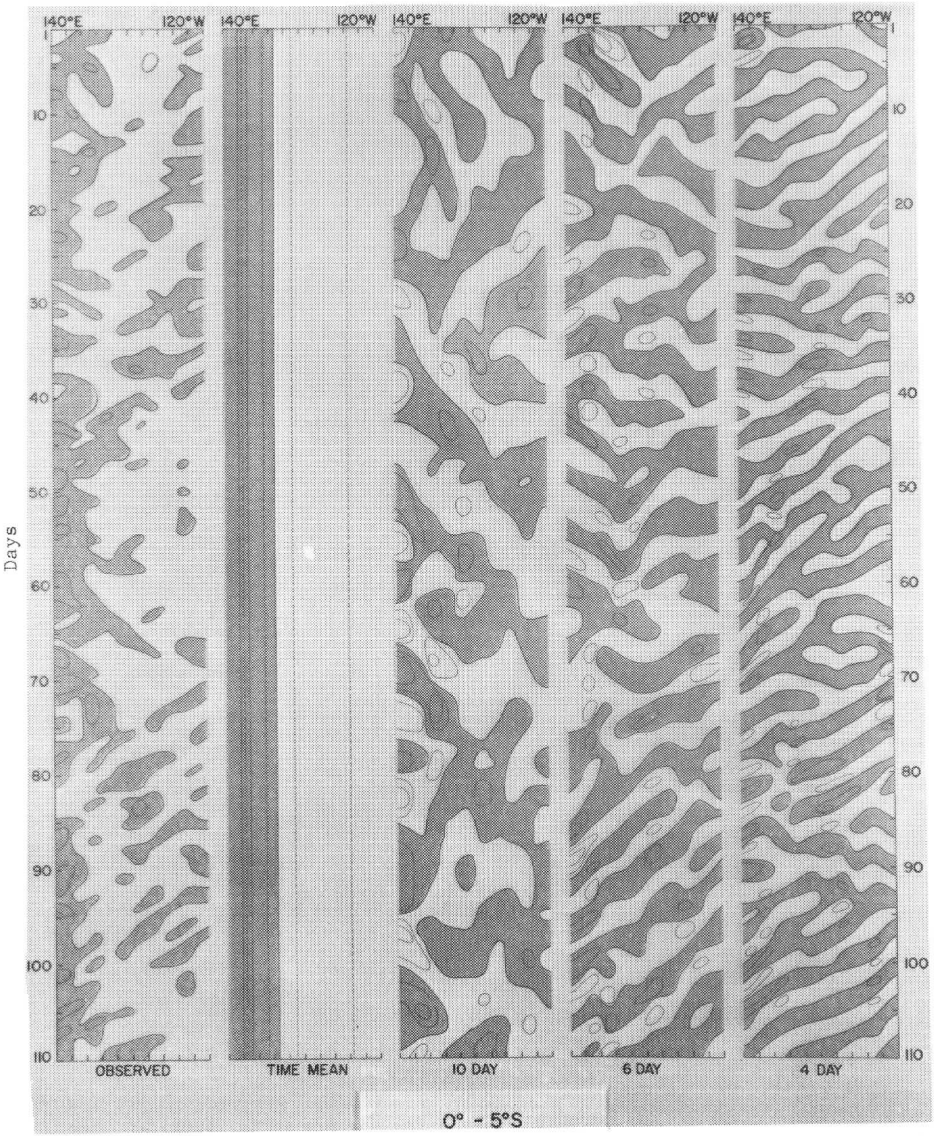

Figure 9. Same as Figure 5, except for latitude band 0°-5°S.

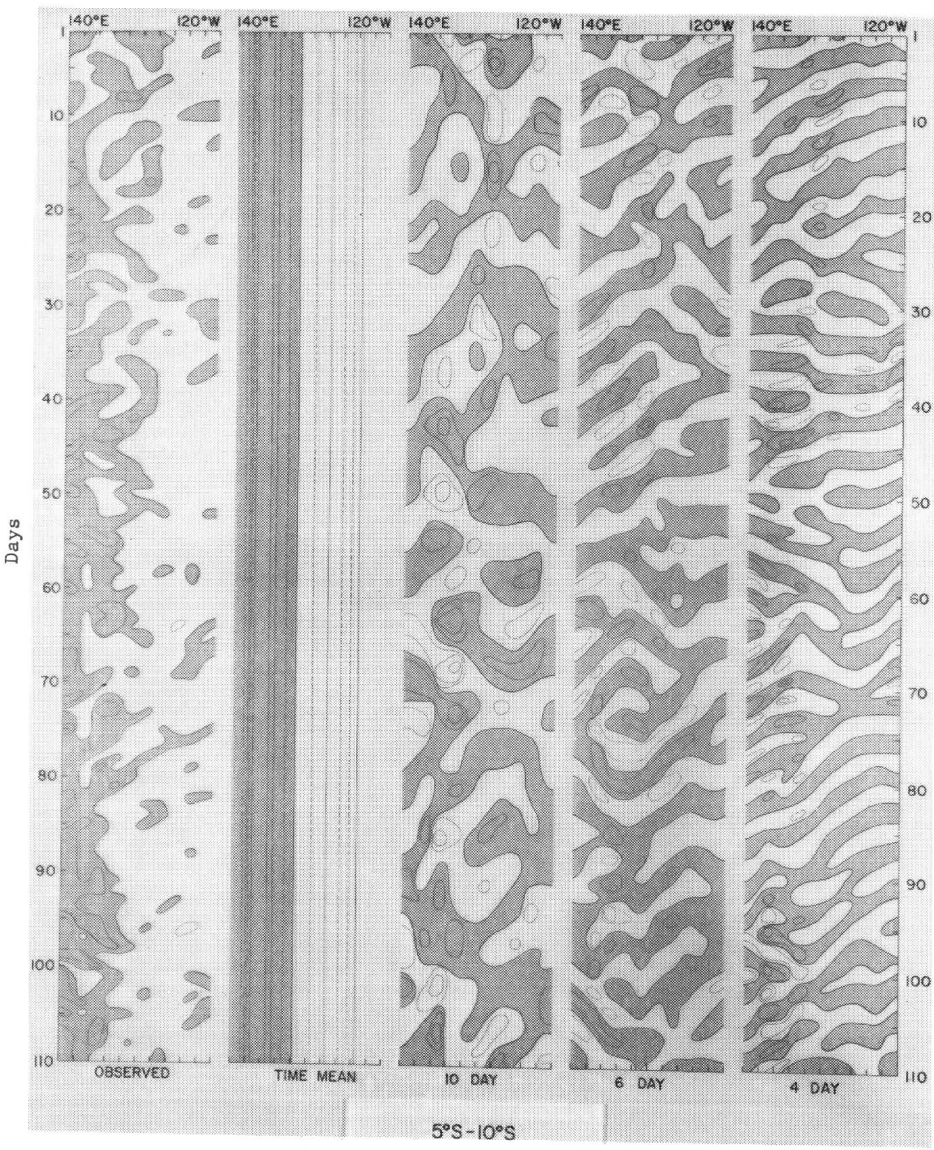

Figure 10. Same as Figure 5, except for latitude band 5°-10°S.

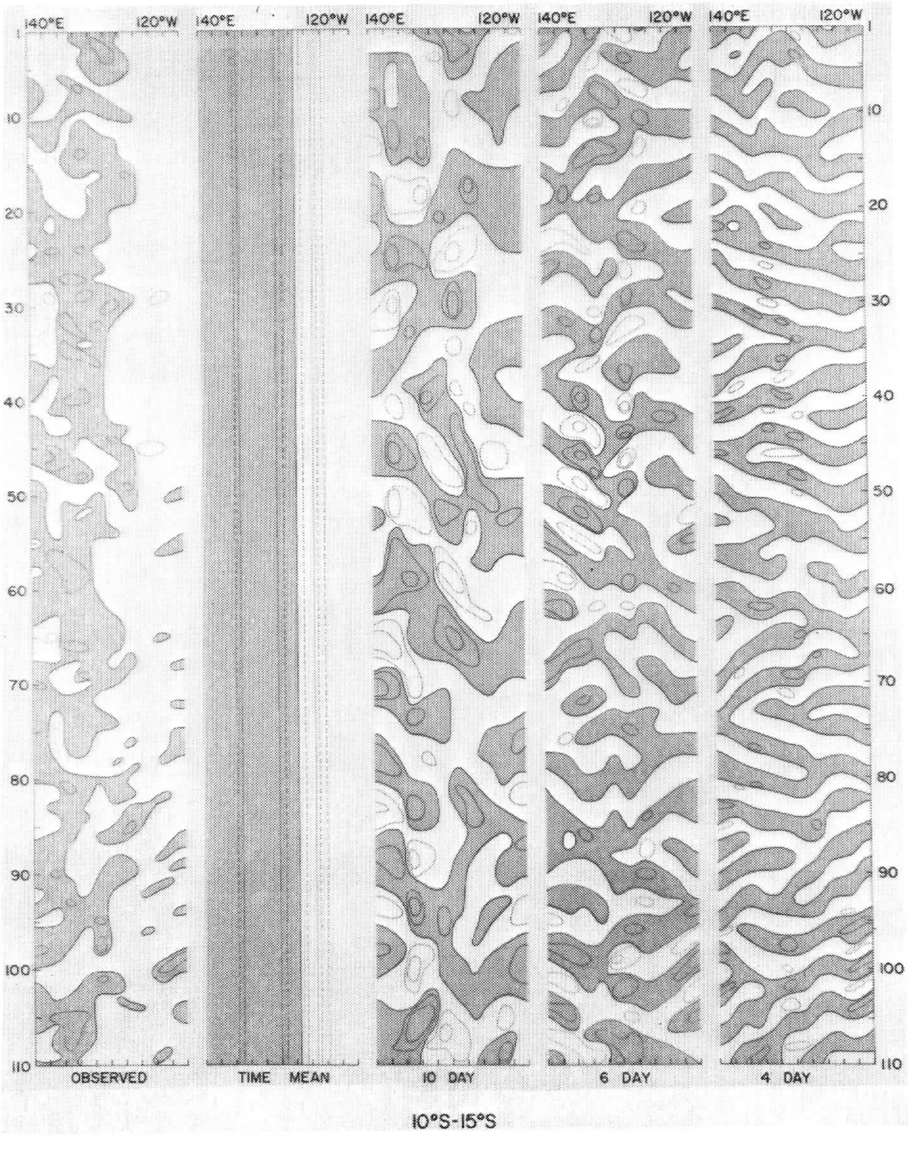

Figure 11. Same as Figure 5, but for latitude band 10°-15°S.

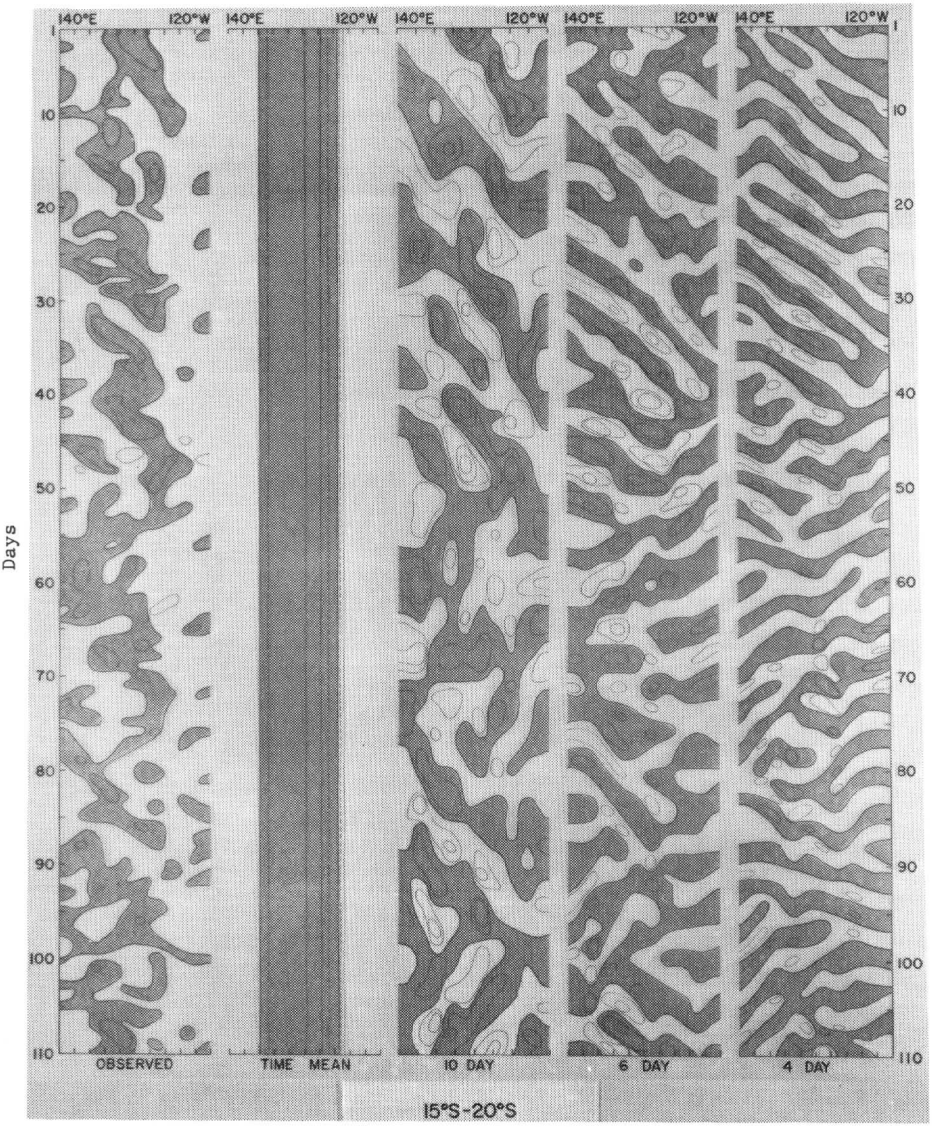

Figure 12. Same as Figure 5, except for latitude band 15°-20°S.

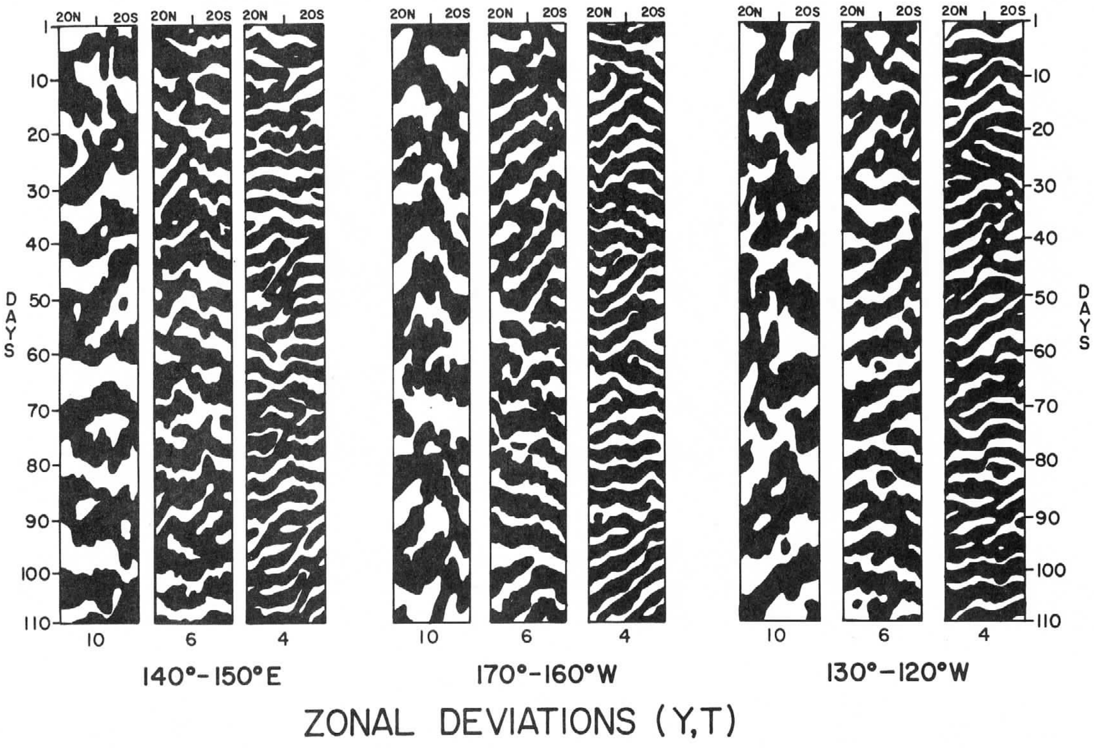

Figure 13. Latitude-time diagrams for zonal deviation filtered cloud data for each of three longitudinal sectors. Dark shaded areas denote positive deviations. Day 1 is April 7, 1967.

wavelengths appear to range from as little as 20° for the four-day periods to more than 40° for the ten-day periods.

The northward propagation is most consistently found in the eastern region (120° - 130°W), but even then periods (at 50 and 100 days) of oppositely directed slopes are found among the different frequencies. The western band also possesses a significant northward slope with time; however; it is interrupted in all frequency bands by occasional periods of zero slope or even apparent southward propagation. The six-day oscillations during days 25-55 show some propagation away from the equator in both hemispheres; this is also evident for the ten-day periods in the central longitude band. Inspection of the figures shown in Section 4 indicates that this is due to the change in direction of propagation so that the wave tilt is still primarily from southwest to northeast. The six-day fluctuations for this central longitude show a period of northward propagation in both hemispheres at day 40, followed by southward propagation at day 90. The somewhat checkered pattern for ten-day activity during days 60-100 in the western longitudes give some indication of a standing latitudinal structure.

These results obtained from cloud amount data contrast somewhat with the conclusions of Krishnamurti (1971) for the wind field during the same time period. Krishnamurti found that the mean planetary wave tilts were from southwest to northeast in the Northern Hemisphere, but the tilts were negligible in the Southern Hemisphere. Shorter transient waves possessed the southwest-northeast tilt in the Northern Hemisphere but were tilted oppositely in the Southern Hemisphere. The reasons for this disagreement are uncertain, but the facts seem consistent with Krishnamurti's observation that the "weather systems" did not exhibit the time continuity evident in the wind field.

6. Conclusion

The figures shown in previous sections have served the purpose of decomposing the complicated space-time cloud patterns of the tropical Pacific into forms which allow the identification of both irregular and wave-like regimes. This has allowed a clearer picture of the natural variability of propagating systems to emerge, particularly on the "easterly wave" scale. The latitude-time structures have given evidence that the waveforms often possess a tilted horizontal axis, suggesting that a picture of the full two-dimensional patterns would yield interesting new results which could be compared with similar wind field data.

ACKNOWLEDGMENTS

The authors wish to thank Peter Guetter for programming assistance and Dennis Heinricy and Richard Cram for assistance in data analysis and interpretation. This research was sponsored by NOAA Grant E-230-68-(G).

References

Chang, C. P., 1970: Westward propagating cloud patterns in the tropical Pacific as seen from time-composite satellite photographs. J. Atmos. Sci., 27, 133-138.

Kornfield, J., A. F. Hasler, K. J. Hanson and V. E. Suomi, 1967: Photographic cloud climatology from ESSA III and V computer-produced mosaics. Bull. Amer. Meteor. Soc., 48, 878-883.

Krishnamurti, T. N., 1971: Observational study of the tropical upper tropospheric motion field during the Northern Hemisphere summer, J. Applied. Meteor., 10, No. 6, pp. 1066-1096.

Sikdar, D. N., J. A. Young and V. E. Suomi, 1972: Time-spectral characteristics of large-scale cloud systems in the tropical Pacific, J. Atmos. Sci., 29, 229-239.

Wallace, J. M., 1970: Time-longitude sections of tropical cloudiness (Dec. 1966-Nov. 1967), ESSA Technical Report NESC 56, Washington, D.C.

Wallace, J. M., 1971: Spectral studies of tropospheric wave disturbances in the tropical western Pacific, Rev. Geophys. Space Phys., 9, 3, 557-612.

THE LIFETIME OF SUBTROPICAL CONVECTIVE CLOUDS ABOVE THE OCEAN

Glenn B. Dick

ABSTRACT:

Data was collected in the BOMEX experimental region ranging from $12^{o}N$ to $18^{o}N$ and $53^{o}W$ to $60^{o}W$. Using ATS-III satellite photographs, 139 convective cloud lifetimes were determined. Each cloud was classified according to size and brightness; radiative cooling values were obtained from the 1969 BOMEX experiment. Cloud lifetimes were then correlated with size, brightness and cooling rate. Other relationships were examined along with the semidiurnal cycle of cloud amount. The study indicates that there is a significant correlation of cloud lifetime with size and brightness but a poor correlation between cloud lifetime and radiative cooling rate.

Introduction

An explanation of the phenomena of certain isolated clouds persisting for hours and others dissipating shortly after formation involves many factors and no single factor always predominates. In this study I have attempted to determine if a relationship exists between isolated convective cumulus clouds and their size, brightness (thickness) and radiative cooling rate at the cloud top.

For the purpose of uniformity, I have selected clouds solely from the BOMEX[1] experimental region (June-July, 1969) over the Caribbean Sea. Having chosen only isolated cumulus convective clouds, the dependence of lifetime on a mesoscale disturbance has been minimized.

A list of factors which affect the lifetime of clouds in a region of this type was compiled. The list is by no means complete, but it is assumed to include the most important factors controlling an isolated cumulus cloud's lifetime.

The dominant requirement for a long lifespan seems to be the continuance of the conditions which generate and maintain the cloud. As long as the system which controls the vertical motion, wave-like motion or cellular convection persists (moisture source and condensation nuclei supply remaining constant), the clouds will not dissipate.

The dominant system in the BOMEX subtropical region appears to

---

[1] BOMEX stands for "Barbados Oceanographic and Meteorological Experiment."

be a type of semidiurnal convective cycle which will be discussed later. The cloud factors involved are:

1. Size of a cloud
2. Thickness of a cloud
3. Thickness of the convective layer
4. Radiative cooling rate at the cloud top
5. Emissivity
6. Temperature (and lapse rate)
7. Moisture source (and gradient)
8. Hygroscopic nuclei source
9. Dissipation mechanisms

The size of a cloud seems to affect its lifetime, with larger clouds indicating a more widespread system of vertical motion. Larger clouds will not dissipate entirely in a relatively small shaft of negative vertical motion as might smaller clouds. In a similar manner, thicker clouds last longer due to more intense convection and thus a stronger forcing system.

The radiative cooling rate at the cloud top should theoretically affect a cloud's lifetime by decreasing the stability. Johnson (1960) demonstrated that radiative cooling, while subtracting heat from a system, actually generates available potential energy. Two earlier theories (unverified) attempted to explain how cooling rates influence stability and cloudiness.

Petterssen (1940) argued that the nocturnal cooling of the lower troposphere will exceed that of the ocean surface and the air immediately above it. This would lead to a decrease of stability and a vertical overturning of the relatively unstable maritime airmass. Presumably, the sky cannot be overcast during the evening if this cooling is to take place. A cloud deck, especially one of middle clouds, would curtail the nocturnal radiation of the free atmosphere below these clouds.

Meinardus (1941) hypothesized that black body radiation from the tops of clouds present during the evening will produce cooling and overturning aloft; with time, this will lead to an increase of the low cloudiness. It is assumed that the radiation of the free atmosphere itself is too small and/or too uniform to affect the stability materially.

Both theories must take higher clouds into account. In the second theory, low cloudiness should increase rapidly if total cloudiness greatly exceeds low cloudiness during the evening. Turbulence initiated in upper cloud decks due to cooling from the tops of clouds usually extends into lower levels, and this should increase the low cloud amount.

Petterssen suggested the opposite conclusion, since high clouds cannot be present for low clouds to grow by cloud top cooling.

Emissivity may affect a cloud's lifetime in a manner similar to cooling rate. Cox (1967) found that, generally, the lower and thicker a cloud, the higher its emissivity.

Temperature may also be a factor, at least for high clouds. Darkow (1964) found that low temperatures in the upper troposphere are conducive to long cirrus cloud lifetime. Cirrus clouds can absorb large amounts of radiant energy and transfer that energy to the surrounding air by conduction with negligible evaporative loss. Thus cirrus clouds may persist for days and continue to absorb infrared radiation. Evaporation can occur only if the ice crystals fall to lower levels.

The effect of temperature on low cloud lifetime has not yet been determined, except for relationships with lapse rate and stability.

For oceanic cumulus convective clouds, the effect of moisture and hygroscopic nuclei sources is very minor since conditions are usually quite constant in the subtropics. The thickness of the convective layer, though, which depends upon vertical moisture and temperature gradients, could affect the thickness of a cloud and thus its lifetime.

Cumulus Convection

Vul'fson (1955) made an intensive study of convective activity in cumulus clouds over Eastern Europe. He found the temperature profile in clouds to be the same as in the ambient air, but convection currents in clouds are substantially more intense than those in cloud-free air.

The concentration of convection currents in clouds decreased with height, whereas the scale increased to about the center of the cloud and then remained constant. Ascending motions predominated through almost the entire vertical extent of developing clouds.

Convective Cloud Dissipation

From 1956 to 1958, N. S. Shishkin studied the dissipation of convective clouds in various parts of the European USSR. He found clouds may dissipate either by (1) evaporation of cloud particles without precipitation, or (2) by the transformation of cloud particles into precipitation particles with subsequent "sweeping out" of the cloud by precipitation.

Dissipation by Evaporation

Dissipation by evaporation takes many forms, depending on atmospheric conditions— primarily lapse rates of temperature and humidity. The eddy diffusion of water vapor from a cloud into surrounding space is quite slow in calm air and evaporation of a thin cloud may take several hours, but unstable lapse rates may cause even thick convective clouds to dissipate rapidly. Shishkin observed a cloud 4-6 km thick to disappear completely in five to ten minutes.

Usually the upper parts of the observed clouds became flocculent and melted away during the initial minute or two of dissipation. The lower portion of the cloud, which has the greatest water content at the peak of cloud development, disappeared last.

The development of large-scale downward motions in clouds when the lapse rate is unstable $(\gamma_m < \gamma < \gamma_d)$ appeared to be most responsible for rapid dissipation. When a cloud mass descended, its temperature increased moist adiabatically. Therefore, downward motions in the cloud will lead to the rapid evaporation of a cloud if the cloud is small enough in horizontal extent to be contained entirely within the descending current (here the size dependence is a factor).

Dissipation by Precipitation

For 17 cases studied by Shishkin, the average time of dissipation by precipitation was 50 minutes, which is, on the average, seven times more slowly than clouds which dissipate by evaporation during development of downdrafts in an unstably stratified atmosphere. The table below illustrates three cumulonimbus cases studied.

Table 1

Case	Rate top sank during precipitation	Rate base rose due to sweeping out by precipitation
Cb #1	.15 m/s	.10 m/s
Cb #2	1.00 m/s	.50 m/s
Cb #3	.70 m/s	.20 m/s

Survey of the Literature

The semidiurnal cycle is a forcing function for much of the convective activity in the subtropics.

Riehl (1947) measured the periodic variations in cloudiness over the summertime subtropical Atlantic Ocean and found a very slight semidiurnal variation with a low cloudiness maximum at 0600 local time (34%) and a low cloudiness minimum around 2100 (32%). A secondary maximum around 1800 was also observed.

Riehl tested the hypotheses of Petterssen and Meinardus concerning radiative cooling effects but found that changes in low cloudiness were independent of both initial cloud cover and high cloud amount, which showed that both theories are presently inadequate.

Lavoie (1963) analyzed 2,719 days from a 10-year period (June 1949 - February 1959) for Eniwetok Island (11°N, 162°E) and obtained the same primary and secondary maxima as Riehl but slight seasonal time differences (rainy vs. dry). He suggested the semidiurnal cycle resulted from the diurnal heating and cooling cycle forcing low level wind velocity changes.

Garstang (1958) found similar maxima and minima over the open ocean from fixed ships in the subtropical Atlantic. A primary maximum occurred between 0700 and 0800 (48.5%) and a secondary maximum around 1300. The minimum changed from 1000 in 1957 to 0200-0300 in 1963 (26%). He could not account for the cycle occurring over open ocean either by radiation or surface heating, but suggested that three mechanisms control the distribution of cloudiness over the open ocean:

> (1) Radiation, which inhibits cloud growth over the ocean by day (Kraus, 1963) but enhances it at night in two different ways, according to the theories of Petterssen (1940) and Meinardus (1941);
>
> (2) Sensible Heat Transport, which can enhance cloud growth or dissipation by out-of-phase relationships between air and sea surface temperatures (which can force diurnal variations of wind velocity);
>
> (3) Atmospheric Tides, which relate directly to the semidiurnal pressure oscillation which produces a response in the windfield which in turn requires a semidiurnal cycle of vertical motion, and thus cloudiness.

A recent study by Brier and Simpson (1968) expanded on Garstang's results. They established a definitive statistical relationship between tropical cloudiness and rainfall and the semidiurnal solar atmospheric tide, as manifested in the semidiurnal surface pressure variation (using data from Batavia and Wake Island). The above "tide" was shown to enhance cloudiness and rain near sunrise and sunset, and to suppress them shortly after noon and midnight. Days with large five to six hourly pressure changes during certain time intervals (4 a.m. to 10 a.m., 10 a.m. to 4 p.m., etc.) had large cloudiness changes during these same periods relative to days with small five to six hourly pressure changes. The varying convergence-divergence field was suggested as the primary link between the semidiurnal solar atmospheric tide and cloud properties. It was also shown how the concentration of active cloud updraughts in the tropics can permit cloudiness to be extremely sensitive to small divergence fields.

An early attempt to determine a cloud's lifetime was made by Battan (1953) using a PPI-scope of 5-band search radar. Studying 67 rain clouds of sizes ranging from less than one to nearly three km in diameter, he found the mean duration of radar echoes to be 23 minutes with a mode of 22 minutes.

If the lifetime of the cloud itself is proportional to the duration of its rainshower (as suggested by theory and common sense), then Battan's results are quite significant for echoes smaller than three miles in diameter— duration increased directly with size. Convective clouds with higher tops (thicker clouds) lived proportionally longer than those with lower tops. The average maximum echo diameter was 2.2 miles; the maximum duration of radar cells rarely exceeded 40 to 45 minutes. A more recent study by Golden (1967), who used aircraft radar and satellite photographs, found that even for smaller echoes (3 to 5 mile diameter), showers were observed to persist for at least two hours.

The above lifetime applies only to radar (precipitating) clouds. Battan pointed out that actual clouds last longer, since these clouds may not be detected until they have built to the 15,000 foot level. Some visual cloud always remains after the radar echoes disappear.

Zipser and La Seur (1965) studied Tiros VII pictures and found a relationship between cloud size and brightness. Horizontal and vertical dimensions of convective clouds correlated positively, and an even stronger relationship existed between the brightness of cloud units and the depth of the convective layer.

It was suggested that the prevalence of conditional instability and ample moisture in most of the tropics is an important factor in the apparent sensitivity of tropical convection to small environmental changes.

Squires (1965) studied a number of subtropical convective clouds with diameters a few kilometers across and found them to last, on the average, for an hour or so.

Purpose of This Research

The purpose of this research is to study relationships between (cumulus) convective cloud lifetime with size, brightness and cloud top radiative cooling rate.

I have attempted to isolate clouds which are not associated with any general tropical or subtropical disturbance or system; thus, I can assume all of the other forementioned factors affecting a cloud's lifetime to be approximately constant. Atmospheric conditions in the BOMEX experimental region fall under the subtropical high pressure system throughout most of the summer months; thus outside influences are minimized.

Data Used

My primary source of data was ATS-III satellite pictures for the months of June and July 1969. These photographs, part of the University of Wisconsin Space Science and Engineering Center archive prints, came in booklets of three or more days each (5 to 20 pictures per day). With time intervals from 15 minutes to one hour between pictures, accuracy of lifetime estimates is assumed to be plus or minus one hour.

Cloud size was obtained from the pictures by eyeballing and subjectively assigning the cloud to one of seven categories. Cloud brightness was found in a similar fashion with special care taken to account for differences in picture quality reported.[2] Radiative cooling rates and cloudiness variations were taken from the "BOMEX Radiometersonde File" and "Marine Surface Observations," respectively.

Method of Investigation

I first devised a type of magnifier consisting of a magnifying glass mounted on three pegs to fix the glass at three inches from the pictures studied. This allowed for consistency in determining cloud sizes and better accuracy for deciding when a cloud was "born" or disappeared.

A BOMEX grid constructed for ATS-III pictures was then obtained and the precise locations of the fixed ships[3] were pinpointed for the following periods: 1) May 2-15, 2) May 24-June 10, 3) June 19-July 2, and 4) July 11-18.

During the first three periods, the ships had the following fixed positions:

Rainier	16°50'N	59°12'W
Rockaway	15°00'N	56°30'W
Discoverer	13°08'N	53°51'W

For the last period, the ships were moved to slightly different locations:

Rainier	17°30'N	54°00'W
Rockaway	13°00'N	54°00'W
Discoverer	07°30'N	52°42'W

In addition, the island station on Barbados (Paragon House), 13°00'N, 59°29'W, was used for each period. The use of a single island station along with the marine locations caused no apparent inconsistencies in the data. Figure 1 shows the gridded location of the stations used.

---

[2] Clouds from pictures which appeared to be uniformly brighter than normal were assigned to a lower category than they would have been had pictorial brightness differences been neglected.

[3] Five ships and an island station (Barbados) were used for the BOMEX project. These ships remained "fixed" to constant geographical coordinates during the first three BOMEX periods and then were moved to new coordinates for the fourth period.

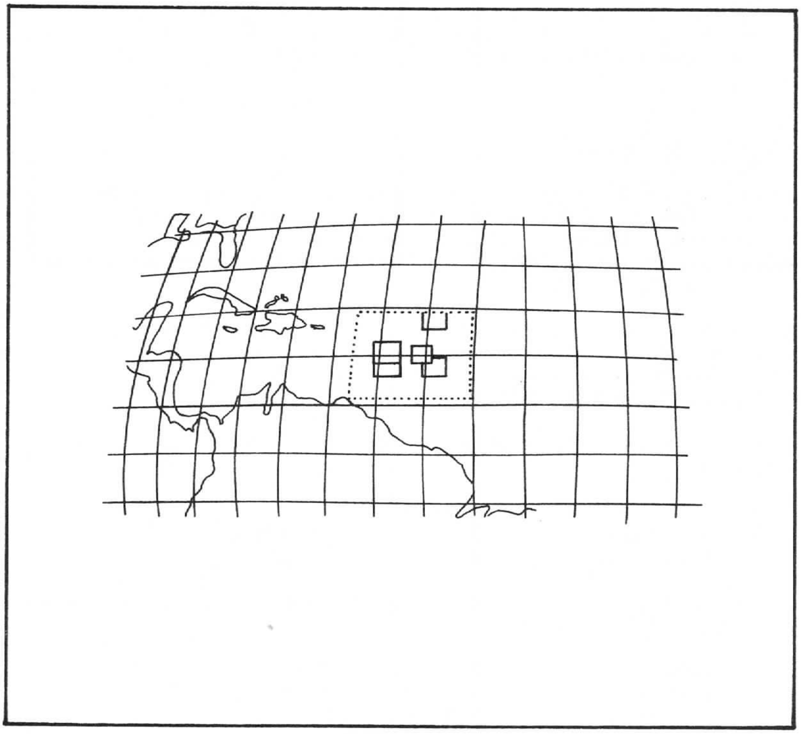

Figure 1. Gridded BOMEX experimental region and data station locations.

Isolated cumulus convective clouds within 10 km of the above stations were then studied and lifetimes determined to the nearest hour. Each cloud was classified according to size and brightness.

Sizes were divided into seven categories with diameters approximated geometrically from the pictures:

1.	VS	Very Small (1 1/2 - 3 miles in diameter)
2.	S	Small (3 - 4)
3.	SM	Small to Medium (4 - 5)
4.	M	Medium (5 - 6)
5.	ML	Medium to Large (6 - 7)
6.	L	Large (7 - 8 1/2)
7.	VL	Very Large (8 1/2 - 10)

Brightness was divided into seven categories of increasing magnitude according to an "eyeballing" classification:

1.	VD	Very Dim
2.	D	Dim
3.	DM	Dim to Medium
4.	M	Medium
5.	MB	Medium to Bright
6.	B	Bright
7.	VB	Very Bright

Radiative cooling values (in °C/day) were extracted from the BOMEX radiometersonde data which contained a profile measured daily at 2100 local time. Values atop the low layer of more than 90% relative humidity were used, since cloud top values were not identified. (Other cooling rates were also analyzed.)

Cloud lifetime was then correlated with size, brightness and cooling rate, and individual linear coefficients were computed. Other combinations of the data were also analyzed along with cloudiness data.

The following sources of error were encountered:

A. Satellite Picture Quality
    1. Resolution
    2. Large Nadir Angle (crowding of latitude-longitude lines near the horizon)
    3. Mistaking sunglint on water bodies for bright clouds
    4. Variations in brightness between pictures
    5. Failing to follow the same cloud in successive pictures

B. BOMEX Data Accuracy and Representativeness
    1. Observational (particularly nocturnal cloudiness amount data)
    2. Computational
    3. Transcriptive
    4. Instrumental (for relative humidity data)

C. Personal Bias
    1. Systematic (especially for sizes and brightnesses)

2. Classification of cloud size and brightness
3. Typographical
4. Assuming thickness and brightness associate well[4]

Results

The data were analyzed and graphs were drawn to show the relationships of cloud lifetime with size, brightness and cloud top radiative cooling rate. Other combinations of the data were examined and plotted in an attempt to ascertain all possible information. In addition, examples of the semidiurnal cycle were illustrated and discussed.

Lifetime vs. Size

Cloud lifetime (in hours) was linearly correlated with size (in miles). A positive correlation coefficient of 0.86 resulted from the 139 clouds studied as shown in Figures 2 and 3. This agrees with Battan's conclusion that for echoes less than three miles in diameter, lifetime is proportional to size (Figure 8).

It was found that for cloud sizes up to seven miles in diameter, a direct linear relationship occurs. For larger cloud diameters, another linear regression line exists with a more rapid increase in lifetime with increase in size.

Very small clouds had lifetimes less than one hour. This agrees with Squires' results which state that convective clouds less than a mile in diameter usually last an hour or less. Small clouds lived from less than one hour to over four; small to medium clouds lived between one and five hours; medium clouds lived between one and seven; medium to large clouds lived between one and nine; large clouds lived between two and ten; and very large clouds lived from eight to over ten hours.

Lifetime vs. Brightness

Lifetime was linearly correlated with brightness by a positive correlation coefficient of 0.89 for the 139 clouds shown in Figures 4 and 5. This agrees with Battan's result that thicker clouds live longer than thinner ones (provided thickness and brightness correlate strongly as concluded by Zipser and La Seur). This correlation is described again by two linear regression lines with the transition point around medium to bright. Lifetime increases more rapidly for brighter clouds.

---

[4] For ATS-viewed clouds, much of the change in brightness may be due to resolution effects of the spin scan photometer and to flare in the photographic products.

	SIZE											
LIFETIME	VS	S	SM	M	ML	L	VL	f_S	d_S	$f_S d_S$	$f_S d_S^2$	$f_{LS} d_L d_S$
0.0-0.9	3^{-45}	11^{-110}						14	5	70	350	-145
1.0-1.9		${}_{-8}20^{-150}$	${}_{-4}3^{-12}$	${}_{0}4^{0}$	${}_{11}1^{4}$			28	4	112	448	-168
2.0-2.9		${}_{-6}10^{-60}$	${}_{-3}8^{-24}$	${}_{0}3^{0}$		${}_{6}1^{6}$		27	3	81	243	-78
3.0-3.9		${}_{-4}1^{-4}$	${}_{-2}1^{-2}$	${}_{0}10^{0}$	${}_{2}4^{8}$	${}_{4}2^{8}$		18	2	36	72	10
4.0-4.9			${}_{-1}1^{-4}$	${}_{0}8^{0}$	${}_{1}3^{3}$	${}_{2}2^{4}$		14	1	14	14	11
5.0-5.9				${}_{0}2^{0}$	${}_{0}1^{0}$	${}_{0}2^{0}$		5	0	0	0	0
6.0-6.9				${}_{0}4^{0}$	${}_{-1}3^{-3}$	${}_{-2}2^{4}$		9	-1	-9	9	-7
7.0-7.9					${}_{-2}2^{-4}$	${}_{-4}4^{-16}$		6	-2	-12	24	-20
8.0-8.9					${}_{-3}1^{-3}$	${}_{-6}2^{-12}$	${}_{-9}2^{-18}$	5	-3	-15	45	-33
9.0-9.9						${}_{-8}3^{-24}$	${}_{-12}3^{-36}$	6	-4	-24	96	-60
10.0 +							${}_{-15}7^{-105}$	7	-5	-35	175	-105
f_L	3	42	13	36	15	18	12	TOTAL		218	1476	-595
d_L	-3	-2	-1	0	1	2	3					
$f_L d_L$	-9	-84	-13	0	15	36	36	-19				
$f_L d_L^2$	27	168	13	0	15	52	108	383				

$$r_{LS} = \frac{\overline{f_{LS} d_L d_S} - \left(\overline{f_L d_L}\right)\left(\overline{f_S d_S}\right)}{\sqrt{\overline{f_L d_L^2} - \left(\overline{f_L d_L}\right)^2}\ \sqrt{\overline{f_S d_S^2} - \left(\overline{f_S d_S}\right)^2}} = \frac{\frac{595}{139} - \left(\frac{218}{139}\right)\left(\frac{-19}{139}\right)}{\sqrt{\left[\frac{383}{139} - \left(\frac{-19}{139}\right)^2\right]\left[\frac{1476}{139} - \left(\frac{218}{139}\right)^2\right]}}$$

$$= +.86$$

Figure 2. Computational grid for determination of correlation coefficient for cloud size vs. lifetime.

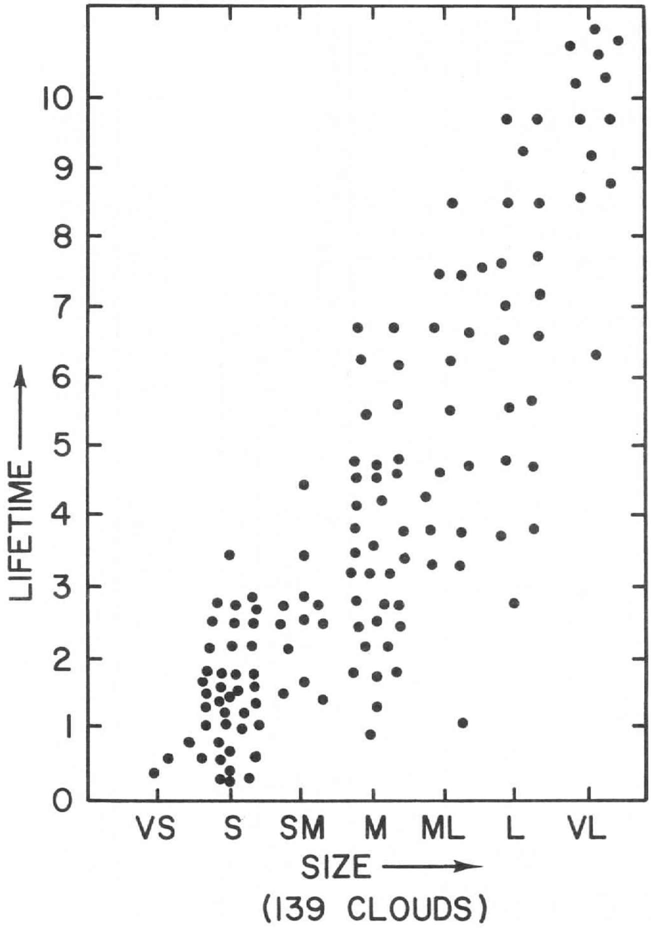

Figure 3. Scatter diagram for cloud size vs. lifetime.

	BRIGHTNESS											
LIFETIME	VD	D	DM	M	MB	B	VB	f_B	d_B	$f_B d_B$	$f_B d_B^2$	$f_{LB} d_L d_B$
0.0 - 0.9	${}_{-15}5^{-75}$	${}_{-10}10^{-100}$						15	5	75	375	-175
1.0 - 1.9	${}_{-12}1^{-12}$	${}_{-8}24^{-192}$	${}_{-4}2^{-8}$	${}_{0}1^{0}$				28	4	104	448	-218
2.0 - 2.9		${}_{-6}10^{-60}$	${}_{-3}9^{-27}$	${}_{0}4^{0}$	${}_{3}2^{6}$	${}_{6}1^{6}$		26	3	78	234	- 75
3.0 - 3.9		${}_{-4}1^{-4}$	${}_{-2}4^{-8}$	${}_{0}11^{0}$	${}_{2}1^{2}$	${}_{4}1^{4}$		18	2	36	72	- 26
4.0 - 4.9		${}_{-2}1^{-2}$	${}_{-1}1^{-1}$	${}_{0}7^{0}$	${}_{1}2^{2}$	${}_{2}2^{4}$		13	1	13	13	3
5.0 - 5.9				${}_{0}2^{0}$	${}_{0}1^{0}$	${}_{0}2^{0}$		5	0	0	0	0
6.0 - 6.9				${}_{0}4^{0}$	${}_{-1}1^{-1}$	${}_{-2}4^{-8}$		9	-1	- 9	9	- 9
7.0 - 7.9				${}_{0}1^{0}$	${}_{-2}3^{-6}$	${}_{-4}4^{-16}$		8	- 2	-16	32	- 22
8.0 - 8.9						${}_{-6}3^{-18}$	${}_{-9}1^{-9}$	4	- 3	-12	36	- 27
9.0 - 9.9						${}_{-8}4^{-32}$	${}_{-12}2^{-24}$	6	- 4	-24	96	- 56
10.0 +						${}_{-10}3^{-30}$	${}_{-15}4^{-60}$	7	- 5	-35	175	- 90
f_L	6	46	16	30	10	24	7	TOTAL	▨	210	1490	- 692
d_L	- 3	- 2	- 1	0	1	2	3	▨				
$f_L d_L$	-18	- 92	-16	0	10	48	21	- 47				
$f_L d_L^2$	54	184	16	0	10	96	63	413				

$$r_{LB} = \frac{\overline{f_{LB} d_L d_B} - (\overline{f_L d_L})(\overline{f_B d_B})}{\sqrt{\overline{f_L d_L^2} - (\overline{f_L d_L})^2}\;\sqrt{\overline{f_B d_B^2} - (\overline{f_B d_B})^2}} = \frac{\frac{692}{139} - \left(\frac{210}{139}\right)\left(\frac{47}{139}\right)}{\sqrt{\left[\frac{413}{139} - \left(\frac{-47}{139}\right)^2\right]\left[\frac{1490}{139} - \left(\frac{210}{139}\right)^2\right]}}$$

$$= +.89$$

Figure 4. Computational grid for determination of correlation coefficient for cloud brightness vs. lifetime.

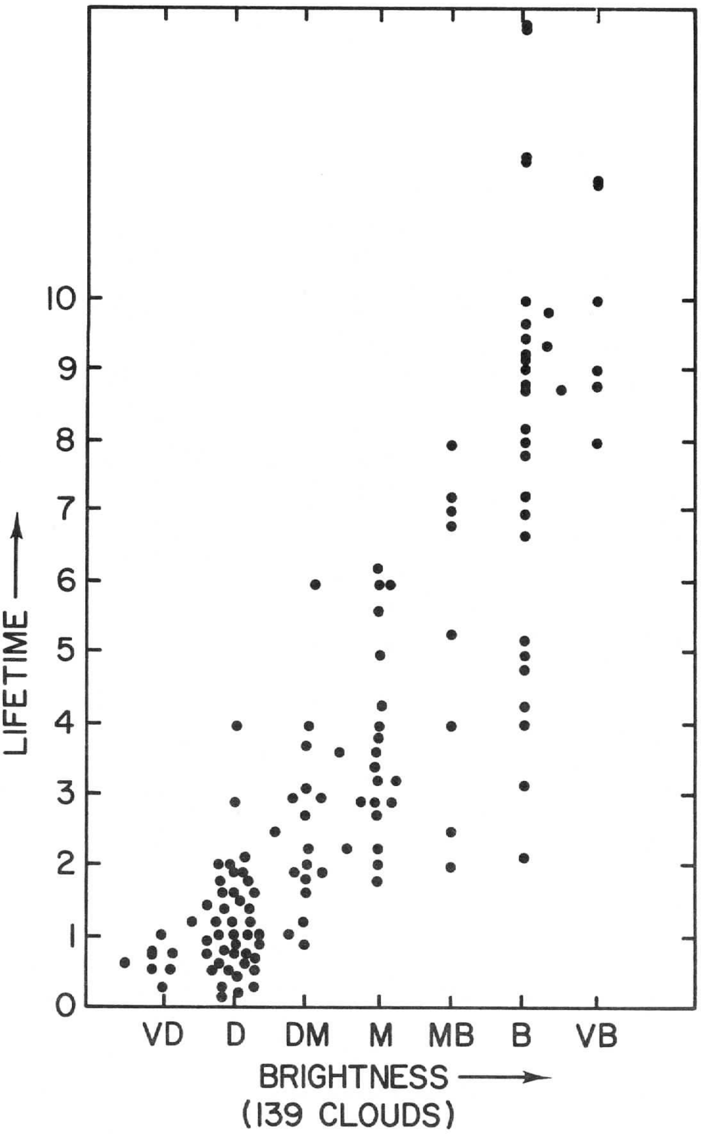

Figure 5. Scatter diagram for cloud brightness vs. lifetime.

Very dim clouds had lifetimes ranging from less than one hour to less than two hours; dim clouds had lifetimes from less than one hour to less than five; dim to medium clouds had lifetimes between one and five; medium clouds had lifetimes between one and eight; medium to bright clouds had lifetimes between two and eight; bright clouds had lifetimes from two to over ten; and very bright clouds had lifetimes from eight to over ten hours.

Lifetime vs. Cooling Rate

A linear correlation coefficient was computed for lifetime vs. radiative cooling rate. A positive correlation of 0.18 resulted for the 55 days studied, as shown in Figure 6.

The weak correlation is perhaps due to lack of representativeness of the cooling rates used. It was difficult to obtain actual cloud top rates for the clouds studied. The BOMEX values were taken from atop the low level high relative humidity layer. Thus for smaller clouds, one could not be sure the cooling rate value came from the cloud top or the cloud-free atmosphere (since ATS-III picture resolution is about two miles). Further study must be made with accurate cloud top cooling rates for results to be significant.

Other Relationships

Other combinations of data were analyzed in an effort to discover other possible relationships.

Size was found to correlate well with brightness (Figure 7) in agreement with Zipser and La Seur. No significant correlation existed between the following factors (as shown in Figures 9 to 12):

a) Surface maximum radiative cooling rate vs. low cloud amount

b) Low level atmospheric maximum cooling rate vs. low cloud amount

c) Low cloud top cooling rate vs. low cloud amount

d) Low level atmospheric maximum cooling rate vs. thickness of the low level high relative humidity layer.

A positive correlation did occur for cooling rate vs. thickness for clouds of lifetime less than one hour.[5] This indicates that cooling rate is definitely a factor of the lifetime of small clouds not affected by large-scale forcing systems (see Figure 13).

---

[5] Thickness here was obtained from BOMEX relative humidity profiles. The 24 clouds studied showed up in the profiles as near 100% relative humidity layers.

	COOLING RATE									
LIFETIME	0.0-1.5	1.5-3.0	3.0-4.5	4.5-6.0	6.0+	f_C	d_C	$f_C d_C$	$f_C d_C^2$	$f_{LC} d_L d_C$
0.0-0.9			${}_{0}\,2\,^{0}$	${}_{5}\,1\,^{5}$		3	5	15	75	5
1.0-1.9		${}_{-4}\,5\,^{-20}$	${}_{0}\,4\,^{0}$	${}_{4}\,3\,^{12}$		12	4	48	192	-8
2.0-2.9		${}_{-3}\,2\,^{-6}$		${}_{3}\,1\,^{3}$	${}_{6}\,1\,^{6}$	4	3	12	36	3
3.0-3.9	${}_{-4}\,1\,^{-4}$	${}_{-2}\,3\,^{-6}$	${}_{0}\,3\,^{0}$	${}_{2}\,3\,^{6}$	${}_{4}\,4\,^{16}$	14	2	28	56	12
4.0-4.9	${}_{-2}\,1\,^{-2}$		${}_{0}\,3\,^{0}$	${}_{1}\,1\,^{1}$	${}_{2}\,3\,^{6}$	8	1	8	8	5
5.0-5.9	${}_{0}\,1\,^{0}$		${}_{0}\,3\,^{0}$		${}_{0}\,1\,^{0}$	5	0	0	0	0
6.0-6.9			${}_{0}\,2\,^{0}$	${}_{-1}\,2\,^{-2}$		4	-1	-4	4	-2
7.0-7.9			${}_{0}\,1\,^{0}$			1	-2	-2	4	0
8.0-8.9						0	-3	0	0	0
9.0-9.9			${}_{0}\,1\,^{0}$	${}_{-4}\,1\,^{-4}$		2	-4	-8	32	-4
10.0+			${}_{0}\,1\,^{0}$		${}_{-10}\,1\,^{-15}$	2	-5	-10	50	-10
f_L	3	10	20	12	10	TOTAL	▨	87	457	1
d_L	-2	-1	0	1	2	▨				
$f_L d_L$	-6	-10	0	12	20	16				
$f_L d_L^2$	12	10	0	12	40	74				

$$r_{LC} = \frac{\overline{f_{LC}\, d_L d_C} - (\overline{f_L d_L})(\overline{f_C d_C})}{\sqrt{\overline{f_L d_L^2} - (\overline{f_L d_L})^2}\ \sqrt{\overline{f_C d_C^2} - (\overline{f_C d_C})^2}} = \frac{\left(\frac{1}{55}\right) - \left(\frac{87}{55}\right)\left(\frac{16}{55}\right)}{\sqrt{\left[\left(\frac{74}{55}\right) - \left(\frac{16}{55}\right)^2\right]\left[\left(\frac{45}{55}\right)\ \left(\frac{87}{55}\right)^2\right]}}$$

$$= +0.18$$

Figure 6. Computational grid for determination of correlation coefficient for cloud top radiative cooling rate vs. lifetime.

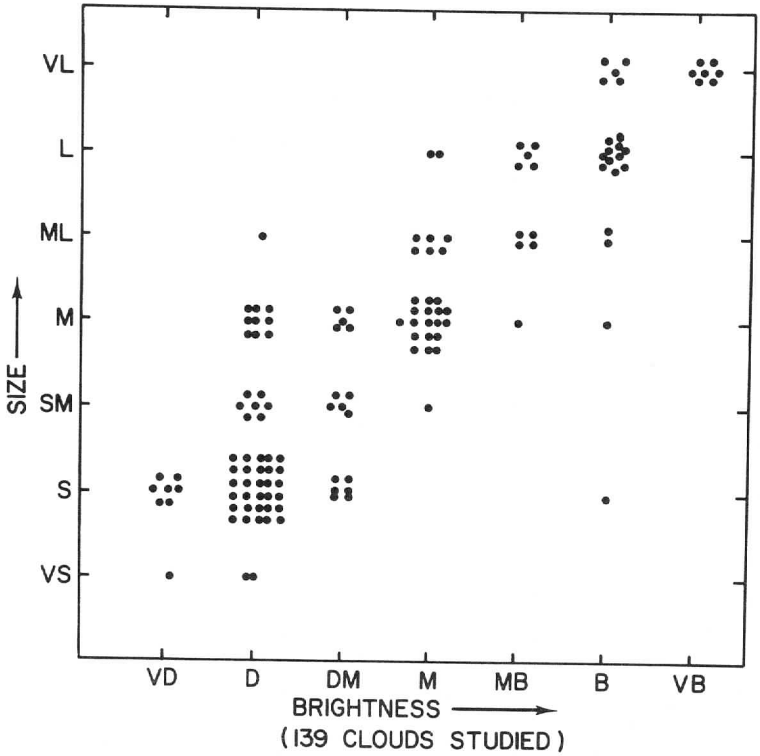

Figure 7. Scatter diagram for cloud size vs. brightness.

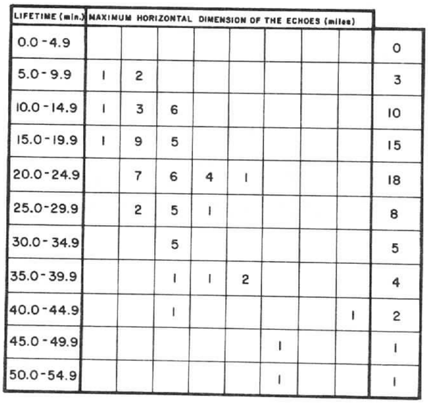

LIFETIME (min.)	MAXIMUM HORIZONTAL DIMENSION OF THE ECHOES (miles)								
0.0 - 4.9									0
5.0 - 9.9	1	2							3
10.0 - 14.9	1	3	6						10
15.0 - 19.9	1	9	5						15
20.0 - 24.9		7	6	4	1				18
25.0 - 29.9		2	5	1					8
30.0 - 34.9			5						5
35.0 - 39.9			1	1	2				4
40.0 - 44.9			1					1	2
45.0 - 49.9						1			1
50.0 - 54.9						1			1

CLOUD SIZE vs. LIFETIME

(67 CLOUDS STUDIED)

Figure 8. Battan's table of results for cloud size vs. lifetime.

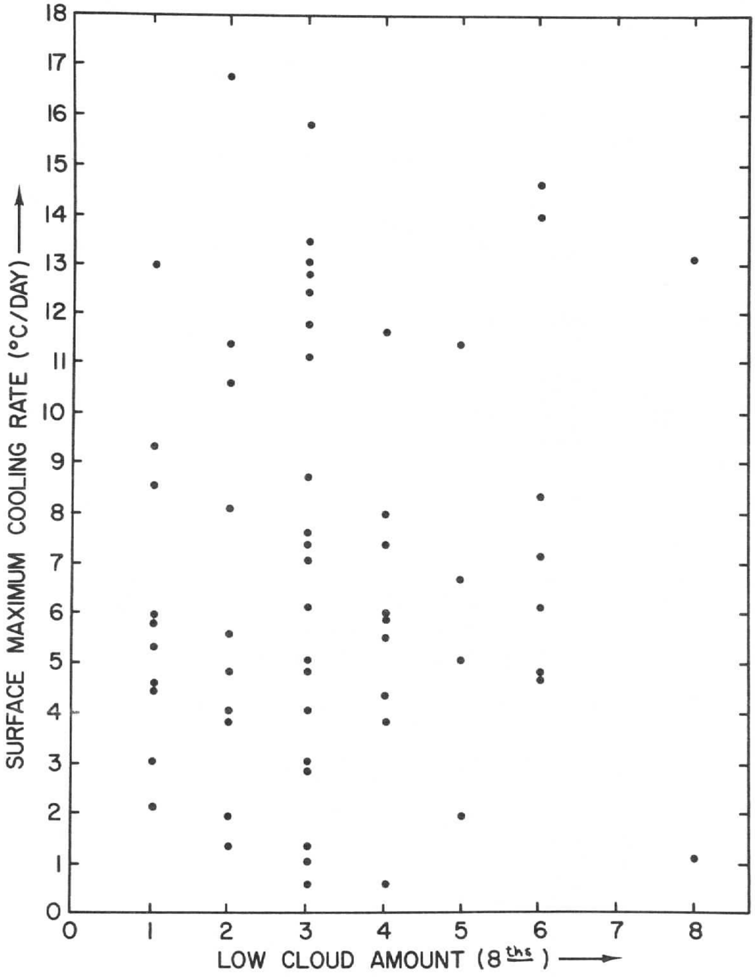

Figure 9. Scatter diagram for low cloud amount vs. surface maximum cooling rate.

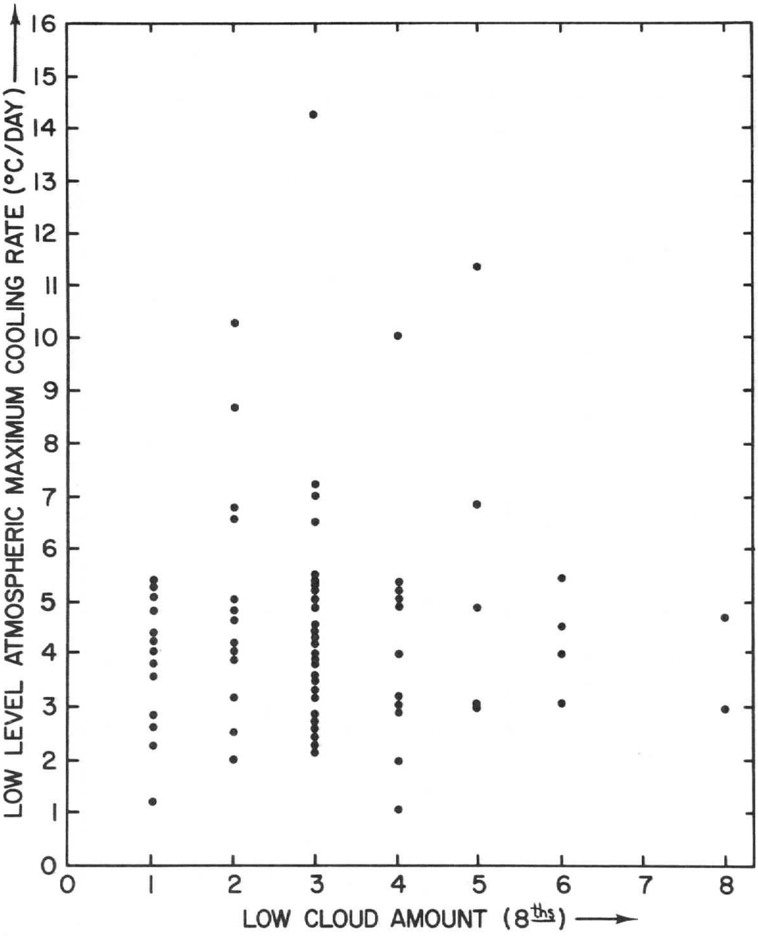

Figure 10. Scatter diagram for low cloud amount vs. low level atmospheric maximum cooling rate.

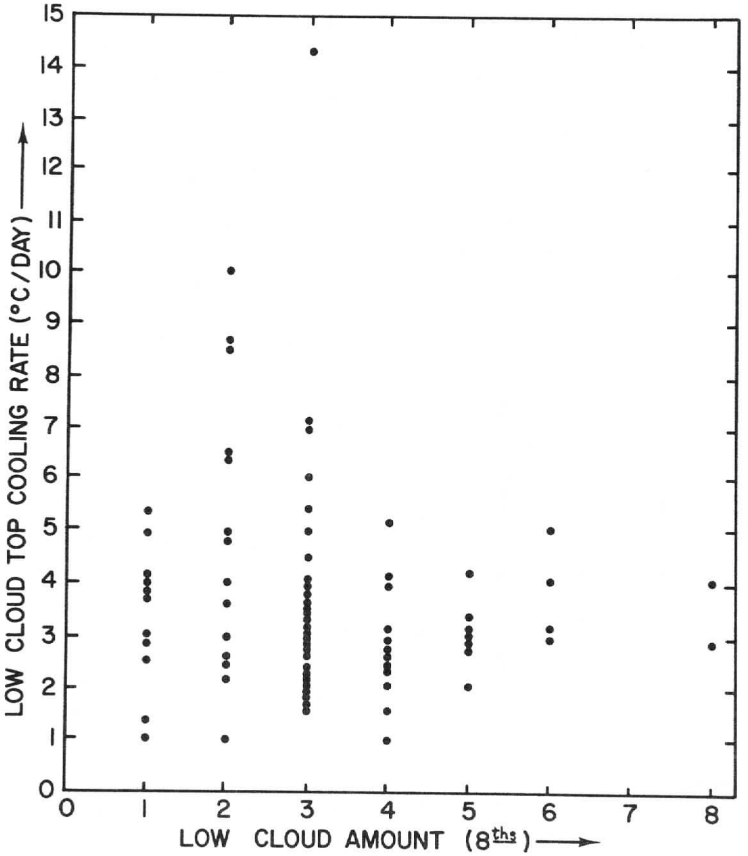

Figure 11. Scatter diagram for low cloud amount vs. low cloud top cooling rate.

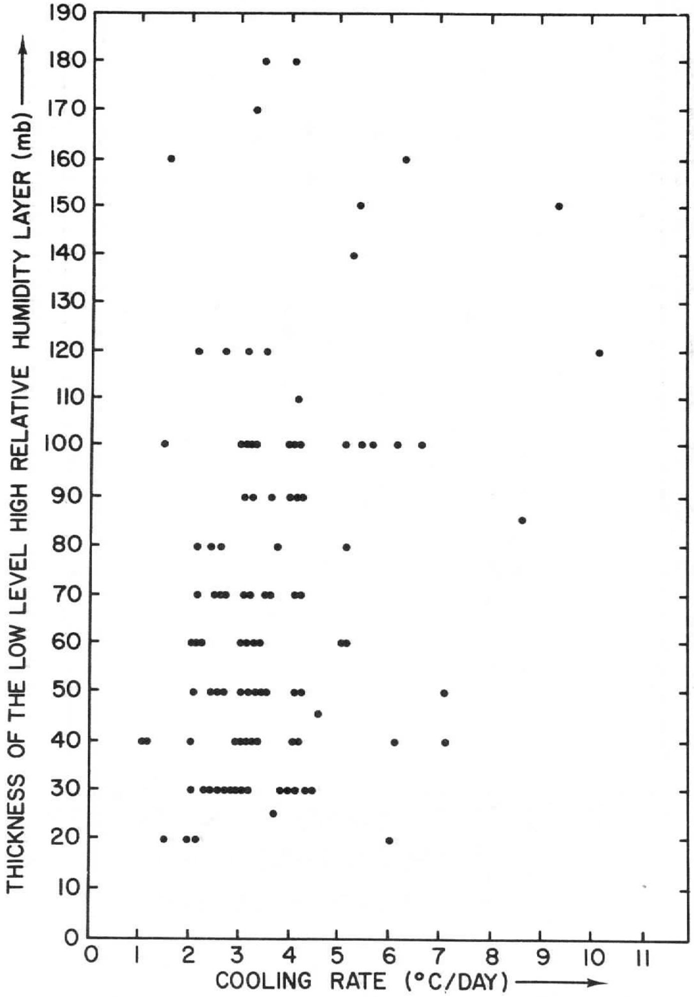

Figure 12. Scatter diagram for thickness vs. cloud top cooling rate.

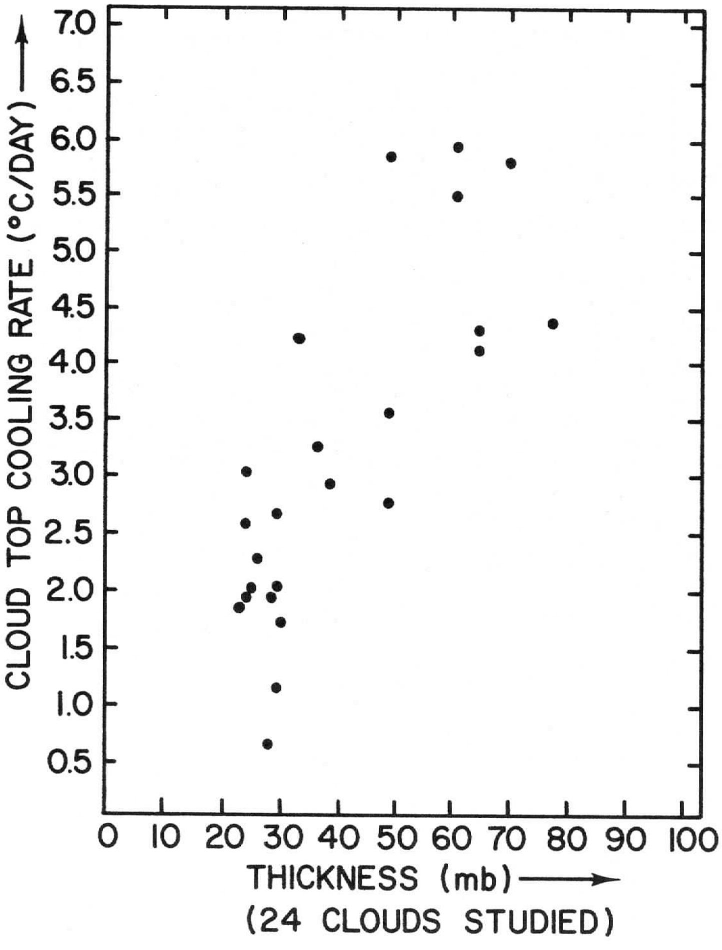

Figure 13. Scatter diagram for cooling rate vs. thickness of the low level high relative humidity layer.

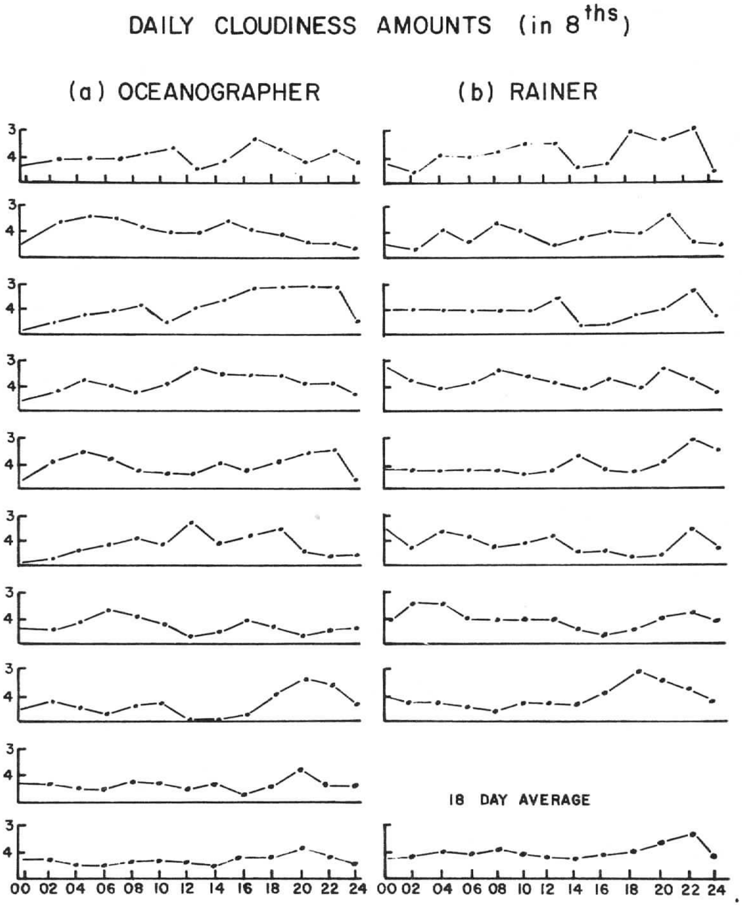

Figure 14. Examples of daily cloudiness amounts from the fixed ships: a) Oceanographer, b) Rainier.

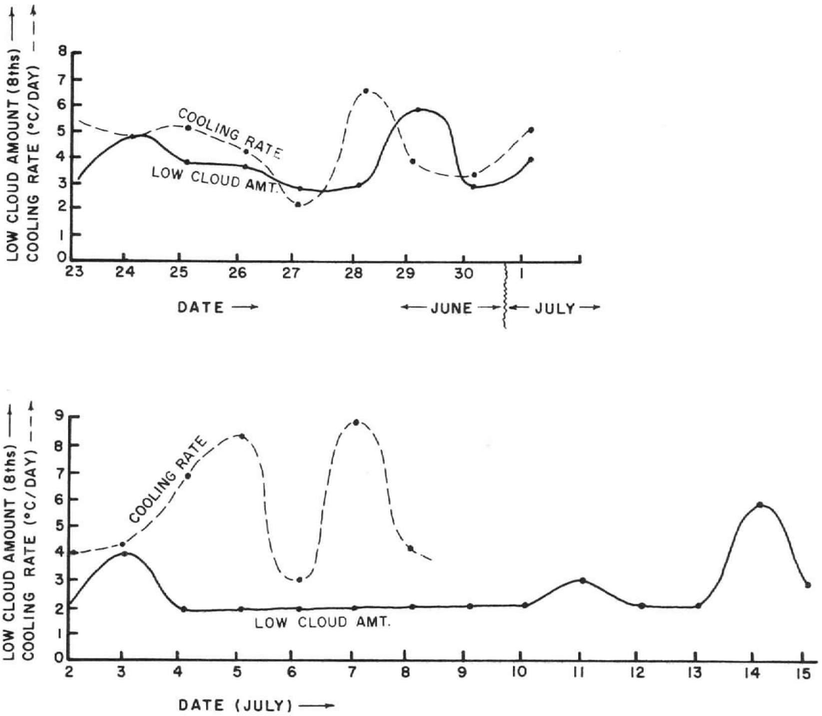

SHIP: ROCKAWAY

Figure 15. Daily averages for low cloud amount and radiative cooling rate from the fixed ship Rockaway.

Diurnal Cycle

Cloudiness amount data from the fixed ships Oceanographer and Rainier were analyzed for 18 days with values recorded at two-hour intervals. An approximately semidiurnal cycle was found to exist with a very distinctive primary maximum (66%) having an average occurrence at 2200 local time and a primary minimum (38%) following shortly after midnight. A secondary maximum (51%) was present but varied between 0400 and 0800. A rather consistent secondary minimum (42%) occurred around 1400.

Figure 14 might cause some questions regarding the accuracy of the nocturnal estimates. Visual cloud observations are very difficult at night and systematic bias related to such things as phase of the moon can be argued, for example. Perhaps the severity of the primary maximum and minimum with respect to the time interval between them could be attributed to factors not reported in these data, such as a change of observers shortly before midnight. One finding favoring the significance of the results is the fact that they agree well with both the daylight and nocturnal values of Brier and Simpson (1969) discussed earlier. This, along with the consistency of the extremes, leads one to conclude that a semidiurnal cycle does exist but with perhaps less intense primary maxima and minima.

Figure 15 illustrates daily averages for low cloud amount and radiative cooling rate from the fixed ship Rockaway (for late June and early July). No apparent cycles occur for this data.

Conclusions

This study indicates that a significant relationship exists between cloud size, brightness and lifetime for subtropical oceanic convective clouds. No conclusions can be reached regarding radiative cooling rate, but evidence suggests it may affect lifetimes, especially for smaller clouds. A semidiurnal cycle of cloudiness amount can be observed in the BOMEX region, but the accuracy of nocturnal data is questionable.

ACKNOWLEDGMENTS

I wish to thank my advisor, Dr. Verner E. Suomi, for his stimulation, support and patience. Thanks must also go to Dr. H. H. Lettau for his help in review of this thesis and to Dr. David Martin for his constructive criticism. I would also like to acknowledge Dr. D. N. Sikdar for his many helpful suggestions in carrying out this research.

References

Aspliden, D. and Landers, F., 1965: Satellite Study of the Tropical North Atlantic, Department of Meteorology, Florida State University.

Battan, L. J., 1953: "Duration of Convective Radar Cloud Units," Bulletin of the American Meteorological Society, Vol. 34, No. 3, pp. 227-228.

Brier, G. W. and Simpson, J., 1969: "Tropical Cloudiness and Rainfall Related to Pressure and Tidal Variations," Quarterly Journal of the Royal Meteorological Society, Vol. 95, No. 403, pp. 120-147.

Byers, H. R., 1965: "Cloud Dynamics," Elements of Cloud Physics, University of Chicago Press, Chicago, Ill.

Cox, S. K., 1967: "A Radiation Model in which the Effects of Clouds are Simulated from Moisture and Temperature," Ph.D. Thesis, Department of Meteorology, University of Wisconsin.

Cox, S. K., Vonder Haar, T. and Huson, J., 1968: "Measurement of Solar Radiation Absorption in Tropical Atmospheres," Department of Meteorology, University of Wisconsin, Preliminary Results.

Cox, S. K., 1968: "Observational Evidence of Anomalous I.R. Cooling in a Clear Tropical Atmosphere," Department of Meteorology, University of Wisconsin.

Darkow, G., 1963: "A Study of Infrared Radiation Measurements in the Vicinity of the Subtropical Tropopause," Ph.D. Thesis, Department of Meteorology, University of Wisconsin.

Fletcher, N. H., 1962: The Physics of Rain Clouds, Cambridge University Press, Cambridge, Massachusetts, pp. 15-30.

Golden, J. H., 1967: "The Life Cycle of Convective Cloud Systems as Portrayed by Radar and Tiros Photographs," Department of Meteorology, Florida State University, Technical Note No. 67-3.

LaSeur, N. E. and Garstang, 1964: "Tropical Convective and Synoptic Scale Weather Systems and their Statistical Contributions to Tropical Meteorology," Department of Meteorology, Florida State University, Final Report on the Observational Field Program to U.S. Army Research and Development Laboratory.

Mancuso, R. I. and Endlich, R. M., 1968: "Objective and Dynamic Analysis of Tropical Weather," Stanford Research Center, Semiannual Report No. 1

Meinardus, W., 1941: Ann. Hydr. Marine Meteorology, Vol. 69, No. 37.

Petterssen, S., 1940: Weather Analysis and Forecasting, Vol. II, McGraw-Hill Book Co., New York, pp. 133-175.

Riehl, H., 1947: "Diurnal Variation of Cloudiness over the Subtropical Atlantic Ocean," Bulletin of the American Meteorological Society, Vol. 28, No. 1, pp. 37-40.

Schutz, P. and Fritz, A., 1961: "Cloud Streets over the Caribbean Sea," Monthly Weather Review, Vol. 89, No. 10, pp. 375-382.

Vul'fson, N. I. and Levin, N. M., 1965: Studies of Clouds, Precipitation, and Thunderstorm Electricity, American Meteorological Society, Boston, Massachusetts, Feb., 1965; especially: Shishkin, N.S., "Investigation of the Dissipation of Convective Clouds," pp. 147-160; and Vul'fson, N. I., "Study of Convective Activity in Cumulus Clouds," pp. 133-146.

Zipser, E. J. and LaSeur, N. E., 1965: "Distribution and Depth of Convective Clouds over the Tropical Atlantic Ocean Determined from Meteorological Satellite and Other Data," Department of Meteorology, Florida State University, Final Report to the National Environmental Satellite Center, ESSA, Grant WBG 36, Dec., 1965.

APPENDIX A

Cloud Data

Date	Ship	Sz	Br	Lf	Sz	Br	Lf	Sz	Br	Lf	C.R.
June 1	Disc	M	D	2	S	D	1				2.7
1	Roc	M	DM	3	s	D	1½	S	D	½	3.7
10	Barb	VL	B	10							3.3
11	Barb	L	ML	5	ML	M	3	ML	M	4	3.2
11	Barb	M	M	2							3.2
12	Barb	ML	B	6	M	M	5	L	B	6	3.7
20	Disc	S	D	1	SM	DM	3	S	D	½	1.0
20	Roc	M	M	6	S	DM	2				10.1
22	Disc	S	D	¼	M	D	1	L	B	9	5.4
22	Barb	SM	D	2	S	D	1				2.5
23	Barb	M	DM	4	S	D	2				3.7
23	Roc	VL	VB	9							5.4
24	Roc	L	B	3	M	M	2				4.8
24	Barb	S	D	1½							2.6
24	Disc	L	M	4							4.4
25	Rain	M	M	3½	M	M	3	S	D	1½	2.4
25	Roc	S	B	2	M	B	4	S	D	1	5.3
26	Barb	M	M	3	ML	MB	7				3.6
27	Roc	M	M	3½							2.3
28	Roc	SM	DM	2	ML	M	4				6.3
28	Rain	ML	MB	4	T	B	6				3.1
29	Rain	ML	M	3							2.1
29	Barb	SM	DM	1							4.0
29	Roc	S	D	1	S	D	½	M	D	2	4.0
30	Roc	S	D	1	SM	D	2	S	D	½	3.5
30	Disc	ML	M	6							2.8
30	Rain	M	M	2							2.6
30	Barb	L	MB	7							2.9
July 1	Barb	ML	MB	7							2.3
1	Rain	VL	VB	14							7.3
1	Disc	S	D	½	M	D	1				3.0
1	Roc	S	D	2	S	D	1	SM	D	1	5.2
2	Barb	VL	VB	12	S	VD	1½	S	VD	1	3.3
2	Barb	S	VD	½							3.3
11	Roc	M	D	4	S	D	3	SM	D	2	6.8
12	Roc	L	B	4	VL	B	10				4.2
12	Barb	VS	D	½	S	D	1	VS	VD	½	5.0
13	Roc	M	D	1	ML	M	3				4.8
13	Disc	S	VD		S	D	1	SM	D	1	3.2
13	Rain	M	M	3	M	DM	3				3.0
14	Rain	M	D	1	S	D	1				3.0
14	Roc	VL	B	10	L	B	9	VL	B	10	1.2
14	Disc	VL	B	9	L	B	9				3.0
14	Barb	S	D	1	M	MB	2½				6.1
16	Barb	ML	D	1½							4.0
17	Rain	M	DM	3	M	M	6	S	D	2	6.5
17	Disc	S	VD	½	M	M	5	M	M	6	3.6

Appendix A (continued)

Date	Ship	Sz	Br	Lf	Sz	Br	Lf	Sz	Br	Lf	C.R.
July 17	Roc	M	DM	6	SM	D	2				5.3
18	Barb	SM	DM	4							3.5
18	Rain	VL	VB	16							7.1
20	Rain	L	MB	7	L	MB	8	M	M	4	4.0
21	Barb	M	D	2	S	DM	1				5.0
22	Barb	ML	MB	6							3.0
22	Rain	M	M	3	M	M	4	S	DM	2	5.0
22	Rain	VS	D	½							5.0
22	Disc	M	DM	2	S	D	1	S	VD	½	4.1
23	Rain	L	MB	2	S	DM	1	S	VD	½	4.5
23	Disc	VL	B	8	SM	DM	2				14.3
24	Barb	M	M	3	L	M	3				4.3
24	Disc	L	B	7	L	B	5				4.4
26	Barb	ML	M	3	ML	B	7	SM	M	2	3.6
26	Barb	L	B	8							3.6
26	Disc	SM	DM	2	S	D	1				4.6
27	Barb	VL	VB	8	L	B	7	VL	VB	9	2.0
27	Disc	S	D	2	M	M	4	S	DM	2	2.6
27	Disc	M	MB	4							2.6
27	Rain	S	D	1	S	D	½	S	D	1	4.2
27	Rain	M	D	2							4.2

Appendix B

Other Data

Date		Ship	Th	Co	SC
May	2	Roc	30	2.4	4.8
	5	Roc	150	8.6	4.8
	5	Rain	40	3.0	5.7
	6	Rain	60	3.2	3.8
	6	Roc	70	2.5	10.7
	25	Roc	40	1.0	16.8
	25	Rain	120	3.0	0.6
	26	Rain	20	1.5	24.6
	26	Roc	100	1.3	5.4
	27	Barb	200	4.0	0.0
	28	Barb	50	4.0	33.0
	30	Roc	70	3.0	-73
	30	Disc	90	3.0	5.1
	31	Disc	120	3.3	13.1
	31	Barb	20	5.9	2.8
June	1	Rain	50	7.0	8.7
	1	Disc	70	2.1	15.3
	1	Roc	30	2.3	13.1
	2	Disc	110	4.0	-5.0
	3	Disc	90	3.8	5.8
	3	Barb	25	3.8	25.0
	4	Barb	50	3.2	13.0
	5	Barb	70	3.4	5.5
	5	Roc	150	8.6	4.0
	6	Roc	70	2.5	10.7
	6	Disc	60	5.0	2.2
	7	Disc	70	4.0	11.2
	7	Barb	50	4.0	13.2
	7	Roc	120	10.0	8.1
	9	Barb	70	2.5	1.3
	9	Rain	180	3.7	1.3
	10	Barb	50	3.2	4.4
	11	Barb	40	3.0	0.7
	12	Barb	60	3.5	9.7
	20	Disc	400	1.0	11.2
	20	Roc	80	2.1	-3.8
June	22	Disc	60	5.0	8.2
	22	Barb	50	2.5	10.2
	23	Barb	160	1.3	-0.2
	23	Roc	100	5.4	1.3
	24	Roc	50	3.3	0.0
	24	Disc	180	3.2	1.2
	24	Barb	30	3.6	6.0
	25	Barb	30	2.6	-.8
	25	Rain	30	2.2	2.0
	25	Roc	30	4.1	8.0
	27	Roc	50	2.3	12.8
	28	Roc	100	6.0	2.8
	28	Rain	70	2.5	-0.6
	29	Rain	70	3.0	11.3
	29	Barb	100	4.0	2.5
	29	Roc	30	4.0	14.0
	30	Roc	20	2.0	12.0
	30	Disc	80	2.8	12.9
	30	Barb	100	2.9	9.2
	30	Rain	30	2.5	-1.7
July	1	Rain	50	7.0	8.7
	1	Barb	50	0.0	2.0
	1	Roc	50	2.5	5.5
	1	Disc	170	3.0	1.0
	2	Barb	50	3.3	-3.1
	11	Roc	100	6.5	1.4
	12	Barb	150	5.0	5.3
	13	Roc	100	4.0	4.5
	13	Disc	30	3.0	13.5
	13	Rain	80	8.5	3.7
	14	Rain	60	2.0	4.3
	14	Barb	40	6.1	-0.5
	14	Roc	40	1.0	5.4
	14	Disc	40	3.0	20.5
	16	Barb	70	4.0	1.3
	17	Disc	30	2.0	0.2
	18	Rain	40	7.1	11.3

Data Key:

Th = Thickness (in mb)
Co = Low level maximum radiative cooling rate (in °C/day)
SC = Surface radiative cooling rate (in °C/day)
Th = Thickness of the low level high relative humidity layer (mb)
C.R. = Cloud top radiative cooling rate (°C/day)
Lf = Cloud lifetime (hours)
Br = Cloud brightness
Sz = Cloud size

APPENDIX C

Cloudiness Amount Data (in eighths)

Ship: Oceanographer

Date		00	02	04	06	08	10	12	14	16	18	20	22
June	1	3	4	4	4	5	6	2	4	8	6	4	6
	2	3	6	7	7	5	4	4	6	5	4	2	2
	3	1	2	3	4	5	2	5	6	8	8	8	8
	4	2	3	5	4	3	5	8	7	7	7	6	6
	6	2	5	6	5	3	2	2	4	3	5	6	7
	7	1	1	2	4	5	4	8	4	5	6	2	1
	23	2	3	2	1	3	3	0	0	1	5	7	6
	24	3	3	4	6	5	4	1	2	4	3	1	3
	25	3	3	2	2	3	3	2	3	1	2	5	3
	26	3	3	2	2	3	3	3	2	4	4	5	4
Ship: Rainier													
May	3	3	2	4	4	5	6	6	2	3	8	7	8
	4	2	1	5	3	6	5	2	3	4	4	7	2
	6	4	4	4	4	4	4	6	1	1	3	4	7
	13	7	5	4	5	7	6	5	4	5	4	7	6
June	1	3	3	3	3	3	2	3	5	3	2	4	8
	2	6	3	6	5	3	4	5	2	2	1	1	6
	3	3	6	6	4	4	4	4	2	1	2	4	5
	4	4	3	3	2	1	3	3	3	5	8	7	6
Average		3.1	3.3	4.0	3.8	4.1	3.9	3.8	3.3	3.9	4.0	4.8	5.2

UPPER TROPOSPHERIC ISOBARIC TEMPERATURE AND HEIGHT FIELDS OVER THE TROPICAL ATLANTIC FROM SATELLITE INFRARED SPECTROMETER SOUNDINGS

D. N. Sikdar and R. S. Cram

ABSTRACT:

This paper presents mean maps of upper tropospheric temperature and constant-pressure height fields constructed from SIRS (Satellite Infrared Spectrometer) data for the period June-July 1969. These tropical Atlantic data were gathered for both clear and cloudy atmospheres.

Temperature analyses at seven pressure levels above 500 mb revealed generally cooler temperatures over the continental areas and warmer temperatures over the ocean. Constant-pressure height profiles indicated lower values over the continents in contrast to higher values over the ocean. With increasing cloud amount, the area of high height values shrank while areas of low height values expanded and became more dominant, suggesting a profound influence of cloud cover on the constant-pressure height profiles. The scatter diagrams of height versus percent cloud cover in the instrument field of view also suggest that increases in percent cloud cover and greater cloud thickness are related to decreases in height of all constant-pressure surfaces above and below cloud top levels.

1. Introduction

The Satellite Infrared Spectrometer (SIRS) experiment flown on Nimbus-III has recorded many temperature and height profiles. These SIRS soundings have been used extensively in daily NMC analyses, especially in the data-sparse oceanic regions. The statistical technique involved in extracting these data from eight spectral bandpasses between 11 and 15 microns, have been discussed by Smith et al. (1970). Results of their comparison with radiosonde data were presented according to the age of the satellite and the cloud conditions. Recently, Hayden (1971) compared constant-pressure height data with height data obtained from conventional radiosondes and found that thickness values had approximately the same accuracy at high levels.

These findings suggest that reasonable climatological maps depicting temperature and constant-pressure height fields can be obtained from the SIRS soundings, at least for tropospheric levels above 500 mb. Also, by grouping the daily soundings in 10° (latitude-longitude) squares, any periodic temperature variations in the upper troposphere which may be related to the passage of easterly waves (Riehl, 1945) or Rossby gravity waves (Yanai, et al., 1968; Sikdar and Suomi, 1971) can be investigated. With these two objectives in mind, a set of SIRS soundings for the BOMEX period—June and July, 1969—covering the tropical Atlantic were obtained from Dr. William L. Smith, National Environmental Satellite Service (NESS), NOAA. (See Figure 1.) Data for June covered only the ocean area while the July data included both land and ocean regions.

Examination of the data showed that large gaps in time occurred between soundings in the same 10° squares, and soundings for even two or three consecutive days in the same square were rare. The data bank therefore appeared unsuitable for a study of periodic temperature variations in the upper troposphere. Consequently, the SIRS soundings were employed to construct mean temperature and geopotential height fields in both clear and cloudy environments. Also, the effects of cloud cover on the mean height fields were investigated.

2. Data Analyses

The SIRS data listing gave the date, time and location of each sounding, cloud top pressure, percent cloud cover in the field of view, and the temperature and geopotential height at several pressure levels. For the present study the data were divided into three parts: clear (2% or less cloud cover in the field of view); cloudy (80% or greater cloud cover); and a June-July mean which considered all the data irrespective of cloud amount. Approximately 1350 soundings were obtained for the two-month period. The soundings were arranged in a grid from 20°N - 20°S latitude and 80°W - 0° longitude. The grid was further divided into 10° squares, each square containing 8 to 95 samples. A subset of these data, arranged by the date of each sounding, yielded from one to eight samples in each 10° square. Of the 61 possible days of coverage for any grid square, the maximum number of days with available data was 28 while the minimum was five. However, data coverage over two or three consecutive days rarely occurred.

The SIRS field of view is approximately 220 km square and temperature and height values represent an average over this area. Results from several studies by Smith and Woolf (1969) show that 70% of the discrepancies between SIRS soundings and radiosonde-observed temperature and geopotential height are less than 2°C and 50 meters respectively. Upon close examination of the SIRS data for June and July, 1969, approximately 10% of the samples were found to have values much higher or lower than the remaining data. Because several of the 10° × 10° grid boxes contained only a few samples, these few erroneous data values produced large discrepancies in the resultant mean field. To eliminate the few inconsistent points, only soundings within one standard deviation of the mean in each grid square were employed to construct the mean fields. This procedure has reduced the data volume but will hopefully improve upon the confidence in the results.

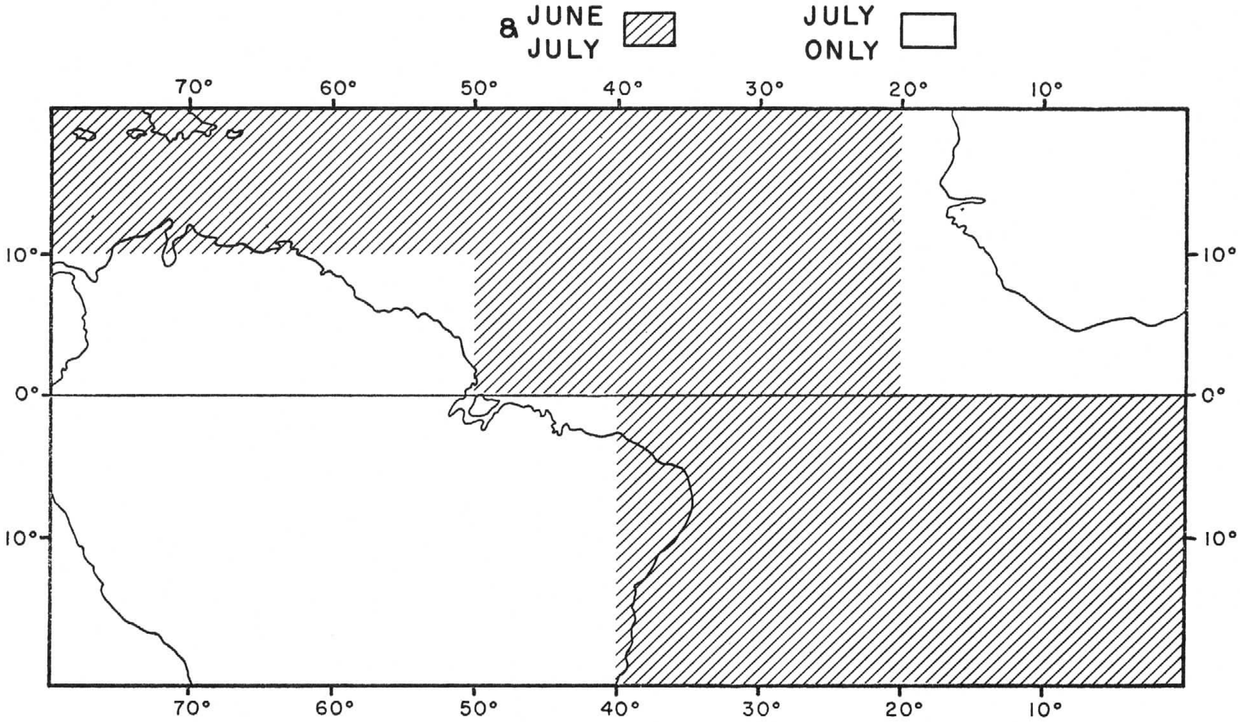

Figure 1. SIRS Data Coverage

To prepare the mean temperature and height fields for seven pressure levels (500, 400, 300, 250, 200, 150, 100 mb), the data in each grid square were averaged, plotted on a mercator projection, and hand analyzed. This resulted in a set of seven maps for each of the three cases investigated (June-July; mean, clear, cloudy).

With decreasing pressure at the surface, one expects more rising air and greater cloud development in the area. In order to examine how well the SIRS data reflect on these features, the soundings were grouped according to cloud-top pressure and a scatter diagram of height versus percent cloud cover in the field of view for each constant pressure surface was prepared for four cloud-top levels (850, 700, 500 and 400 mb). A least square fit line was drawn by computer to show the tendency of height as the percent cloud increased.

3. Results of the Analysis

Temperature Profiles

Temperature patterns for seven pressure levels obtained from the clear case soundings are presented in Figure 2. The mean fields in general show cooler temperatures over South America and western Africa and warmer temperatures over the equatorial Atlantic. These patterns persist throughout the seven pressure levels. However, a warm cell begins to develop over Venezuela at 250 mb and expands eastward and northward at higher levels until at 100 mb the warm region has extended to include most of the zone above 10°N latitude. Also, the warm region off the coast of Brazil extends westward at 100 mb to include most of the latitudinal zone below 10°S. In fact, although the warm air over the tropical Atlantic dominates through the 150 mb layer, at 100 mb the cold air has taken over most of the central portion of the grid (10°N - 10°S), while the warmer regions are pushed poleward. Interestingly, one finds a significant meridional temperature gradient at the 500 mb level off the west coast of Africa near the ITCZ at the location proposed for GARP Atlantic Tropical Experiment (GATE) in 1974. Over eastern Brazil there is a similar gradient persisting to 150 mb.

Figure 3 presents the temperature distribution at the same seven pressure levels for the cloudy case. These fields must be interpreted with caution. The SIRS data listing specifically states that soundings with cloud cover in excess of 10% at 500 mb or above are of less reliability. This set of maps was composed entirely from data with cloud cover at 80% or greater in the satellite field of view. Even though these analyses may be less reliable, they appear to be consistent throughout all the levels in the upper troposphere. In contrast to the clear air soundings in Figure 2, there is a dominating cold cell centered near 5°N, 35°W which extends from 500 mb through 150 mb. Two weak warm cells are present in its vicinity at 500 mb: one to the east, disappearing above 400 mb,

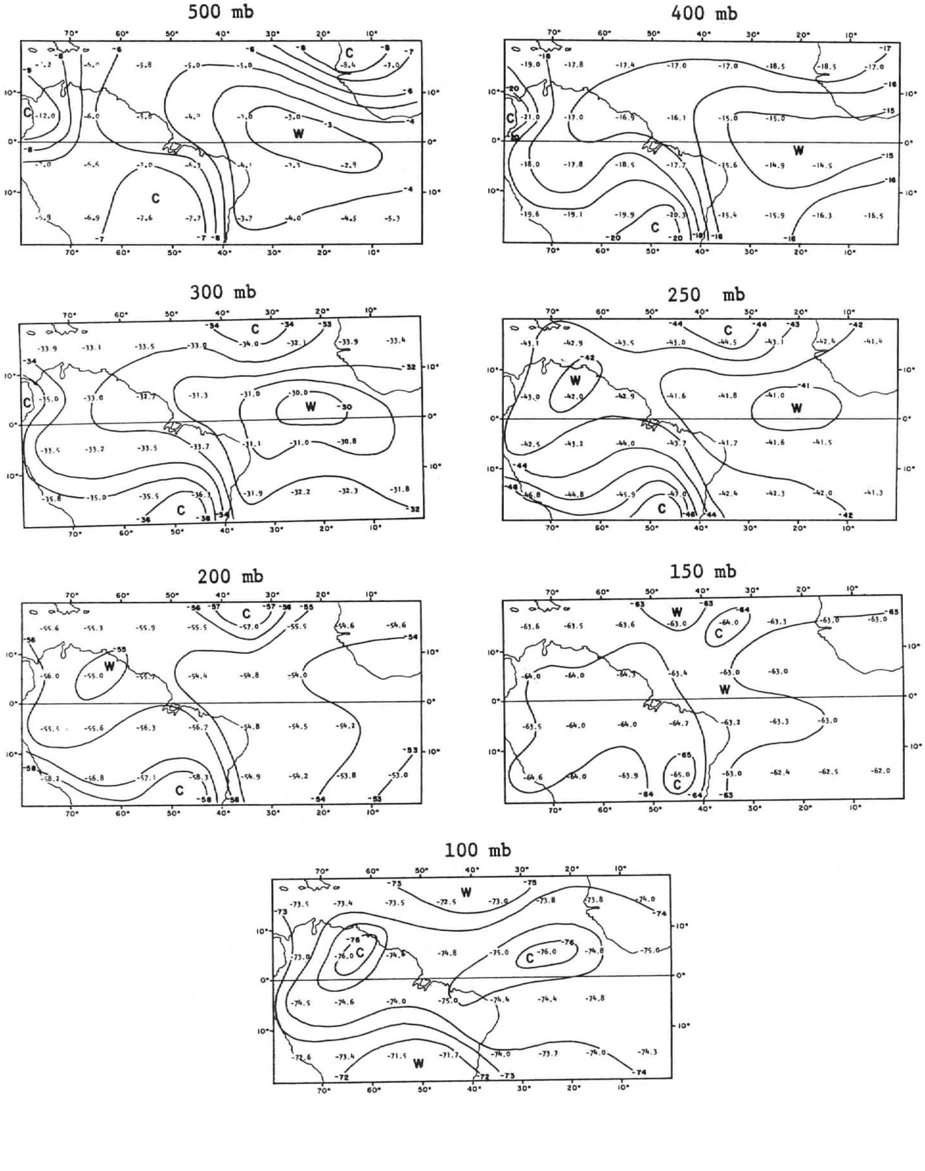

Figure 2. Mean temperature profiles at seven pressure levels from "clear case" SIRS soundings.

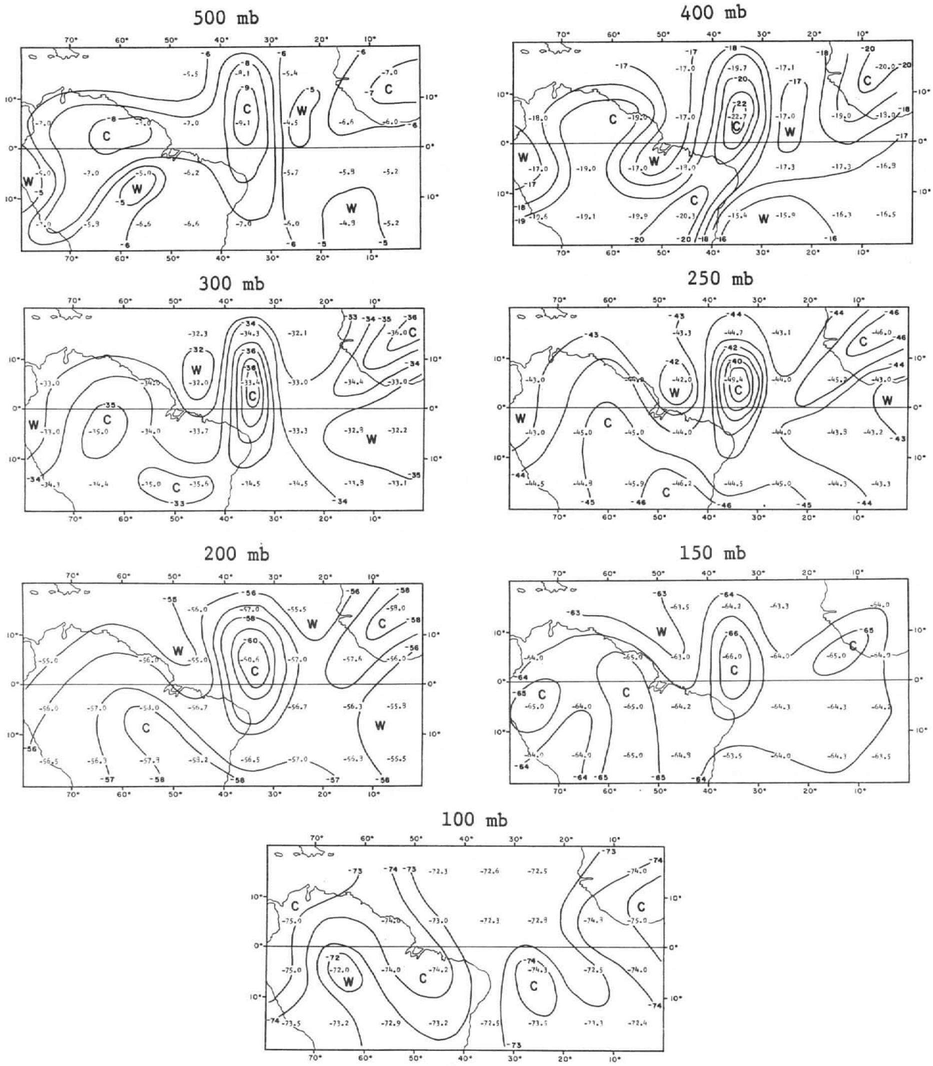

Figure 3. Same as in Figure 2 but for "cloudy" cases.

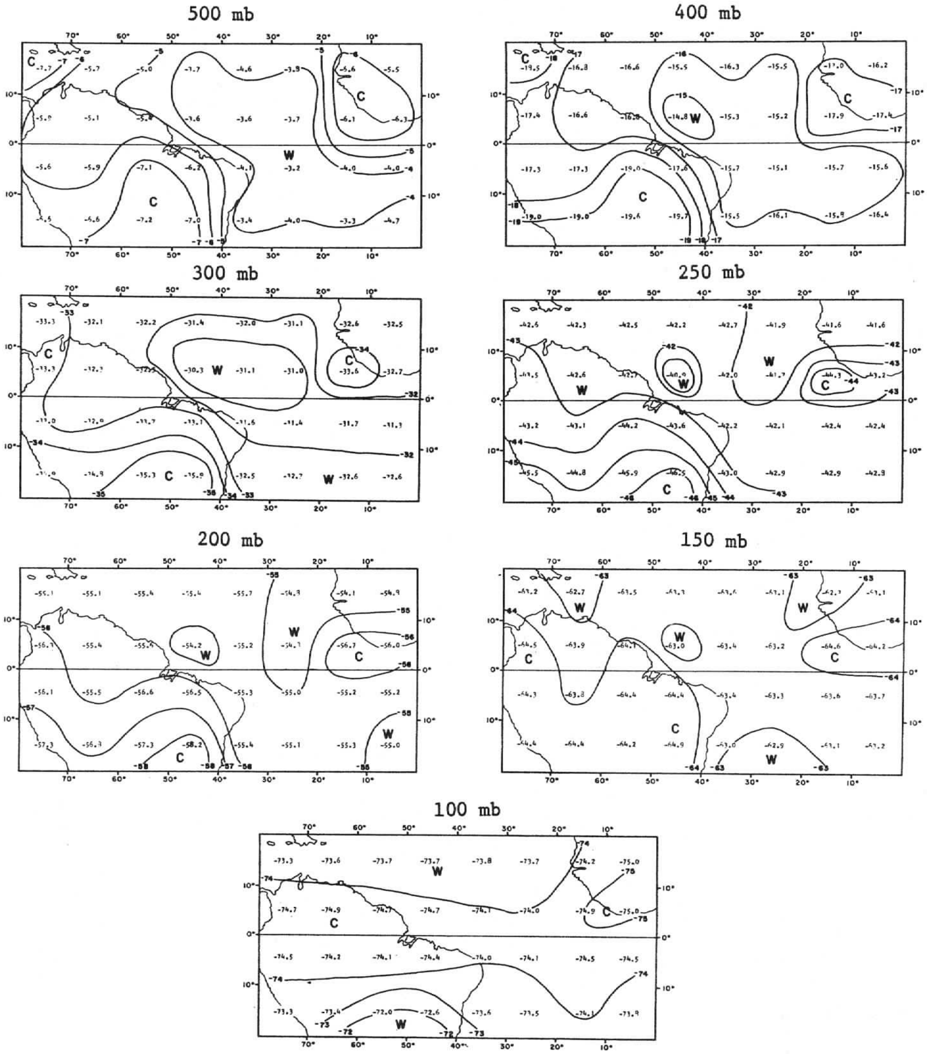

Figure 4. Same as in Figure 2 but for all soundings.

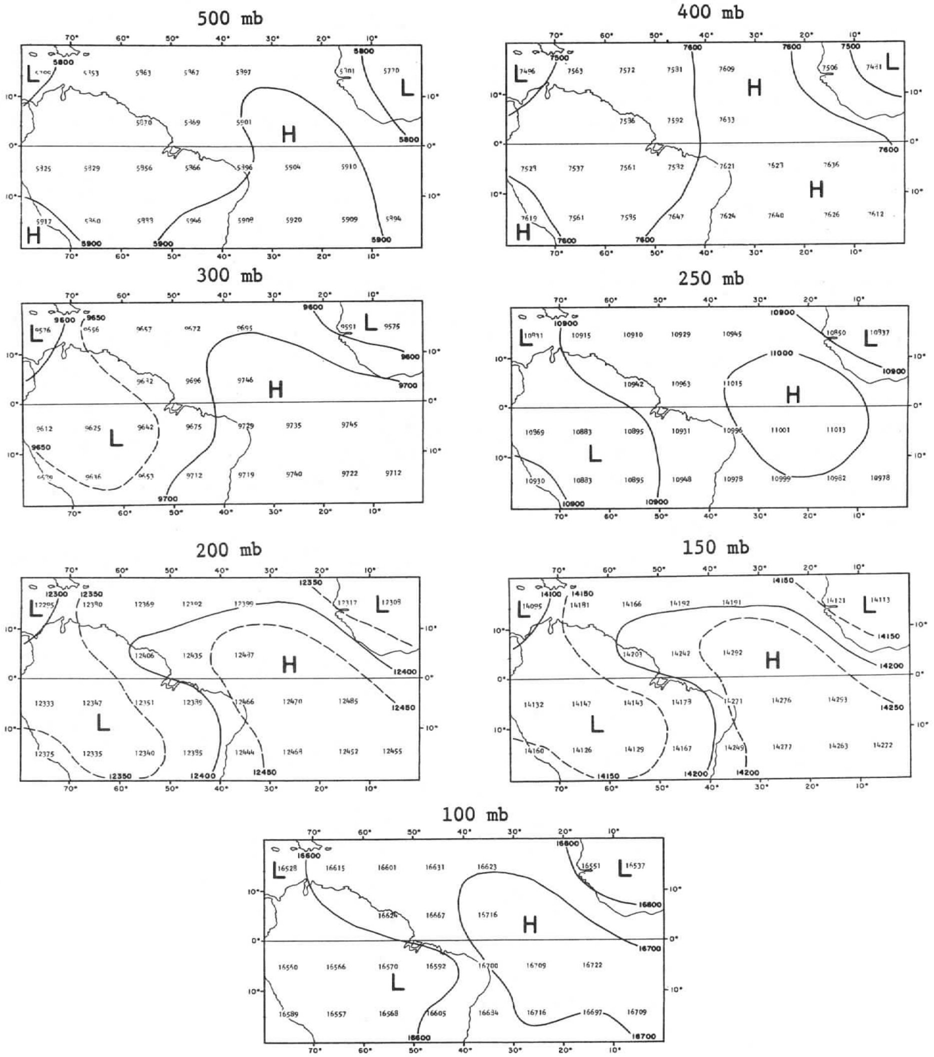

Figure 5. Mean geopotential height profiles at seven pressure levels from "clear case" SIRS soundings.

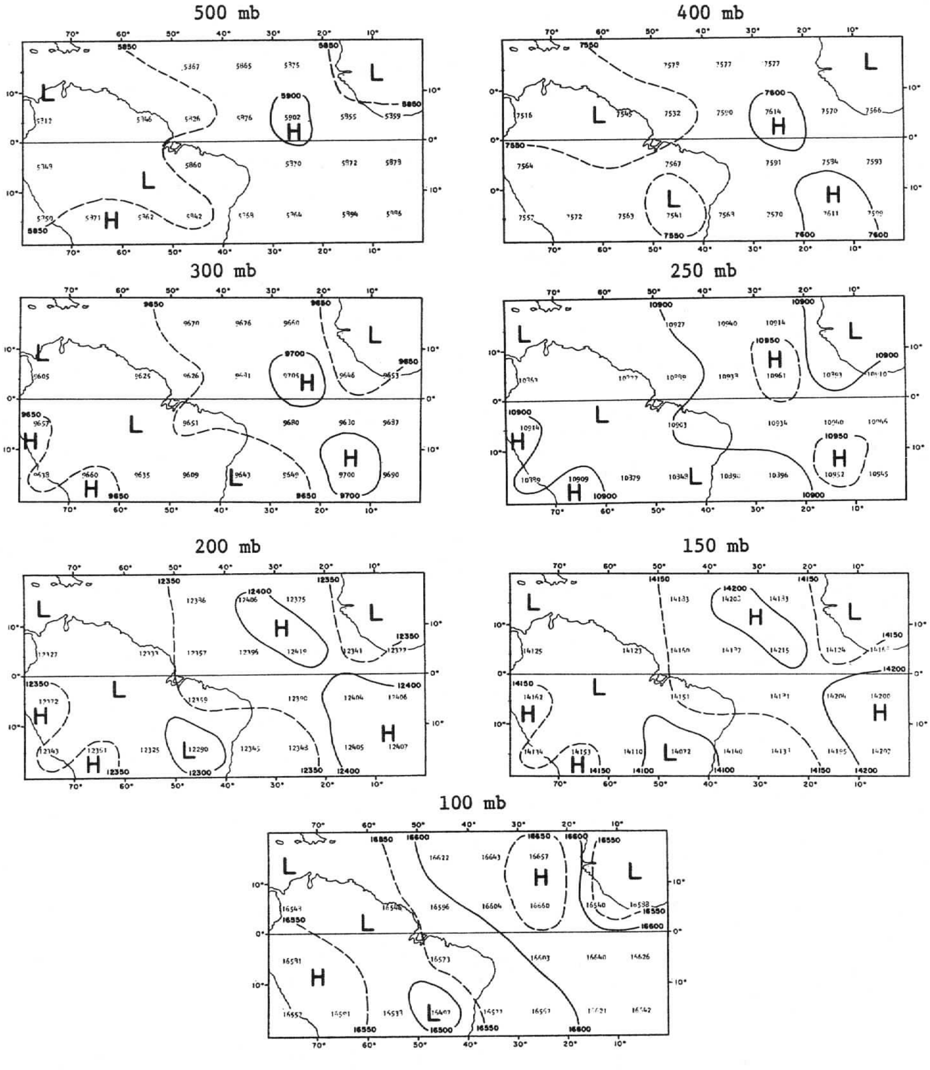
500 mb

400 mb

300 mb

250 mb

200 mb

150 mb

100 mb

Figure 6. Same as in Figure 5 but for "cloudy" cases.

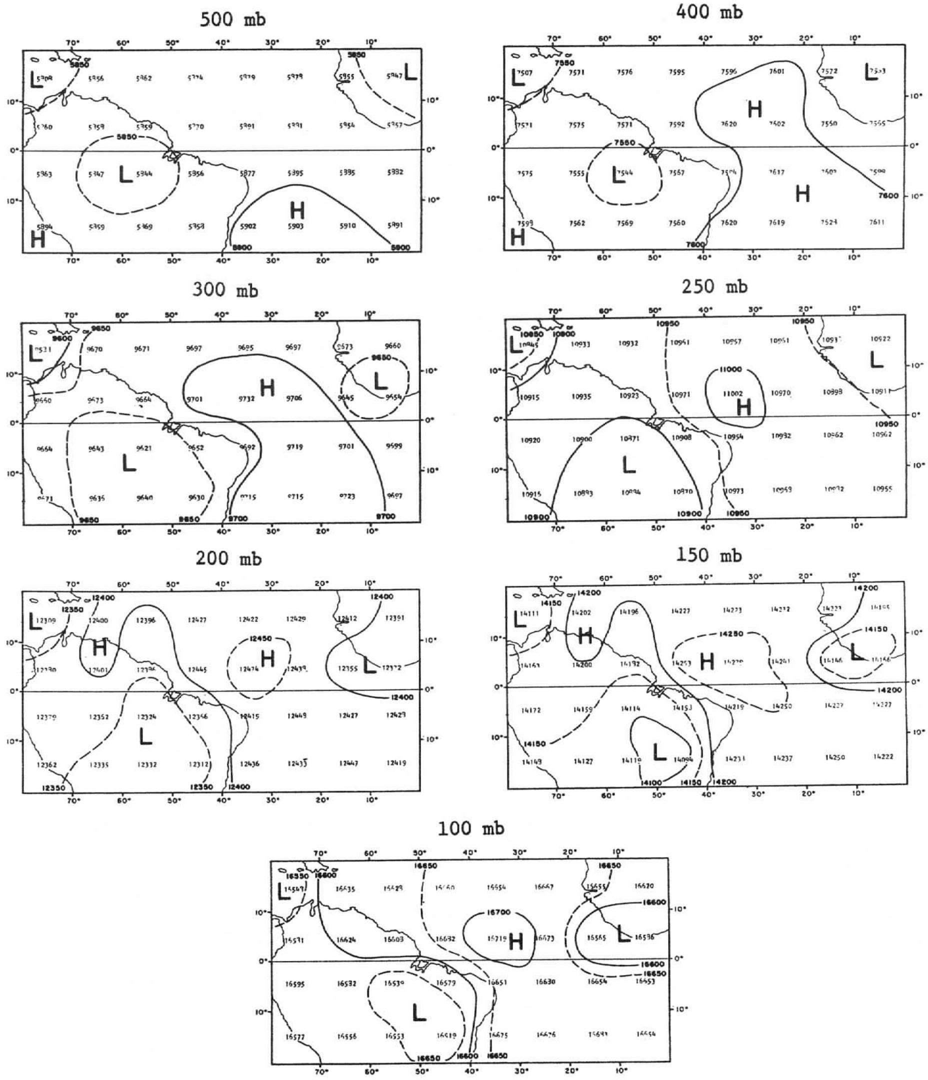

Figure 7. Same as in Figure 5 but for all soundings.

while the other to the west continues through the 150 mb level. Obviously, a strong meridional temperature gradient exists in the region. At the 500 mb surface two cold cells are seen: one over northern South America and the other over western Africa. The South American cell expands to cover most of the continent within the grid boundary and persists through 150 mb where a warm tongue enters from the southwest to dominate most of the region at 100 mb. The cold cell over western Africa remains throughout the upper troposphere. A warm region over the southeast Atlantic continues through the 200 mb layer. The general temperature distribution more or less reverses at the 100 mb level showing some agreement with the temperature fields in Figure 2. A meridional gradient is again seen south of Guinea in the eastern Atlantic, as noted for the clear air soundings.

A set of maps prepared from all the SIRS soundings irrespective of their cloud amount is presented in Figure 4. These maps include soundings with percent cloud cover ranging from 0 to 100%. The temperature patterns agree very well with the clear case at all pressure levels and the effect of the dominant cold cell in the equatorial Atlantic discussed in the previous paragraph has apparently been averaged out. The only significant difference between the mean June-July maps and those composed of only clear air soundings is that the clear case seems to be about one degree warmer over the ocean areas. A more detailed study of this set of temperature maps is left to the reader.

Constant-pressure Height Profiles

Presented in Figures 5, 6 and 7 are height analyses for the clear, cloudy and mean June and July cases, respectively. The dominant features on the clear case analyses are a large region of greater heights over the tropical Atlantic Ocean areas and two regions of lower heights over the continents of South America and western Africa. The large high over the ocean is consistent throughout the seven constant pressure surfaces, showing the greatest extent at the 150 mb level and yet, curiously, remaining over the ocean. As can be seen in Figure 5, the contour lines indicating the high region follow the continental boundaries almost exactly. This probably indicates that the warmer land surfaces produce much stronger vertical motions than the cooler adjacent ocean. Stronger vertical motions may cause a lower pressure and, hence, lower height values at a constant-pressure surface. The strong contrast seen between land and ocean in Figure 5 is not, however, depicted in the NAVAIR climatic means, although this may be due to their much more sparse data network. One low area centered in the South Caribbean at 500 mb, becomes more and more extensive as pressure decreases until at 300 mb and above, the low includes most of the South American continent within the grid. The other low, centered in west Africa, maintains itself throughout the upper troposphere. Another small high can be seen at 500 mb off the coast of Peru.

In Figures 6 and 7 are seen the analyses of cloudy and all June and July soundings. Both show the same general features seen in the clear case. The high centered in the tropical Atlantic for the all-soundings case is somewhat less extensive, and the area encompassed by the largest closed contour line is noticeably smaller than those shown for the clear case. The same is also true for the cloudy case (Figure 6): the high centers are smaller than those of both the clear and all-soundings cases and height values are 50 meters or more lower in the cloudy case than the other cases, especially above 300 mb. Lower height regions over the continents show an opposite behavior. In the all-soundings analyses, the center of the low heights over South America is more extensive at all pressure levels than those shown in the clear analyses (Figure 5). The low center over west Africa is also more dominant and extends off the coast above the 300 mb level. The same comments apply to the low areas shown in the cloudy case. They appear to be somewhat larger than those of the other two cases at any constant pressure surface.

Some discrepancies do exist in the three cases, even though the gross features pointed out above dominate the height analyses. The smaller high center in Figure 5 off the coast of Peru can also be seen at the 500 mb level of the June-July and cloudy cases. This high is very much smaller and disappears above 400 mb in the June-July case while in the cloudy case this high becomes much more extensive at 300 mb and covers most of western South America at the 100 mb level. Another discrepancy can be seen in the June-July analyses where a tongue of greater heights develops at 200 mb over Venezuela and extends through the 100 mb level. This Venezuelan high center is not indicated in either the clear or cloudy cases. Otherwise, the patterns depicted in the three sets of height analyses are quite similar.

4. The Relationship of Cloud Cover in the SIRS Field of View to the Geopotential Height

To study in greater detail the effects of cloud cover on the height of a constant-pressure surface, the SIRS data were arranged in sets according to the cloud top pressure. The cloud top levels used were 850 mb, 700 mb, 500 mb and 400 mb. A scatter diagram of height versus percent cloud in the satellite field of view was computer-produced and a line of least squares fit drawn for each set of data. For each cloud top pressure group, seven scatter diagrams were constructed, one for each constant pressure surface examined in the discussion of height fields above. The scatter diagrams are presented in Figures 8-14. Each figure includes the four diagrams of successively higher cloud tops for one of the constant pressure surfaces; i.e., Figure 8 gives the four diagrams for the 500 mb surface, Figure 9 gives the four diagrams for the 400 mb surface, and so on. In this manner the effects of higher cloud as well as cloud amount on the height of any one constant pressure surface can be readily seen. Note that while the percent cloud increases from left to right along the abscissa, the heights increase from top to bottom on the ordinate. Also, thinner dashed lines on the diagrams represent one standard deviation from the mean of all the points in the analysis, not to be confused with the thicker line of least squares fit.

The lines of least squares fit show that as the amount of cloud in the field of view increases, there is a tendency for the height of the constant pressure surface to decrease. This is evident in all the cases presented except for the lowest cloud top (850 mb) at the 500 mb and 400 mb pressure surfaces where the lines are nearly horizontal, indicating no change in height with greater cloud amounts. Otherwise, all the remaining data very consistently indicate a decrease in height with an increase in cloud.

A close examination of the intercepts on the height axes and the slopes of the lines of least squares fit reveal some interesting features. The intercepts and slopes of the least squares lines are given in Table 1 for each cloud top and constant pressure surface. The intercept on the height axis indicates the height of the pressure surface when no clouds are present. Therefore, for any constant pressure surface the height intercepts must be the same, regardless of the cloud top, a necessary condition if the data are to be considered valid. A look at the range of the intercepts at each pressure surface yields very small differences—12 to 31 meters—which is well within the 50-meter accuracy of the SIRS instrument (Smith and Woolf, 1969). We can also see from the diagrams and Table 1 that for each cloud top the slopes of the least squares lines become steeper for successively lower pressures. This indicates that a given percent of cloud will have an increasingly greater effect on the height of pressure surfaces at increasingly higher altitudes; e.g., 30% cloud cover with tops at 500 mb will have a greater effect on the 200 mb constant pressure surface height than on the 400 mb constant pressure surface. A similar negatively increasing slope is seen for each constant pressure surface as the height of the cloud top increases. Since the majority of the clouds in the tropics are cumuliform, greater cloud tops imply greater thickness. We may conclude from these scatter diagrams that for greater amounts and thicknesses of clouds over an area, the heights of constant pressure surfaces typically decrease.

5. Conclusions

The available SIRS data were found to be inadequate for a study of periodic temperature variations in the upper troposphere due to the lack of consecutive daily time intervals over a given area. However, climatological mean maps of temperature and constant-pressure height fields were developed with quite reasonable results. Also, while the effects of individual cloud clusters on temperature or constant-pressure surfaces could not be examined in detail, some general conclusions could be drawn concerning the relationship between cloud amount and thickness and the heights of constant pressure surfaces. In order to study the effects of clouds on their immediate surroundings in greater detail, much higher resolution data and many more soundings consistent in both time and interval and location will be necessary.

Temperature analyses at seven different constant pressure surfaces in the tropical upper troposphere in general revealed cooler temperatures over the continental surfaces and warmer temperatures

Table 1

Percent Cloud versus Height Scatter Diagrams
Slopes (S) and Intercepts on the Height Axis (I) of Least Squares Fit Lines

Constant-Pressure Surface		Cloud top at				Range of Intercept on Height Axis (Geopotential meters)
		850	700	500	400	
		(mb)				
500	S	0.011	-0.361	-0.476	-0.386	
	I	5877	5888	5889	5888	12
400	S	0.029	-0.490	-0.740	-0.708	
	I	7589	7606	7611	7611	22
300	S	-0.112	-0.735	-1.071	-1.191	
	I	9689	9708	9715	9717	28
250	S	-0.195	-0.835	-1.253	-1.492	
	I	10952	10970	10980	10983	31
200	S	-0.303	-0.965	-1.410	-1.798	
	I	12422	12437	12446	12451	29
150	S	-0.407	-1.115	-1.520	-2.079	
	I	14228	14242	14247	14253	25
100	S	-0.417	-1.134	-1.513	-2.122	
	I	16660	16674	16675	16679	19

over the Atlantic Ocean. For the most part, the three cloud cases analyzed (clear air soundings, cloudy soundings, and all June-July soundings) agreed well, and their contour patterns were consistent throughout the upper troposphere. It was found that the clear air case displayed temperatures about one degree warmer over the oceans than the all-soundings mean.

Constant-pressure height analyses for the same three-cloud amount cases showed the same consistencies in their contour patterns. Lower height values remained over the continents while higher regions persisted over the ocean. As the cloud amount of the soundings increased, the areas of greater heights became smaller while the lower height regions became more dominant, suggesting that cloud amount has profound influence on the heights of a constant-pressure surface.

To reinforce this conclusion, scatter diagrams of height versus percent cloud in the satellite field of view were investigated for

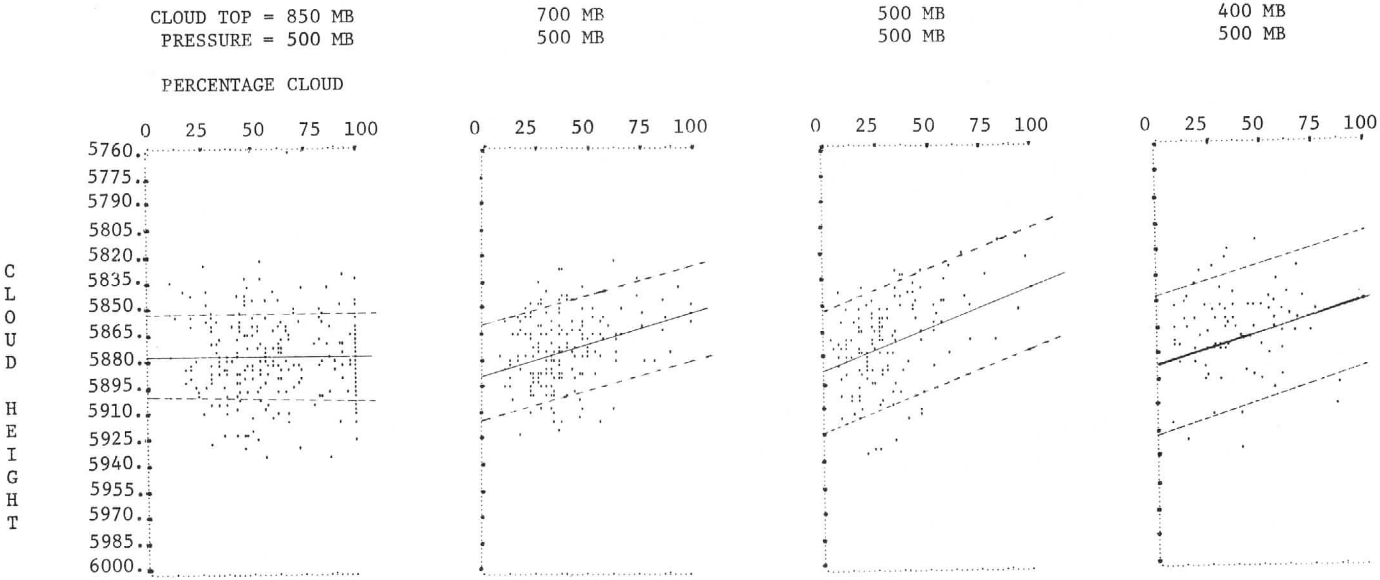

Figure 8. Height (geopotential meters) vs. Percentage Cloud, 500 mb Surface

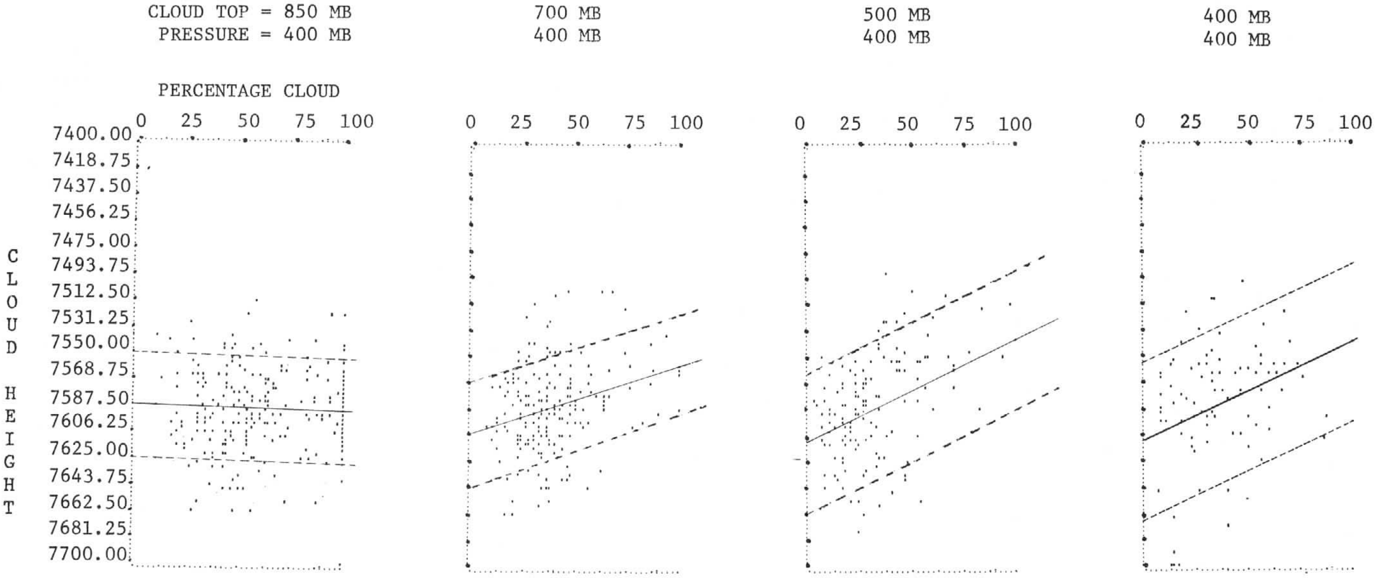

Figure 9. Same as in Figure 8 but for 400 mb Surface

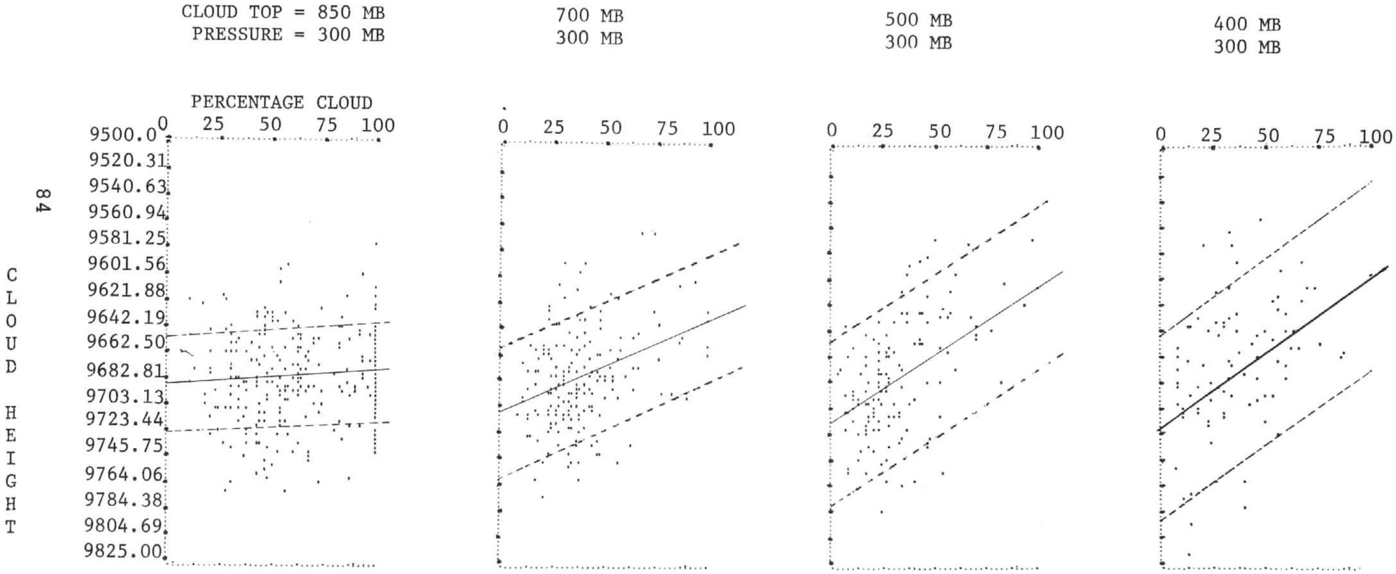

Figure 10. Same as in Figure 8 but for 300 mb Surface

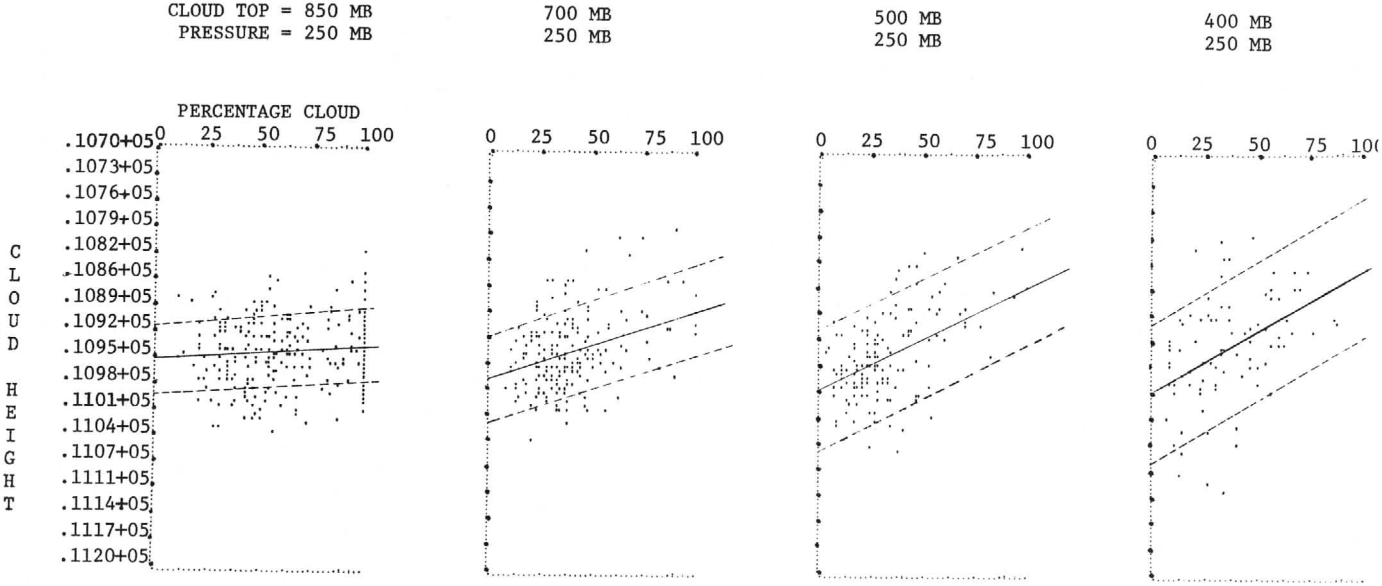

Figure 11. Same as in Figure 8 but for 250 mb (+05 in the ordinate means × 10^5)

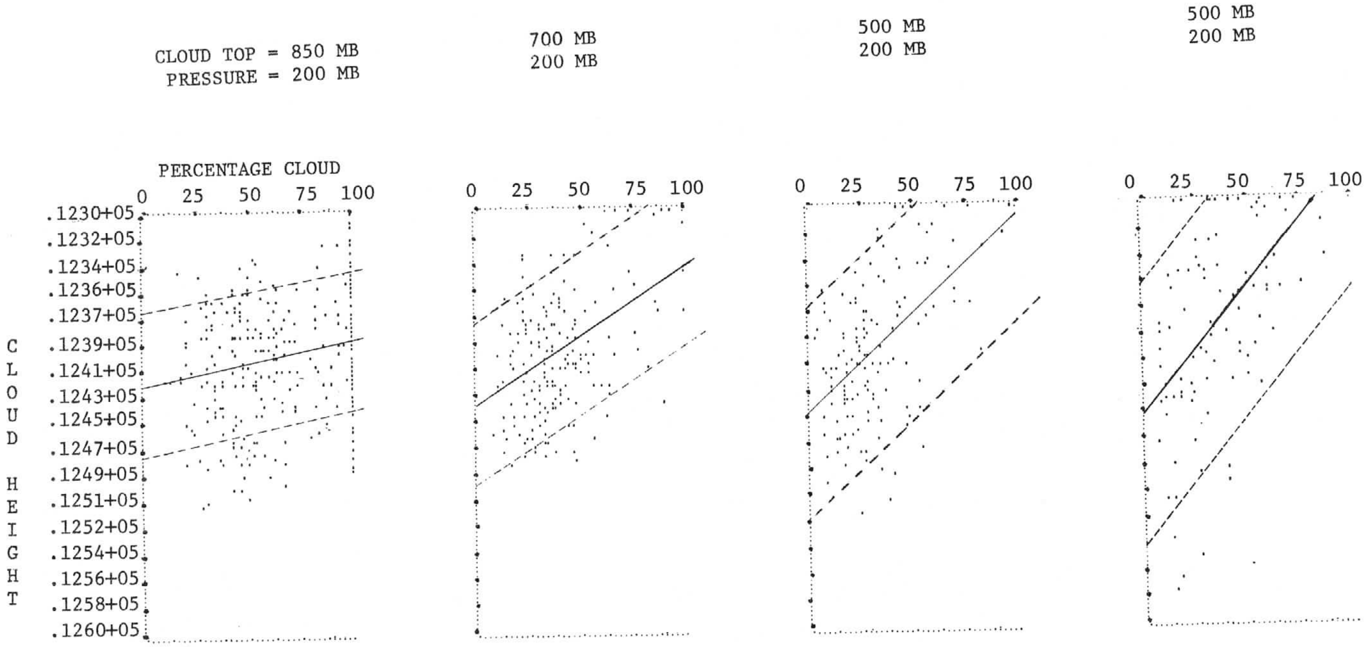

Figure 12. Same as in Figure 11 but for 200 mb Surface

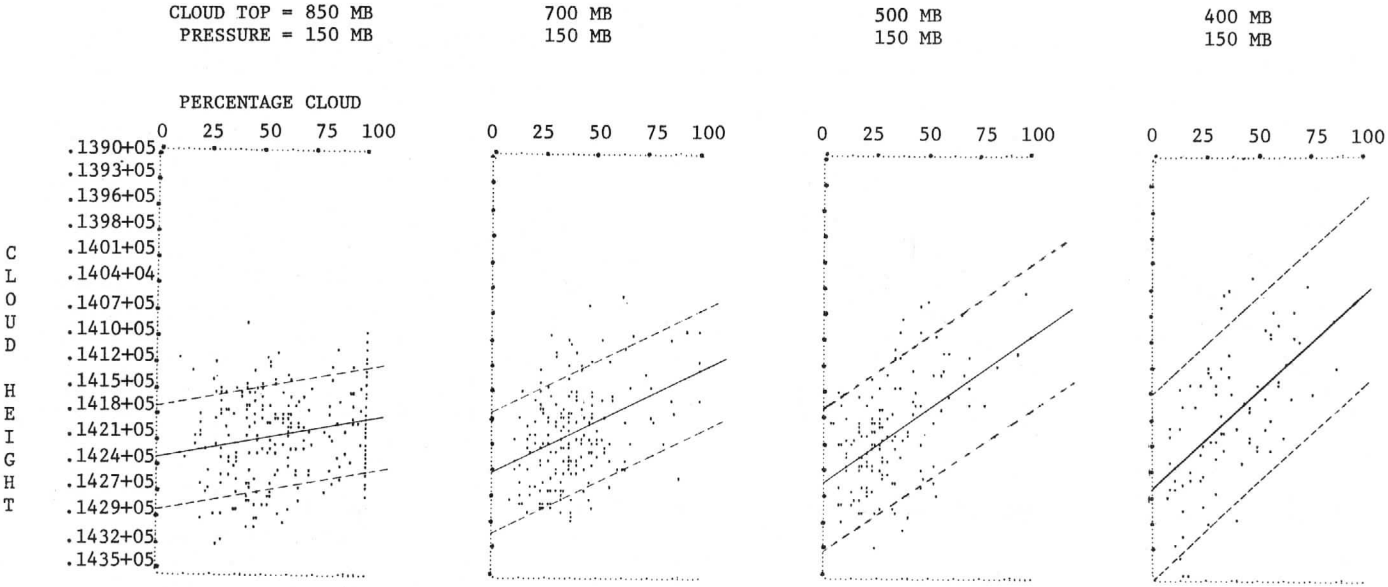

Figure 13. Same as in Figure 11 but for 150 mb Surface

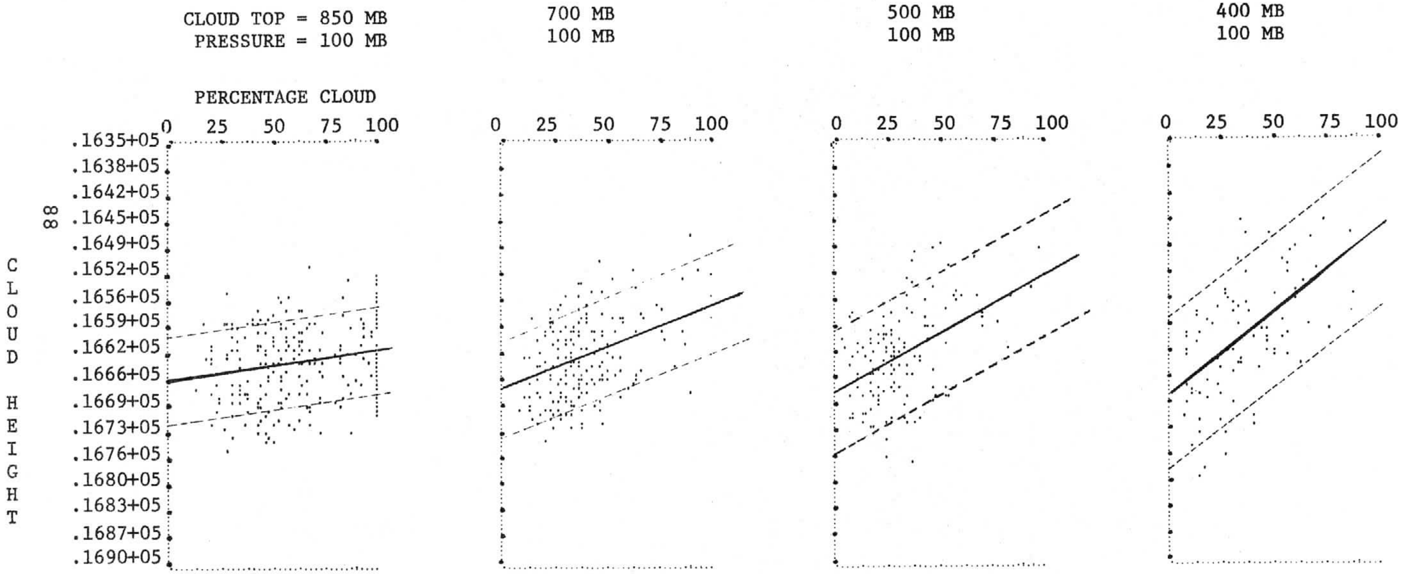

Figure 14. Same as in Figure 11 but for 100 mb Surface

separate cloud top levels. By examining the change in slope of the line of least squares fit, it was apparent that increases in percent cloud cover and greater cloud thickness caused consequential decreases in the heights of all the constant-pressure surfaces, above and below the cloud top level.

We may tentatively conclude from this investigation that, despite some limitations, the SIRS soundings are exceedingly useful for constructing upper tropospheric climatological patterns of temperature and constant-pressure height fields, especially in the data-sparse tropical oceans.

ACKNOWLEDGMENT

The authors wish to thank Dr. W. L. Smith of NESS for supplying the NIMBUS-III SIRS data, and D. W. Martin of the Space Science and Engineering Center and Mr. Hans Rosendal, State Climatologist at the University of Wisconsin, for critically reviewing the manuscript. The research reported in this paper was supported by NOAA under Grant E-230-68-(G).

References

Hayden, C. M., 1971: "Nimbus 3 SIRS Pressure-height Profiles as Compared to Radiosondes," Mon. Wea. Rev., 99, 9, 659-665.

Nimbus-III User's Guide, Ed. R. R. Sabatini; prepared by the NIMBUS project. Goddard Space Flight Center, NASA.

Riehl, H., 1945: "Waves in the Easterlies and the Polar Front in the Tropics," Dept. of Meteorology, The University of Chicago, Misc. Rept. 17, 79 pp.

Sikdar, D. N. and V. E. Suomi, 1971: "Time Variation of Tropical Energetics as Viewed from a Geostationary Altitude," J. Atmos. Sci., 28, 2, 170-180.

Smith, W. L., et al., 1970: "A Regression Method for Obtaining Real-Time Temperature and Geopotential Height Profiles from Satellite Spectrometer Measurements and Its Application to Nimbus 3 SIRS Observations," Mon. Wea. Rev., 98, 8, 582-603.

Smith, W. L. and H. M. Woolf, 1969: "On the Usefulness of Satellite Derived Temperature Profiles in Tropical Analysis," Sixth Technical Conference on Hurricanes, Dec. 2-4, Miami, Florida.

Yanai, et al., 1968: "Power Spectra of Large-scale Disturbances over the Tropical Pacific," J. Meteor. Soc. Japan, 46, 801-816.

SOME EMPIRICAL FINDINGS ON THE RELEASE OF LATENT HEAT IN TROPICAL CLOUD CLUSTERS OF THE PACIFIC

D. N. Sikdar

ABSTRACT

ATS-I time lapse cloud photos are here employed for deriving information on cloud cluster growth rate in the central Pacific using Sikdar's technique and a regression equation relating growth rate to cirrus shield area. The growth rate is found to increase consistently with cirrus shield size, and the related latent heat fluxes range between 10^{12} and 10^{14} cal/sec in a mean thermodynamic environment.

1. Introduction

A large convective cloud, according to thermal theory, is an assemblage of individual buoyant parcels intermittently rising as cloud towers. Successive towers in a cumulonimbus cloud penetrate into high troposphere leading to a persistent glaciated residue spreading out into a mushroom anvil. This visual manifestation of deep tropical cloud evolution has been noted on time lapse Applications Technology Satellite-I (ATS-I) and ATS-III cloud photos (Sikdar 1969). The size of these glaciated surfaces evidently depends on the lifetime and intensity of convection beneath the cluster. The lifetimes of these clusters usually range between one and three days, occasionally reaching five days in the Pacific (Martin and Karst 1969).

These cloud cluster-scale disturbances embedded in a wave scale are the central zones in which most of the latent heat is released to the atmosphere; they appear to have direct interaction with the large-scale tropical circulation. In view of its important role in the general circulation, it will be interesting to examine the relationship existing between the release of latent heat in a tropical cluster and some parameters such as cloud size, brightness, depth, etc., as visually evident on the satellite photos.

Ground-based observations of cumulus convection show a consistent increase in the growth of convection as a function of cloud size (Brown 1967). Sikdar and Suomi (1972) also reported such linear relationship from the ATS satellite photos and showed the feasibility of estimating latent heat release—the primary energy source in a convective circulation. The purpose of this paper is:

1. To assemble such ATS observations of cloud size made in summer 1970 in the central Pacific, and

2. To develop a power function relating cirrus shield size to their possible latent heat release.

Such information should be useful to circulations in the data-sparse regions of the tropical oceans.

2. Background

In the simple three-layer convection scheme used by Sikdar and Suomi (1971, 1972), the expansion of cumulonimbus cloud tops aloft in the form of an anvil was taken to be a direct result of convergence at the subcloud layer, vertical motion in the undiluted core, and subsequent divergence at the cloud top. The cloud divergence is analogous to the horizontal spread of smoke particles in the atmosphere when the rising plume strikes a stable layer. Implicit in such a convective circulation is the question of what proportion of the upward convected air ends in the outflow layer. It is well known that a large amount of air is involved in the downdraft—about 60% of the updraft—which, according to Newton (1966), comes from the midtropospheric layers. Fankhauser (1968) also provided some observational support to the midtropospheric origin of the cold downdraft in a deep convective circulation. From midlatitude thunderstorm data, Newton (1966) concluded that "essentially all the air originating in the updraft remains in the upper troposphere, spreading out mainly in the anvil plume downshear, but appreciably also in the upshear side." In this paper we have attempted to estimate the rate at which this air originating at low levels spreads out near the tropopause in the anvil plume atop a cloud cluster.

In a cloud cluster-scale convection regime, there may be embedded one or more active convective elements at a time. As has been pointed out by Byers and Braham (1949), while the formation of precipitation within the updraft eventually results in the collapse of an individual cell, new cell formation perpetuates the lifetime of the storm complex. This mode of evolution leads to quasi-periodic or periodic fluctuations in the anvil growth, as has been noted by Sikdar (1969) and Sikdar et al. (1970).

3. Method

Sikdar and Suomi (1971) have demonstrated that anvil growth measurement by eye atop an active cloud cluster in the tropics is a reasonable technique for probing into the storm circulation parameters like cloud divergence aloft, mass flux and volume flux in time domain from enlarged time-lapse ATS photographs. Although some subjectivity is involved in isolating the cirrus shield boundary from the hard copy pictures, our experience is that even such measurements are meaningful for statistical information on the dynamics of large-scale cloud systems in the tropics (Sikdar et al. 1972). In this paper we have used hard copy cloud pictures as our data source, the main reason being that they are inexpensive and readily available.

Approximately six ATS-I photographs for each day of summer 1970 were selected; each set of six had been taken at 23-minute intervals around local noon at the satellite subpoint (150°W). Cirrus shield changes for various cloud sizes were then analyzed from successive cloud photos in 10° latitude by 20° longitude zones in the Central Pacific (Figure 1).

The assumptions involved in developing a regression equation relating cirrus shield size and latent heat release are that:

(a) In an active deep tropical convection, air converging at the cloud base rises in undiluted wet towers to the upper troposphere. Mass is conserved in the rising volume.

(b) The amount of moisture flowing into the tower from subcloud layer (20 g/kg) is all condensed in-cloud and the equivalent potential temperature at the LCL is constant.

(c) The layer of outflow atop a deep convection is approximately 1.0 kilometer thick (Ludlum 1966) with its base at around 200 mb.

The power functions employed to derive growth rate and latent energy release are:

$$\frac{dA_c}{dt} = aA_c^x \qquad (1)$$

$$E_c = bA_c^x \qquad (2)$$

where A_c is the cirrus shield area (cm^2), E_c is latent energy flux in the system (cal/sec), t is time (secs), and a, b and x are parameters to be determined from observation.

4. Mean Features of Cloud Cluster Activity in the Pacific during Summer 1970

Figure 1a presents mean percent cover of bright cloud clusters in the study area bounded by 170°E - 110°W, 20°N - 20°S during summer 1970. Only those clusters were chosen whose brightness corresponded approximately to the uppermost 25-30% of the ATS brightness range and whose dimensions were larger than 10^2km^2. A significant geographical difference in the amount of bright cloud is clearly evident in the figure. The mean cloud amounts range from less than 1% to more than 15% coverage with two apparent maxima located in the 7°-20°N in the eastern sector and 0°-10°N in the western sector of the ITCZ. In the southern hemisphere a similar structure is missing due to a pronounced "dry zone" in the eastern portion of the domain which terminated at the western end at around 150°W. Although no significant maximum is clearly seen in the western southern hemisphere of the domain, mean cloudiness ranged between 5% to 9% with a broad cloud band extending from the equator southeastward crossing 20°S at around 170°W.

The transient features of cloud cluster activity are brought out clearly in the root-mean-square amounts shown in Figure 1b. An apparent similarity in the patterns shown in Figures 1a and 1b suggests that the resulting mean cloud amounts are due to moving cloud disturbances. In the diagram one finds a persistent regime both in the eastern as well as in the western Pacific on the ITCZ (lightly stippled areas), while in the dry zone cloudiness appears to be related mainly to transient disturbances (heavily shaded areas).

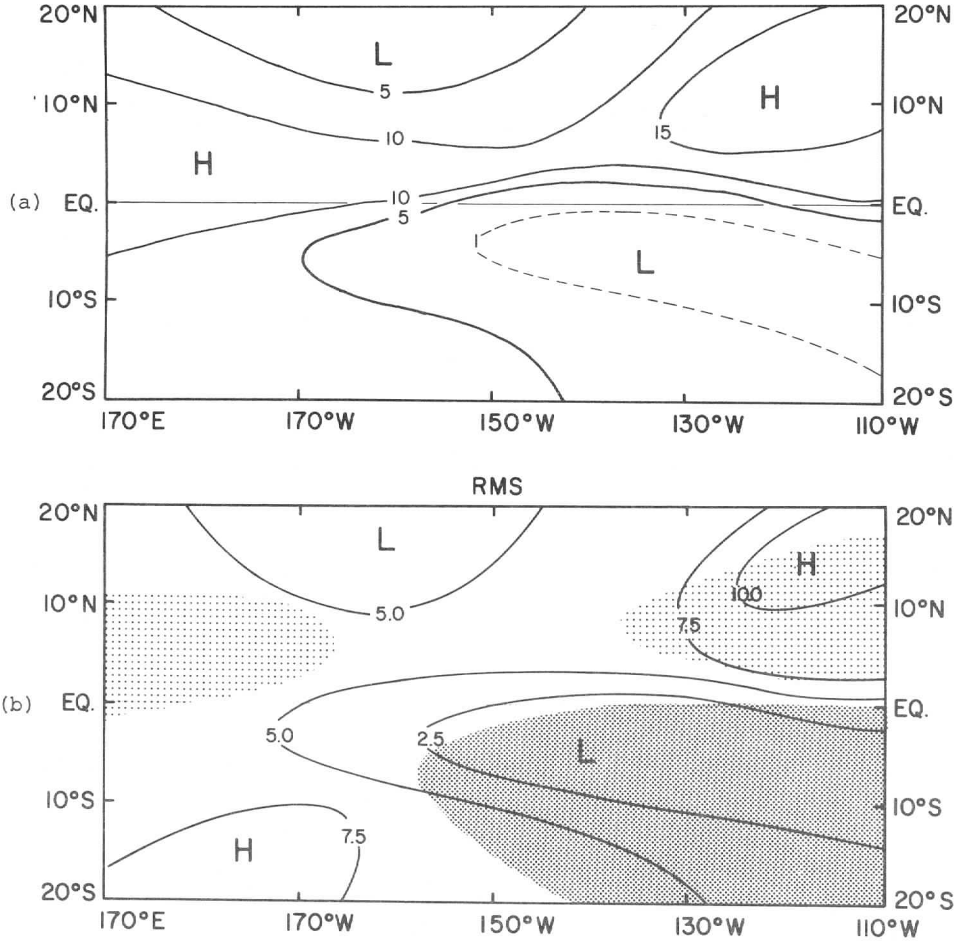

Figure 1(a). Mean percent cover of bright cloud clusters in the study area (July-September, 1970).

1(b). Root-mean-square cloud amount. Lightly stippled areas indicate persistent regime while heavily shaded areas represent transient disturbance regime.

In Figure 2 the mean cloud cluster growth rate in the domain is shown. As expected, the regions of maximum growth rates are at the locations of persistent and highest mean percent bright cover. Viewing a wide range of variations in convection intensity as a function of both latitude and longitude, the data have been partitioned into four latitude bands and regression analyses were performed. The results are discussed in the next section.

5. Results

Figure 3 is a scatter plot of cirrus shield expansion rate in growing clouds vs. cloud sizes in the latitude belt 0-10°N for the study period. This diagram reflects mainly the cloud cluster activity in the ITCZ and suggests that the growth-rate varies as a simple power function of cloud size. The parameters determined from the regression line are: $a = 52.4(\mathrm{cm})^{0.7}\ \mathrm{sec}^{-1}$, and $x = 0.62$. Substituting them in Eq. (1) results in:

$$\frac{dA_c}{dt} = 52.4\ A_c^{0.62}\ . \qquad (3)$$

Table 1 gives the parameters such as a and x, correlation coefficients, and variances for other latitude bands as well, while the regression lines thus obtained are shown in Figure 4. Interestingly,

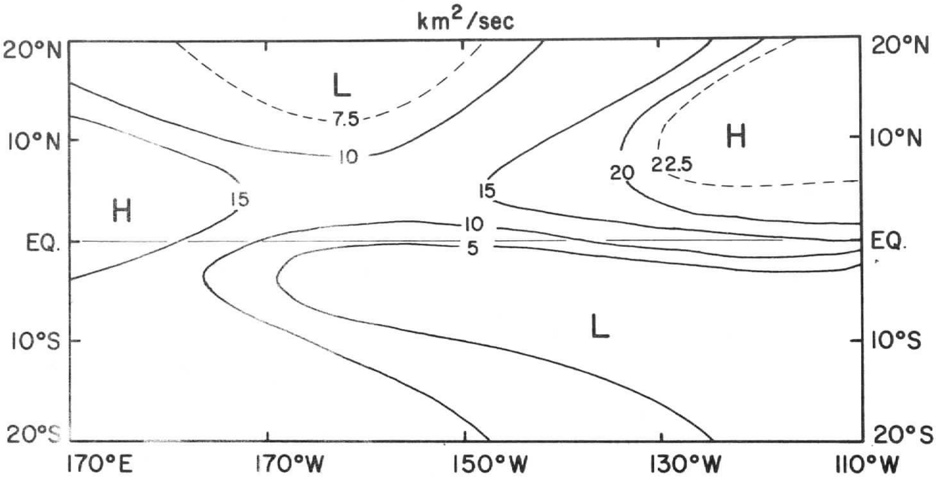

Figure 2. Mean cloud growth rate in the study domain and period.

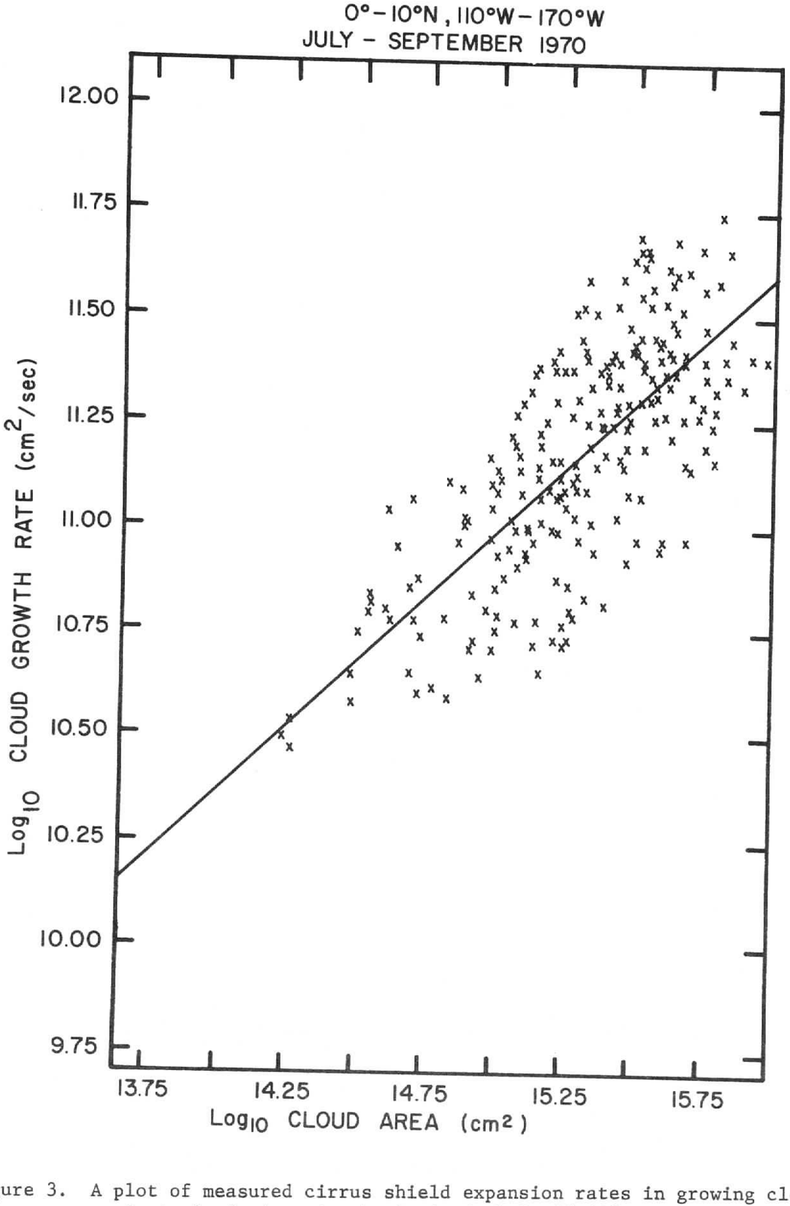

Figure 3. A plot of measured cirrus shield expansion rates in growing clouds against cloud sizes in the latitude belt 0°-10°N for the study period.

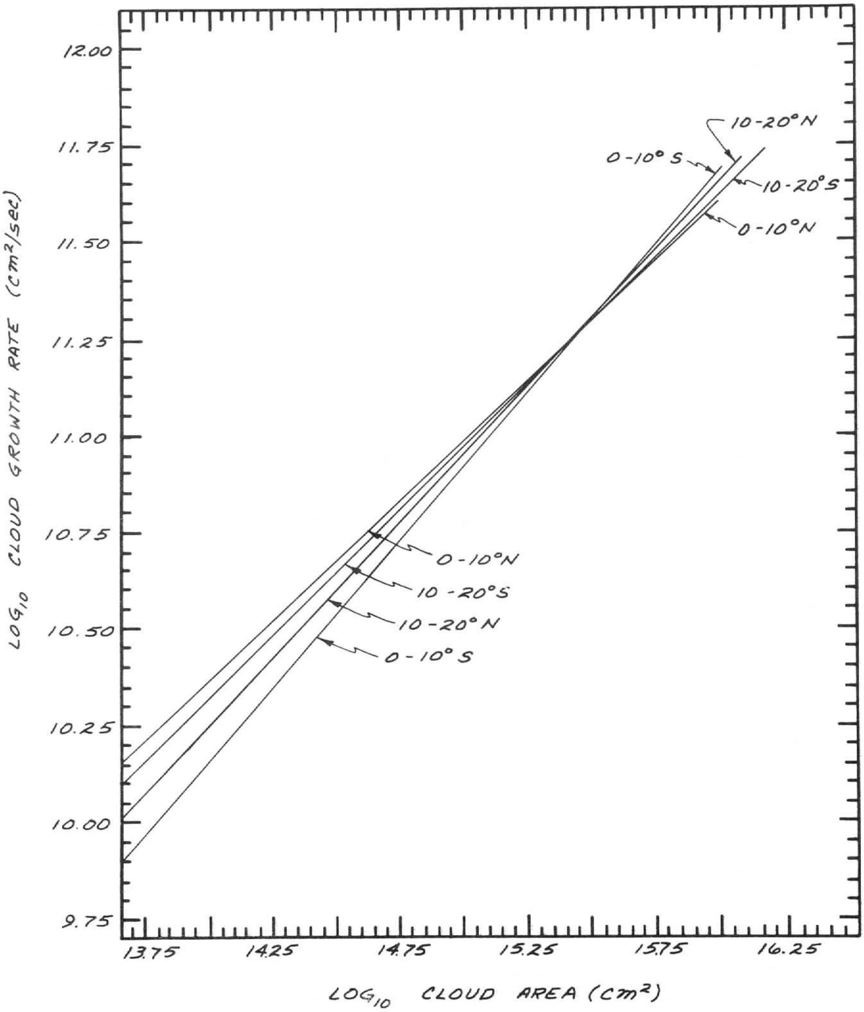

Figure 4. Regression lines for cloud growth rates vs. cloud sizes for four latitude belts.

the slopes are slightly different, probably because of the varying range of convection activities and of numbers sampled in different latitude bands. Nevertheless, the magnitudes for cluster growth rates hardly show much variation for clusters of size greater than $10^2 km^2$ in the data presented. An important feature of this diagram, however, is the proximity of the regression lines pertaining to the latitude bands 0°-10°N and 10°-20°S.

Although various slopes have been presented here to show the range of convection activity in different latitude bands in the Pacific, for an order of magnitude estimate one might as well use the mean regression line for 10-20°N band. This will involve an error in cloud growth rate of less than ± 1% for latitude bands 0-10°N, and 0°-10°S for cloud size $10^{14}\ \bar{c}m^2$ and even less for larger clouds.

It should be re-emphasized here that in this computation scheme only the positive values of the first time derivative have been considered. This condition includes only the clouds in their active stages of growth and avoids ambiguity likely to be introduced by dissipating convection.

In regard to the cloud cluster energetics (primarily latent heat released), Sikdar and Suomi (1971) assumed that there was a direct coupling between the subcloud layer and the outflow layer through undiluted wet towers, and also that the latent heat released during ascent is conserved in the rising volume itself. Based on this concept, we have developed regression equations for the cloud cluster energetics related to cloud size shown in Figure 5. The parameter b in Eq. (2) is given in Table 2. The equation used to derive these energetics is:

$$E_c = L \cdot \Delta W \frac{dM_L}{dt} \text{ cal/sec} \qquad (4)$$

where $L = 597$ cal/gm at 0°C; ΔW = difference in mixing ratio between the base and cloud top; dM_L/dt = mass influx at the cloud base determined by following Sikdar and Suomi (1971).

6. Concluding Remarks

The data in Figure 5 clearly show that the latent heat release varies significantly from one cloud cluster to another in the tropical Pacific and the variation ranges from about 10^{12} to 10^{14} cal/sec depending on the cloud size. Using thunderstorm project data, Braham (1952) investigated the energy budget of typical Ohio thunderstorms to be of the order of 10^{11} cal/sec. The tropical cloud clusters investigated in this paper are large enough to cover more than one thunderstorm simultaneously, and what we have measured is the total contribution during the growth period. Sikdar and Suomi (1972) have shown that the energy released in a cloud cluster scale convection may at times be even two orders higher than

Table 1

Parameters Computed from Regression

Analyses of A_c vs. $\frac{dA_c}{dt}$

Latitude Band	No. of Data Points	a	x	Variance*	r	Empirical Equation
10-20°N	322	1.74 $cm^{0.58}/sec$	0.71	.083	0.99	$\frac{dA_c}{dt} = 1.74A_c^{0.75}$
0-10°N	257	52.4 $cm^{0.76}/sec$	0.62	.072	0.99	$= 52.4A_c^{0.62}$
0-10°S	187	0.17 $cm^{0.44}/sec$	0.78	.073	0.99	$= 0.17A_c^{0.78}$
10-20°S	241	16.6 $cm^{0.7}/sec$	0.65	.065	0.99	$= 16.6A^{0.64}$

r = correlation coefficient

$^*\log_{10}$

Table 2

Empirical Equations Relating Cloud Size and Possible Latent Heat Release (Eq. (2))

Latitude Band	b	Empirical Equations
10-20°N	478.7 $cal/cm^{1.42}$ sec	$E_c = 478.7A_c^{0.71}$
0-10°N	14355.0 $cal/cm^{1.24}$ sec	" $= 14355A_c^{0.62}$
0-10°S	46.8 $cal/cm^{1.56}$ sec	" $= 46.8A_c^{0.78}$
10-20°S	4571.0 $cal/cm^{1.30}$ sec	" $= 4571.0A_c^{0.65}$

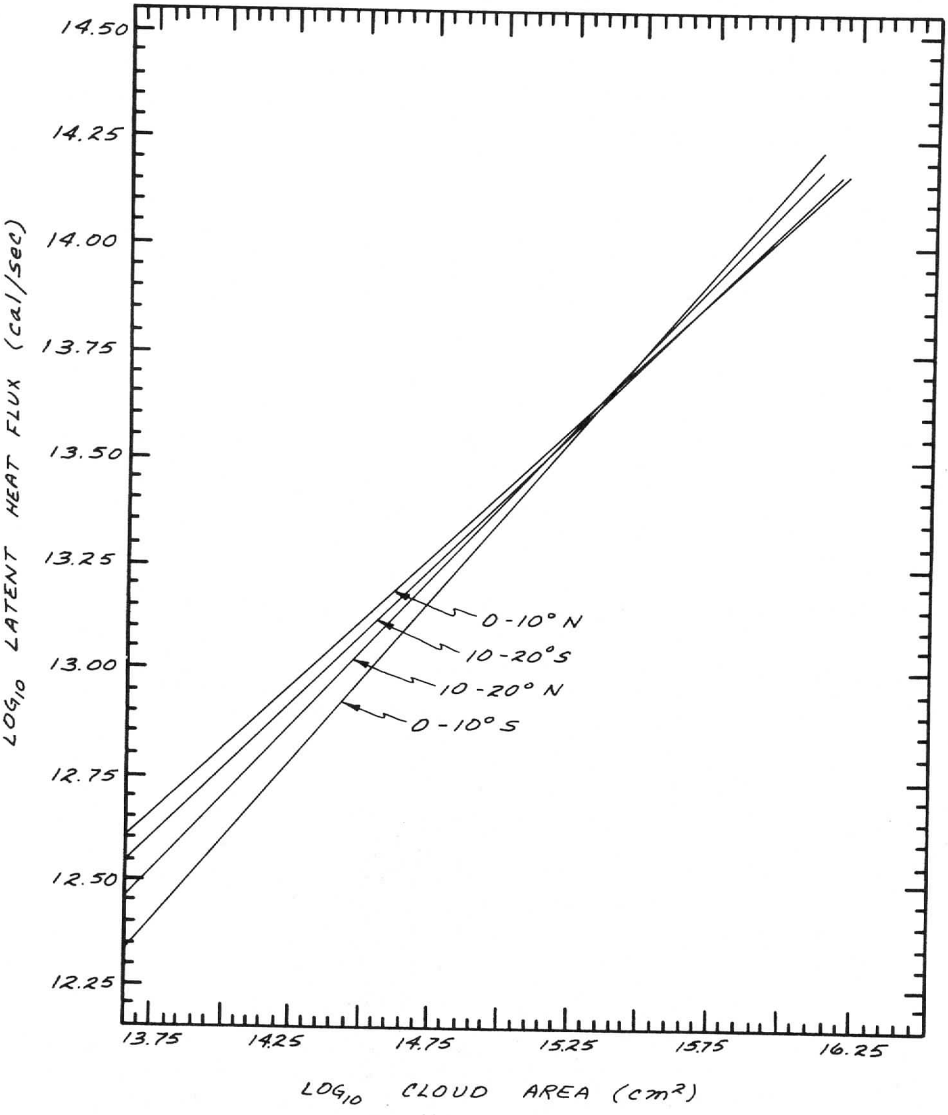

Figure 5. Cloud cluster-scale latent heat release related to cloud sizes.

in an ordinary Ohio thunderstorm. In light of Brown's composited picture on thunderstorm energetics (1967), the magnitudes of heat release quoted here appear very realistic.

Dissipating cirrus shields have been ignored in this study, even though they might have a role to play on the energy balance in the tropical upper troposphere. The magnitudes of these effects are under further study.

ACKNOWLEDGMENT

The author is grateful to Professor V. E. Suomi for reviewing this report and offering helpful suggestions. The research reported in this paper was supported by NOAA under grant E-230-68-(g).

References

Byers, H. and R. R. Braham, Jr., 1949: The Thunderstorm, Washington, Govt. Printing Office, 287 pp.

Braham, R. R., Jr., 1952: "The Water and Energy Budgets of the Thunderstorm and their Relation to Thunderstorm Development," J. Meteor., 9, 227-242.

Brown, R. A., 1967: "Mass and Available Energy in Growing Convective Clouds," J. Atmos. Sci., 24, 308-311.

Fankhauser, J. C., 1968: "Thunderstorm-environment Interaction Revealed by Chaff Trajectories in the Mid-troposphere," Nat. Severe Storm Lab. Tech. Mem. ERLTM-NSSL 39, 14 pp.

Ludlum, F. H., 1966: "Cumulus and Cumulonimbus Convection," Tellus 4, 18, 687-698.

Martin, D. W. and O. Karst, 1969: "A Census of Cloud Systems Over the Tropical Pacific," Studies in Atmospheric Energetics Based on Aerospace Probings, Annual Report 1968, Space Science and Engineering Center, University of Wisconsin, 37-50.

Newton, C., 1966: "Circulation in Large Sheared Cumulonimbus," Tellus 4, 687, 699-712.

Riehl, H., 1954: Tropical Meteorology, New York, McGraw-Hill.

Sikdar, D. N., 1969: "Convective Heat Transport over the Tropical Mid-Pacific as Estimated from a Geosynchronous Satellite Altitude," Ph.D. thesis, Dept. of Meteorology, University of Wisconsin, Madison.

---

[*] Global Atmospheric Research Program.

Sikdar, D. N., V. E. Suomi and C. E. Anderson, 1970: "Convective Transport of Mass and Energy in Severe Storms over the United States—An Estimate from a Geostationary Altitude," Tellus, 22, 521-532.

Sikdar, D. N. and V. E. Suomi, 1971: "Time Variation of Tropical Energetics as Viewed from a Geostationary Altitude," J. Atmos. Sci., 28, 170-180.

Sikdar, D. N., J. A. Young and V. E. Suomi, 1972: "Time-spectral Characteristics of Large-scale Cloud Systems in the Tropical Pacific," J. Atmos. Sci., 29, 229-239.

Sikdar, D. N. and V. E. Suomi, 1972: "On the Remote Sensing of Mesoscale Tropical Convection Intensity from a Geostationary Satellite," J. Appl. Meteor., 11, 37-43.

A LINEAR MODEL OF BOUNDARY LAYER AIRFLOW DURING THE ST. PATRICK'S DAY STORM OF 1965

Richard J. Naistat and John A. Young

ABSTRACT:

A time-dependent, one-dimensional numerical model of the boundary layer at individual stations is solved by a finite difference technique for the St. Patrick's Day storm of 1965. Using only surface pressure and temperature gradients at three-hour intervals as input, the model predicts the boundary layer wind profile at each of the 225 grid points covering the central and eastern United States. Predicted winds are used to evaluate vertical motion, vorticity, trajectories, and the acceleration due to the isallobaric wind. The output is compared to a simple steady-state solution and to observed data.

The solution of the equations of motion with the local accelerations included and inertial terms neglected contains a damping effect in order to control the inertial-like oscillations which have previously complicated the physical interpretation of similar models. With the damping included, the model successfully predicts the location of the low-level jet core, the vertical motion distribution, and, qualitatively, the orientation of the acceleration associated with the isallobaric wind in the boundary layer. The model-forecast ascent is well correlated with the observed precipitation rate.

1. Introduction

From a forecaster's point of view, the prediction of winds at any level is a difficult problem. Frequently in the middle latitudes the geostrophic approximation is used in the free atmosphere and the Ekman Spiral in the boundary layer. However, during storm situations, i.e., nonsteady-state conditions, these simplifications fail. Fortunately, sophisticated numerical models such as the six-level primitive equation (PE) model (Shuman and Hovermale, 1968) provide useful forecasts in the free atmosphere. However, the six-level PE model includes only a crude representation of frictional effects and is further handicapped by its coarse grid structure. A relatively simple scheme for the prediction of low-level winds seems desirable. Correctly forecast winds in the boundary layer are important, not only because much of human activity takes place there, but because the vertical motion at the top of the boundary layer is related to the convergence in this layer as emphasized by Charney and Eliassen (1949). The role of this vertical motion as a contributing factor in the formation of low-level clouds and precipitation is well known. In recent years, boundary winds have gained increased importance because of their application to air pollution potential forecasting (Gross, 1970).

Surprisingly little has been done in modelling boundary layer airflow during changing synoptic conditions. On the other hand, many steady-state models have been developed. The classic steady-state solutions which produce wind spirals were due to Ekman (1905) and Taylor (1916). More realistic steady-state models, again for a barotropic atmosphere, have been formulated by Lettau (1962) and Blackadar (1962). Baroclinicity has been included in steady-state models by Blackadar (1965), Mahrt and Schwerdtfeger (1970), and Young (1970).

In a more general sense, models of the time-dependent boundary layer that involve temporal changes of the eddy viscosity but hold the synoptic conditions constant have been devised by Ooyama (1957) and Estoque (1963).

Returning to the free atmosphere, we find that the classic idealized solution for the variation of the wind due to a changing pressure gradient force is that of the isallobaric wind due to Brunt and Douglas (1928). However, extension of this concept into the boundary layer (indeed, forecasters apply this on the surface weather map) has only recently been accomplished (Young, 1972).

Pandolfo and Brown (1967) were the first to allow for the variation in the pressure gradient force in the boundary layer. They found an analytic solution for a two-layer air-sea interaction model in which the pressure gradient in one layer was periodic and in the other layer was zero. Furthermore, the fluid was assumed barotropic. Their results were difficult to interpret in a large-scale synoptic situation because of the presence of a quasipermanent inertial oscillation.

In an extension of this idea, Businger and Ching (1968) have derived an analytic solution for boundary layer winds in which the direction of the pressure gradient force varied in time. Again, the atmosphere was assumed barotropic. Furthermore, their one-layer model used a "no-slip" condition at the lower boundary. Their resulting solution consisted of an Ekman-like component and a damped inertial oscillation. They concluded, however, that the inertial oscillations should have been neglected since they were rather artificial.

The most recent attempt at extending the concept of the isallobaric wind into the boundary layer has been given by Young (1972). His analytic solution has the advantage that inertial oscillations are automatically filtered out; yet deviations from Ekman flow are included. Again, using a linear barotropic model, he finds that besides the Ekman wind spiral there is a spiral associated with the isallobaric wind component in the boundary layer. Essentially the isallobaric wind in this layer does not blow 90° across the isallobars toward lower values as found by Brunt and Douglas (1928) in the free atmosphere, but blows somewhat to the left of this direction. This may be likened to the real wind blowing to the left of the geostrophic wind in the boundary layer and veering with height in a manner somewhat like the Ekman spiral.

In a realistic synoptic storm situation, the requirement of a no-slip boundary condition and a barotropic atmosphere undergoing a periodic pressure gradient force cannot be expected to give reasonable results. In this paper, a numerical model is discussed which allows for temporally and spatially varying pressure and temperature gradients in the boundary layer. Furthermore, the no-slip requirement is replaced by the geophysical boundary condition used by Kuo (1971). As in the previous studies of Pandolfo and Brown (1967), Businger and Ching (1968), and Young (1972), the inertial terms in the equation of motion are neglected, the eddy exchange coefficient is constant in time and space, and horizontal stresses and molecular viscosity are ignored.

This model's largest departure from previous studies is the application of boundary layer theory to a real storm situation. Over the period from 16 March 1965 to 19 March 1965, a storm of major proportions (see, e.g., Ludlum, 1965; Green, 1965; or Ludlum, 1966) moved from Colorado to the Upper Great Lakes where as much as 21.4 inches of snow was deposited at Duluth, and a foot of snow was blown about by winds gusting to 70 mph over Iowa. Further south, tornadoes ravaged portions of the central Great Plains, Midwest, and South. In particular, this storm was characterized by its large area of influence, its strong isallobaric gradient, its dry tongue, and its low-level jet. Furthermore, the storm went through three distinct stages: intensification with little movement, movement with little intensification, and the occluded or decaying stage.

Essentially, in the one-dimensional model presented here, the linearized horizontal equations of motion are numerically integrated in height and time. Other than the initialization, the only inputs into the model are the surface pressure and temperature gradients from three-hourly maps provided by the National Meteorological Center. (Operationally, the analog of this procedure would be a perfect surface forecast of temperature and pressure gradients.) Thus, the atmosphere was considered to be in the process of adjusting to the changing pressure pattern, and the model predicts the boundary layer airflow that accompanied these changes.

In Section 2, the mathematical formulation of the model and its finite difference solution are discussed. In Section 3, several numerical experiments are performed at the grid point corresponding to Columbia, Missouri. Especially important in Section 3 is the elimination of the inertial oscillations which are unobservable on the synoptic scale. These oscillations distorted the results of Pandolfo and Brown (1967) and Businger and Ching (1968). Without further adjustment of parameters, the one-dimensional model is run at each of 225 grid points. In Section 4, the kinematically computed vertical motion field that is produced from the model forecast divergence is compared to observed cloudiness, weather and precipitation rates. Also, the vertical motion from the model is contrasted to that produced by a simple steady-state analytic solution. Finally, in Section 5, the model-predicted winds are computed to both a steady-state solution and, more important, to the observed winds. The location and intensity of the low-level jet is examined. Trajectories are shown for selected air parcels and the vorticity field is compared to that of vertical motion.

2. Governing Equations

Data

The input into the model consisted of surface pressure and temperature gradients evaluated by centered finite differences on a 15 × 15 grid that extended from 77°W to 105°W and from 31°N to 53°N. The area approximately extended from the Rocky Mountains to the Atlantic Coast and from southern Canada to the southern United States. The grid interval was 2° longitude in the east-west direction, and 1.67° latitude in the north-south direction. The surface gradients of temperature were taken from smoothed analyses of the isotherms by the authors and those of pressure by smoothed analyses at the isobars by the National Meteorological Center. While it was recognized that a horizontal temperature gradient generally exists over the Great Plains due to the sloping terrain, no correction for this effect was made. The neglect of this term results in the absence of a slope-induced thermal wind which depends upon the location and low-level stability (Holton, 1967; Mahrt and Schwerdtfeger, 1970).

Basic Equations

The horizontal equations of motion with the addition of a damping term, the inertial terms neglected, and using the Boussinesq approximation can be written as

$$\frac{\partial \vec{V}}{\partial t} = -f\vec{k} \times \vec{V} - \frac{1}{\rho_c}\vec{\nabla}p(z) + K\frac{\partial^2 \vec{V}}{\partial z^2} - \kappa(\vec{V} - \vec{V}_s) \qquad (2.1)$$

where $\vec{V}$ is the horizontal wind, f the Coriolis parameter, ρ_c a standard air density at the surface (equal to 1.3×10^{-3} gcm^{-3} in this paper), p the pressure, K the constant eddy diffusivity, $\vec{k}$ a unit vector in the vertical, κ an empirically determined damping coefficient, $\vec{\nabla}$ the two-dimensional del operator, and $\vec{V}_s$ the steady-state wind. The local acceleration in (2.1) results from an imbalance between the Coriolis force, the pressure gradient force, and the friction force and is gradually damped in time, depending on the value of κ.

The other equations used in this paper are the equation of state and the hydrostatic equation:

$$p = \rho RT \qquad (2.2)$$

and

$$\frac{\partial p}{\partial z} = -\rho g \qquad (2.3)$$

respectively. R is the gas constant for dry air, T the temperature, and g the acceleration of gravity.

In (2.1), pressure is a function of height. The height dependence is arrived at by substituting (2.2) into (2.3), integrating with respect to z (height), and then taking the gradient of both sides yielding

$$\frac{g}{R} z\nabla\left(\frac{1}{T}\right) = -\frac{\nabla p}{p_0} + \frac{\nabla p_0}{p_0} \qquad (2.4)$$

where $p(z)$ in the denominator of the right-hand side terms has been approximated by p_0, the surface pressure. Assuming that the temperature gradient is constant in height in the boundary layer, (2.4) can be rewritten approximately as

$$\nabla p(z) = \nabla p_0 + \frac{p_0 g z}{RT_c^2} (\nabla T_0) \qquad (2.5)$$

where T_c is a standard air temperature at the surface (equal to 280°K in this paper). By using (2.5), the height dependence of the pressure gradient is uniquely determined by the horizontal temperature gradient at the surface.

The fourth term on the right-hand side of (2.1) has been included as an ad-hoc means of controlling the inertial oscillations that result from ageostrophic motions above the layer of strong frictional influence— the lowest several hundred meters. Haltiner (1971) has theoretically discussed this phenomenon. In the real atmosphere, inertial oscillations do occur (Palmen and Newton, 1969), and are dispersed into the surrounding fluid as gravity-inertia waves (Cahn, 1945; Washington, 1964). However, in this one-dimensional model with pressure specified a priori, gravity waves are not present, so an alternative scheme was needed.

To alleviate the problem, the winds predicted in the model are damped toward a steady-state solution in such a way that the damping effect does not enter the steady-state balance of forces. In a barotropic atmosphere, this is tantamount to forcing the model solution toward the Ekman or Taylor wind spiral, for example. In the case of a baroclinic atmosphere, the output winds are damped toward a wind spiral modified by the thermal wind. No other theoretical reason is claimed for this process. The formulation of the damping scheme is described in Section 3.

The one-dimensional diffusion-like equation (2.1) is solved as a marching process at each of the 225 grid points. Each one-dimensional model has 16 levels with a vertical grid interval of 100 m. The model thus extends from the surface (which is really the base of the Ekman layer) to 1500 m above the top of the surface layer. The winds are computed at each time step, equal to 15 minutes, by the procedure to be later described. Divergence is then computed at each level over the 225 point grid. The results to be presented in map form in this paper are for the interior 13 × 13 points since differential quantities could not be computed at the boundaries.

Initial and Boundary Conditions

Equation (2.1) is the diffusion equation modified by a source term consisting of the pressure gradient and Coriolis force terms and the damping term. Therefore, both initial and boundary conditions must be prescribed. The initial condition for the barotropic atmosphere is the Taylor wind spiral, and for the baroclinic atmosphere it is the Taylor wind plus the thermal wind. Such an initialization appeared realistic since the model began running when the atmosphere was quiescent over most of the 225 point grid.

The simplest lower boundary condition for a boundary layer model is "no-slip" at the base. Taylor (1915) has shown that a more realistic assumption for the lower boundary is that the shear of the wind at the bottom of the Ekman layer be parallel to the wind itself. In the model a more general boundary condition is used:

$$\vec{V} = A \frac{\partial \vec{V}}{\partial z} , \qquad (2.5)$$

which is called the geophysical boundary condition by Kuo (1971), and is derived by equating two expressions for stress at the interface between the surface and planetary boundary layers (see, e.g., Eliassen and Kleinschmidt, 1957), $\vec{\tau}$:

$$C_D|\vec{V}|\vec{V} = \frac{\vec{\tau}}{\rho} = K \frac{\partial \vec{V}}{\partial z}$$

where C_D is the drag coefficient. Therefore

$$A = \frac{K}{C_D|\vec{V}|} ,$$

which was assumed constant by Kuo (1971). He interpreted A as the thickness of the sublayer (corresponding to the surface layer in this model), provided the wind profile was extended linearly rather than logarithmically down to the earth's surface. In this model, A is allowed to vary. Typical magnitudes of A in this model range from 200 m to 800 m.

At the top of the model, the usual assumption of geostrophic flow was thought too restrictive. Schlichting (1968) suggests that the top of the boundary layer be defined as that level at which the vertical wind shear becomes arbitrarily small. In this model, the top of the boundary layer is defined as that level at which there is no vertical wind shear for the barotropic case. In the baroclinic case, the condition is modified such that the vertical wind shear is due only to the thermal wind. Thus, in general, at the top of the model the wind shear corresponds to that of a geostrophic flow, viz:

$$\frac{\partial \vec{V}}{\partial z} = - \frac{g}{fT_c} (\vec{\nabla}T \times \vec{k})z \ . \qquad (2.6)$$

The Numerical Technique

The modified diffusion equation (2.1) can be solved by a method based upon the alternating Saul'ev finite differencing method. Larkin (1964) has shown that this quasi-implicit method is stable for the simple diffusion equation regardless of the time step used; its advantage is that it may be calculated explicitly, so that matrix inversions are not necessary. His approach is followed here.

Let ℓ and n identify points in the z,t (height, time) space. ℓ has integral values from 1 to 16 representing levels from the surface to 1500 m at 100 m intervals. The subscript n refers to known values, and $n + 1$ to the forecast values at the next time step. Difference quotients L and R are defined as:

$$L(u) = \frac{u_{\ell,n+1} - u_{\ell,n}}{\Delta t} - K \left[\frac{(u_{\ell+1,n} - u_{\ell,n}) - (u_{\ell,n+1} - u_{\ell-1,n+1})}{(\Delta z)^2}\right]$$

$$- \left[fv_{\ell,n} - \frac{1}{\rho_c} \left(\frac{\Delta p}{2\Delta x}\right)_{\ell,n}\right] - \kappa(u_{\ell,n} - u_{s\ell,n}) \qquad (2.8)$$

$$R(u) = \frac{u_{\ell,n+1} - u_{\ell,n}}{\Delta t} - K\left[\frac{(u_{\ell+1,n+1} - u_{\ell,n+1}) - (u_{\ell,n} - u_{\ell-1,n})}{(\Delta z)^2}\right]$$

$$- \left[fv_{\ell,n} - \frac{1}{\rho_c}\left(\frac{\Delta p}{2\Delta x}\right)_{\ell,n}\right] - \kappa(u_{\ell,n} - u_{s\ell,n}) \qquad (2.9)$$

respectively. A similar formulation exists for the v-component of (2.1). When (2.8) and (2.9) are set equal to zero (to satisfy (2.1)) and some rearrangement is done, the results are the explicit forms

$$u_{\ell,n+1} = \left[\frac{1}{\Delta t} + \frac{K}{(\Delta z)^2}\right]^{-1} \left[\frac{u_{\ell,n}}{\Delta t} + \frac{K}{(\Delta z)^2}(u_{\ell+1,n} - u_{\ell,n} + u_{\ell-1,n+1})\right.$$

$$\left. + fv_{\ell,n} - \frac{1}{\rho_c} \left(\frac{\Delta p}{2\Delta x} \right)_{\ell,n}\right] - \kappa(u_{\ell,n} - u_{s\ell,n}) \qquad (2.10)$$

and

$$u_{\ell,n+1} = \left[\frac{1}{\Delta t} + \frac{K}{(\Delta z)^2}\right]^{-1} \left[\frac{u_{\ell,n}}{\Delta t} + \frac{K}{(\Delta z)^2}(u_{\ell+1,n+1} - u_{\ell,n} + u_{\ell-1,n})\right.$$

$$\left. + fv_{\ell,n} - \frac{1}{\rho_c} \left(\frac{\Delta p}{2\Delta x}\right)_{\ell,n}\right] - \kappa(u_{\ell,n} - u_{s\ell,n}), \qquad (2.11)$$

for ℓ ranging from 2 to 15. In this paper, (2.10) is called "Saul'ev-up" because it is used in evaluating, for a given $n + 1$ time step, $\ell = 2,3,4,\ldots,15$. Likewise, (2.11) is called "Saul'ev-down" because, for a given $n + 1$ time step, it is used for $\ell = 15, 13, 12, \ldots, 2$. Saul'ev (1957) and Larkin (1964) recommend a combination of the above equations called the alternation direction explicit method in which (2.10) is used at odd time steps and (2.11) is used at even time steps. The alternation of (2.10) and (2.11) is believed to eliminate bias in the solution that may occur by always evaluating the vertical grid column in the same direction.

The lower boundary condition (2.5) can be rewritten as

$$\Gamma \vec{V}_{1,n} = \vec{V}_{2,n} \tag{2.12}$$

where

$$\Gamma = K^{-1} \Delta z \, C_D |\vec{V}_{1,n}| + 1 .$$

Substituting (2.12) into (2.10) and (2.11) yields

$$u_{1,n+1} = \left[\frac{\Gamma}{\Delta t} + (\Gamma-1)\frac{K}{(\Delta z)^2}\right]^{-1}\left[\frac{u_{2,n}}{\Delta t} + \frac{K}{(\Delta z)^2}(u_{3,n} - u_{2,n}) + f v_{2,n} - \frac{1}{\rho_c}\left(\frac{\Delta p}{2\Delta x}\right)_{2,n}\right] - \kappa(u_{1,n} - u_{s1,n}) \tag{2.13}$$

and

$$u_{1,n+1} = \Gamma^{-1} u_{2,n+1} \tag{2.14}$$

respectively.

Similarly, the upper boundary condition (2.6) is rewritten as

$$\frac{\vec{V}_{16} - \vec{V}_{15}}{\Delta z} = - \frac{g}{f T_c} (\vec{\nabla} T \times k)(15.5 \Delta z) . \tag{2.15}$$

Substituting (2.15) into (2.10) and (2.11) results in

$$u_{16,n+1} = - \frac{g}{f T_c} \left(\frac{\Delta T}{2\Delta y}\right)_{n+1} z + u_{15,n+1} \tag{2.16}$$

and

$$u_{16,n+1} = \Delta t \left[\frac{K}{(\Delta z)^2}(u_{14,n} - u_{15,n}) + \frac{u_{15,n}}{\Delta t} + f v_{15,n} - \frac{1}{\rho_c}\left(\frac{\Delta p}{2\Delta x}\right)_{15,n}\right] - \frac{g}{f T_c}\left(\frac{\Delta T}{2\Delta y}\right) z \left(1 + \frac{\Delta t}{(\Delta z)^2} K\right) - \kappa(u_{16,n} - u_{s16,n}) , \tag{2.17}$$

respectively.

As mentioned earlier, the Saul'ev method is stable regardless of the time step. However, near the top of the model the friction term in (2.1) becomes negligible and the solutions are no longer diffusive, but correspond to forced inertial oscillations subject to damping. To maintain stability in this area, Heun's method (called the double-approximation forward difference by Lorenz (1963)) is employed, which is reasonably stable for simple temporal oscillations as shown by Young (1968). Essentially, the modified scheme consists of using Saul'ev-up to get the (n+1)st time step, Saul'ev-down to get the (n+2)nd time step, and averaging the values at the nth and (n+2)nd time steps to obtain a more accurate value of the variable predicted at the (n+1)st time step. In the next step, Saul'ev-down and Saul'ev-up schemes are used in analogous fashion. The marching process then continues through the model integration.

Testing the Model

The accuracy of the finite difference scheme was tested by solving two problems that have analytic solutions. First, (2.1) was reduced to the equation used in the Ekman spiral by setting to zero the local acceleration and the damping term and by requiring that the pressure gradient term be constant in time and height. The boundary conditions were no-slip at the bottom and geostrophic at the top. Initially $\vec{V}$ was constant in height and equal to zero. Convergence to the analytic Ekman solution occurred in 36 hours. When the upper boundary condition was generalized by using no stress rather than the geostrophic condition, convergence occurred at 84 hours. When the damping term was added, convergence occurred more rapidly in both cases, as expected.

The second test involved Stokes' second problem. Schlichting (1968) showed that the oscillation of a flow over a flat plate sinusoidually in time with the lower boundary condition

$$U(0,t) = U_0 \cos(nt)$$

obeyed the equation

$$\frac{\partial U}{\partial t} = K \frac{\partial^2 U}{\partial z^2} .$$

The solution was a vertically damped harmonic oscillation. In the model this problem was equivalent to prescribing the pressure gradient force as sinusoidal in time, by neglecting the Coriolis force and damping terms, and by using the no-slip condition at the bottom of the model and no stress at the top, along with the initial condition of zero wind. When $U(z)$ was plotted with respect to the forcing function, the damped harmonic oscillation was obtained after an initial adjustment period.

3. Single Station Tests

As mentioned in Section 2, the damping coefficient was empirically determined. In order to find the most realistic results, six numerical experiments were conducted for the grid point corresponding to Columbia, Missouri, in order to evaluate the accuracy of the model in terms of the observed wind field. Table 1 summarizes the differences between the various attempts.

Before considering the various experiments, we examine Figure 1 in which the observed winds are shown for the duration of the model run, from 0600 GMT on 16 March 1965 (referred to as time = 0 hr), to 1800 GMT on 19 March 1965 (referred to as time = 84 hr). Features especially apparent and important are the strong clockwise turning of the wind with height in the first 12 hr, the maximum wind of 25 mps between 30 and 42 hr, and the slight backing of the wind with height after 42 hr. In Figure 1b, the observed surface pressure ascendent components are shown, illustrating that the strongest winds correspond to the strongest pressure gradient. Notice, however, in the model that a step function is used for the pressure (and temperature) gradients rather than a smooth function because the observed forcing functions were available only at three-hour intervals.

In Experiment 1, the simplest solution of (2.1) was sought. The results shown in Figure 2 are useless from a practical point of view and thus provided the motivation for the addition of the damping term. The most noticeable failure of the model is the 90 mps winds found at about 1000 m at 39 hr. Interestingly, the wind speed and direction undergoes an 18 hr oscillation after the 39th hr, corresponding to the inertial period for this latitude. Such an oscillation above the boundary layer is termed inertial-like as opposed to inertial because it results from a local imbalance between the pressure gradient and Coriolis forces locally. The classic inertial oscillation is a Lagrangian concept as contrasted to the Eulerian reference frame used here. In Figure 2, notice also that the wind at 6 hr does not show the strong clockwise turning with height that is observed.

To correct the problem of Experiment 1, the model was damped toward the steady-state wind appropriate for the instantaneous pressure gradient. Initial guidance for the size of the damping was provided by the theoretical results given by Blumen (1967). In the barotropic case, the steady-state wind was the Taylor wind. The damping coefficient of 1/2 f somewhat reduced the strong winds and the inertial-like oscillations. Next, the damping was increased in Experiment 3 to the value of the Coriolis parameter. Although the turning of the wind with height was not reproduced, the wind maximum of 35 mps at 39 hr was more reasonable. In both experiments, the cross-isobaric angle used in the Taylor wind solution, toward which the model was being damped, was kept constant at 40°. Although this value was unusually large (Petterssen, 1956), the observed cross-isobaric angle was even larger.

The lack of the turning of the wind with height suggested that the actual pressure gradient vector was not constant in height.

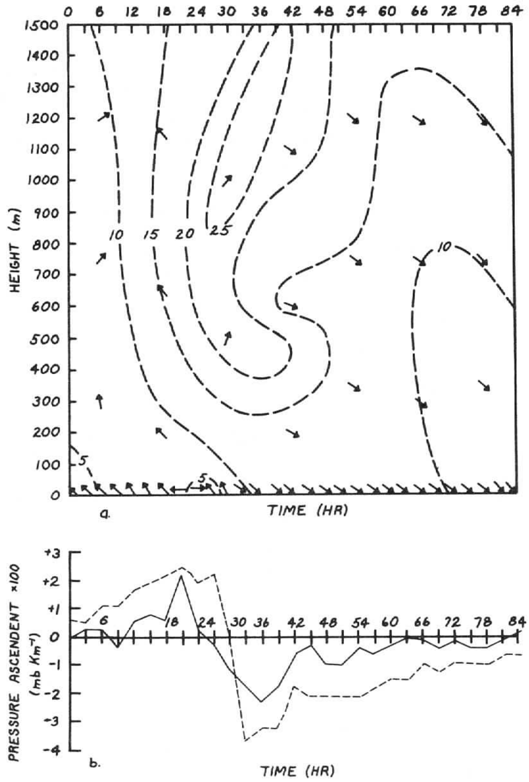

Figure 1. The (a) observed winds (m sec^{-1}) and (b) sea level pressure ascendent (mb/100 km) at Columbia, Missouri. Solid line is $\partial p/\partial y$ and dashed line is $\partial p/\partial x$.

Table 1

The Experiments Corresponding to Columbia, Missouri

Experiment	Pressure gradient	Damping coefficient	Surface cross-isobaric angle used in Taylor or TTW solution	Frequency at which gradients are evaulated
1	barotropic	0	not applicable	every 3 hrs
2	barotropic	1/2 f	40°	every 3 hrs
3	barotropic	f	40°	every 3 hrs
4	baroclinic	f	40°	every 3 hrs
5	baroclinic	linear 0 at $z = 0$ f at $z = 1500$ m	varies according to (4.1)	every 1 1/2 hrs
6	baroclinic	tan h $(\frac{z}{500})$ (f) 0 at $z = 0$ f at $z = 1500$m	varies according to (4.1)	every 1 1/2 hrs

Note: In all six experiments, $K = 5\ m^2/sec$ (after Hess, 1959), and $C_D = 1.2 \times 10^{-3}$ (after Cressman, 1961).

Therefore, in Experiment 4 the baroclinic atmosphere was considered. For simplicity, the damping was toward the algebraic sum of the Taylor and thermal wind (TTW) solutions, although this approach resulted in some distortion of the TTW solution near the surface. The noticeable change with the introduction of baroclinicity was the strong veering of the wind prior to 18 hr. Some backing of the wind was noticeable after 54 hr. The isotachs were no longer vertically oriented, indicating a less rapid and thus less forced adjustment to the changing pressure gradient.

Experiment 4, like the second and third experiments, was damped toward the TTW solution in which the surface cross-isobaric angle was maintained at 40°. However, to be consistent with the model in which the cross-isobaric angle is allowed to vary, the TTW should also be allowed to have a varying cross-isobaric angle. Eliassen and Kleinschmidt (1957) have shown this to satisfy

$$\frac{\sin \alpha}{(\cos \alpha - \sin \alpha)} = \frac{C_D \left| \vec{V}_g \right|}{\sqrt{2Kf}} \qquad (3.1)$$

where α is the cross-isobaric angle, C_D the drag coefficient, $\vec{V}_g$ the surface geostrophic wind, K the eddy diffusivity, and f

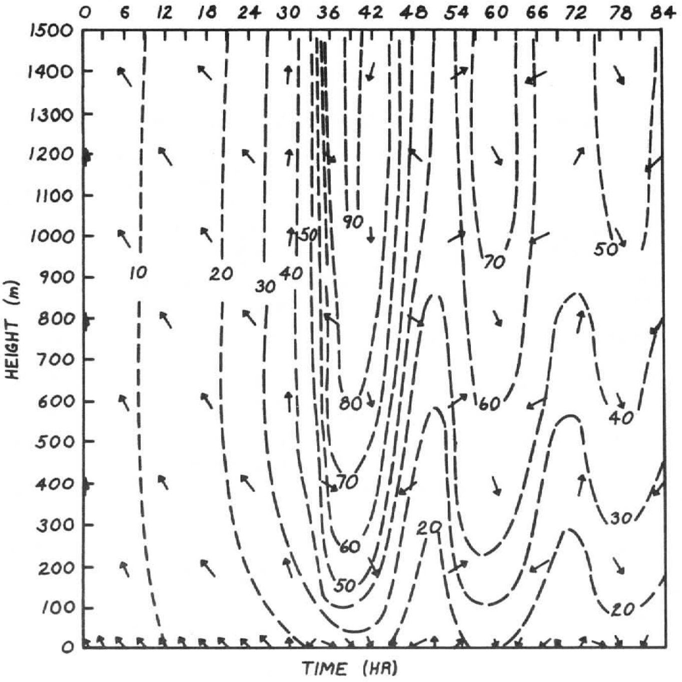

Figure 2. The model-forecast winds (m $\sec^{-1}$) at Columbia, Missouri in the first numerical experiment.

the Coriolis parameter. Since (3.1) is a transcendental relation for α, α was held constant in the second, third and fourth experiments. However, in the fifth and succeeding experiments, α was allowed to vary by solving (3.1) by the Newton-Raphson method (see, e.g., McCracken and Dorn, 1964). The lack of large cross-isobaric flow in previous experiments suggested that the damping in the model was too strong. Therefore, as part of Experiment 5, the value of the damping was lessened at most levels by making the coefficient a linear function of height ranging from zero at the earth's surface to f at the top of the model. This was done in order to give the model more freedom since the model-predicted low level winds had been too similar to the winds of the TTW. Additionally, in this experiment pressure and temperature gradients were interpolated at one and one-half hours to provide smoother forcing in the model. With these changes, the inertial-like oscillations reappeared and the maximum wind at 39 hr was again too strong (45 mps), apparently because the damping coefficient had been reduced too much. Moreover, the cross-isobaric flow was still not as great as observed.

For Experiment 6, the damping was changed to $[\tanh(\frac{z}{500})](f)$ where z is in meters. Essentially this gives the value of the damping coefficient as nearly linear in height from $z = 0$ to $z = 500$ m (as K goes from 0 to 1) and the nearly constant value 1.0 above 500 m. This means that substantial damping occurs above 500 m, but below this level the friction force is allowed to be the primary damping agent. The result is shown in Figure 3. It is encouraging to note similarities to the observed case shown in Figure 1. For example, the strong veering of the wind with height occurs until 18 hr, the wind maximum of 35 mps is somewhat strong but occurs only briefly, and the wind backs slightly with height after 54 hr. However, the surface winds after 42 hr lack enough westerly component which corresponds to a large cross-isobaric angle; in all six experiments this was a problem. The model-isotachs appear too vertically oriented, but precise comparisons are discouraged by the relatively infrequent observations used in Figure 1.

In order to examine the results of Experiment 6, a model-predicted hodograph for Columbia, Missouri, for the 30th hour is presented in Figure 4 along with the Taylor wind, the TTW and the observed wind. Recall that the model is being forced toward the TTW at each time step. Figure 4 shows that the model does poorly in predicting the wind in the lowest 50 m. However, above this lowest layer the model's wind forecast rapidly improves and between 500 and 1000 m is more realistic and certainly much better than the simple analytic solutions. Above 1000 m the model is still a better approximation to the real wind than either the Taylor wind or the TTW.

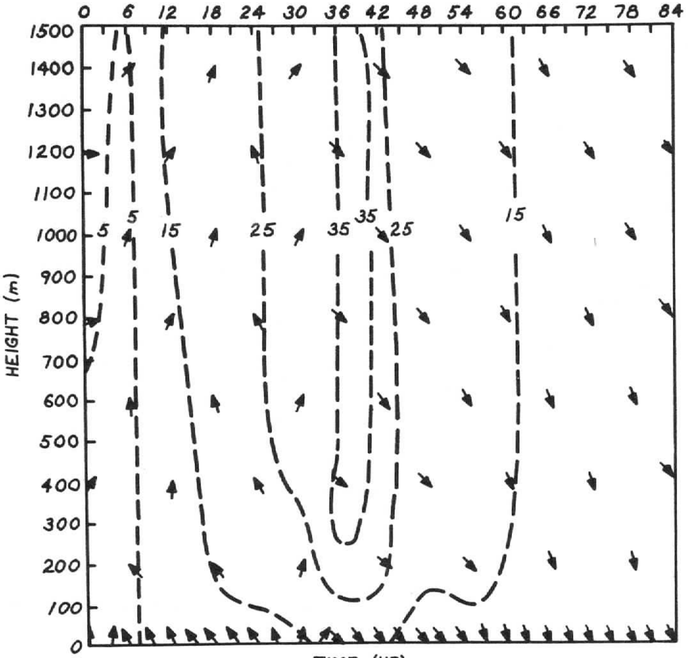

Figure 3. The model-forecast winds (m sec^{-1}) at Columbia, Missouri, in the sixth numerical experiment.

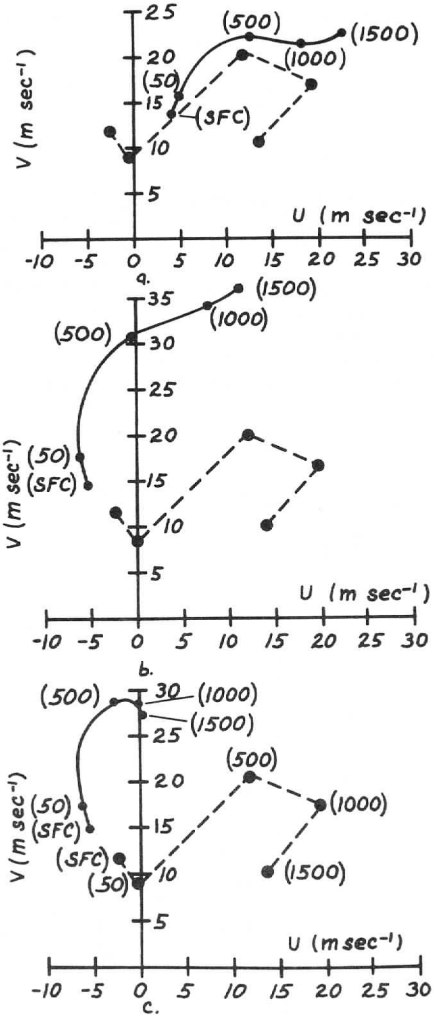

Figure 4. The model-forecast hodograph (a), the TTW-forecast hodograph (b), and the Taylor-forecast hodograph (c) for Columbia, Missouri, for 30 hr. Heights (m) are in parentheses. Large dots connected by a dashed line represent observed winds.

4. The Vertical Motion Forecast

The Evolution of the Storm

As mentioned in the last section, the parameters were adjusted at Columbia, Missouri, to yield as realistic results as possible. The one-dimensional linear model developed in this paper was run at the other 224 points of the 15 × 15 grid using the same parameters. The horizontal divergence was then computed at the interior 13 × 13 grid. Numerical integration of the incompressible continuity equation with the additional condition that there was zero vertical motion at the base of the model yielded vertical profiles and maps of vertical motion. In this chapter, the vertical motion pattern about the storm and its relationship to clouds, weather and precipitation rate are discussed. All figures in this section refer to observed or forecast information at 1200 GMT, 17 March 1965 (time = 30 hr), unless otherwise stated.

Figures 5, 6 and 7 show the evolution of the St. Patrick's Day storm. Figure 5 illustrates the track of the storm beginning with the fifteenth hour of the model run, since prior to this time the storm was outside the grid used in depicting the output in this paper from the model. The storm consisted of three stages: the first 20 hours was the developing stage when the storm intensified; the second 20 hours was the mature stage when the storm moved with little change in intensity; and the remaining 44 hours was the occluded or decaying stage. This storm was a typical Colorado low with the important features of a large isallobaric gradient, a dry tongue, and a low-level jet.

In the remainder of Figure 5, the model-forecast vertical motion at 1500 m is shown superimposed on the observed isobars for various times in the developing stage. Figure 5b shows the generally quiescent initial conditions, in which the vertical motion produced by the model is essentially that due to the TTW. The only area of significant ascent occurs in the vicinity of the cyclonically curved isobars in the Northern Plains. However, upward motion develops 6 hr later in northern Kansas and southern Nebraska as the pressure gradient intensifies. By 12 hr (Figure 5c), the low emerges onto the plains with noticeable vertical motion extending eastward across to southeastern Kansas.

As the storm reaches the mature stage, the vertical motion field becomes of greater interest. Figure 6 shows this developed stage. In Figure 6a, corresponding to 18 hr, the low is in southwest Kansas with upward motion in the convergence zone, which coincides with the surface warm front position. Such a distribution of vertical motion is to be expected from Ekman-Taylor considerations. However, at 24 hr when the low is well-developed, the axis of ascent extends eastward north of the warm front in the isallobaric fall center into Illinois. In effect, the convergence zone associated with the warm front is found north of the warm front because of the isallobaric wind. At 30 hr, the large storm's circulation is influencing most of the Midwest with upward motion evident from the low center to northern Illinois and eastward to Kentucky. Especially notable is

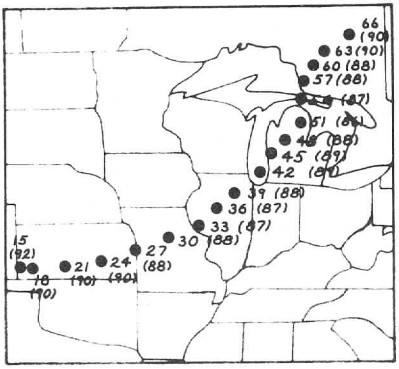

a. STORM TRACK

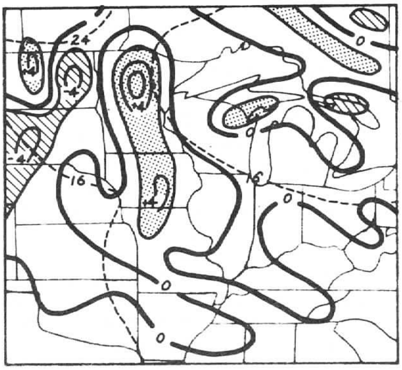

b. VERTICAL MOTION TIME 00 HR

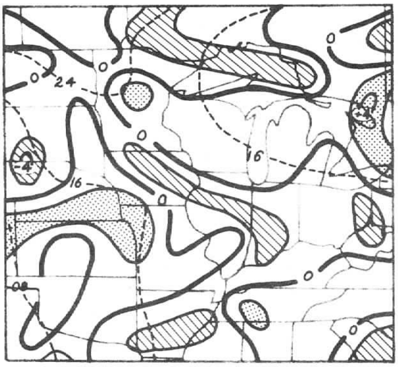

c. VERTICAL MOTION TIME 6 HR

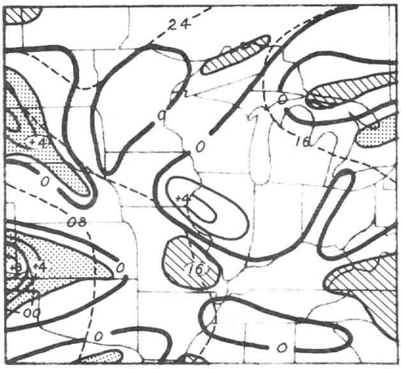

d. VERTICAL MOTION TIME 12 HR

Figure 5a. Track of the storm with dots indicating location of center at given time and lowest pressure in parentheses.

Figures 5b-d. Model-forecast vertical motion (cm sec^{-1}) at 1500 m (solid lines) and observed isobaric pattern (dashed lines). Shaded area represents vertical motion greater than +2 cm sec^{-1} and hatched area depicts vertical motion less than -2 cm sec^{-1} .

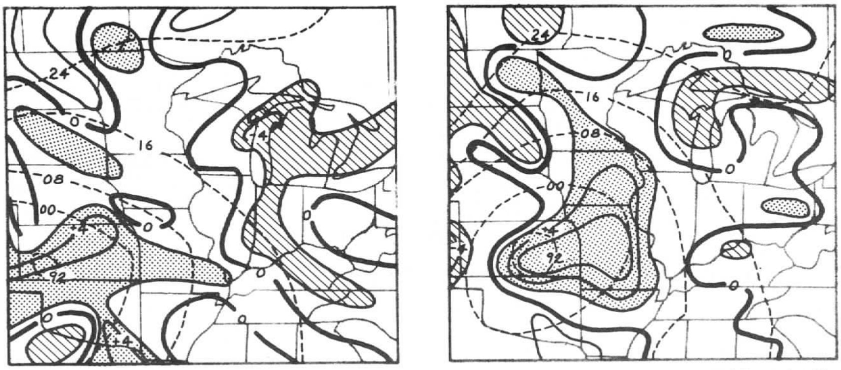

a. VERTICAL MOTION TIME 18 HR

b. VERTICAL MOTION TIME 24 HR

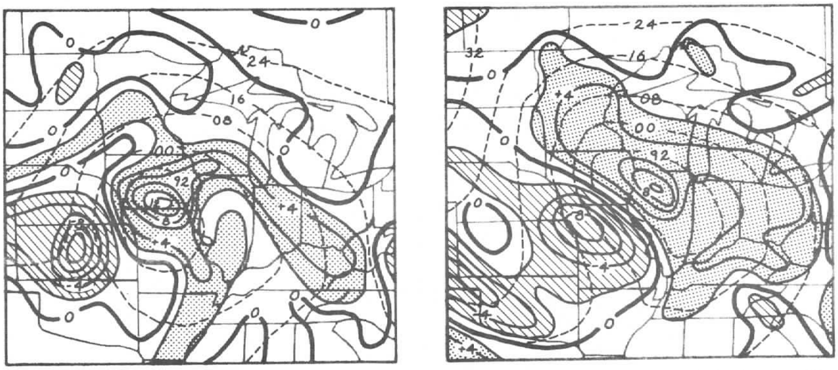

c. VERTICAL MOTION TIME 30 HR.

d. VERTICAL MOTION TIME 36 HR

Figure 6. Same as Figures 5b-d except times as indicated.

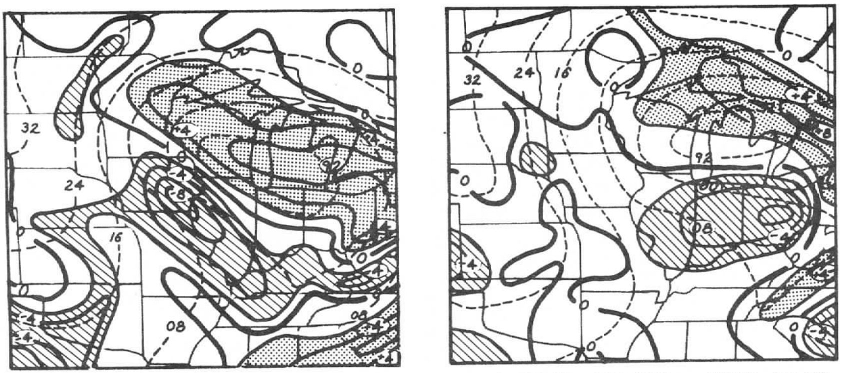

a. VERTICAL MOTION TIME 42 HR b. VERTICAL MOTION TIME 48 HR

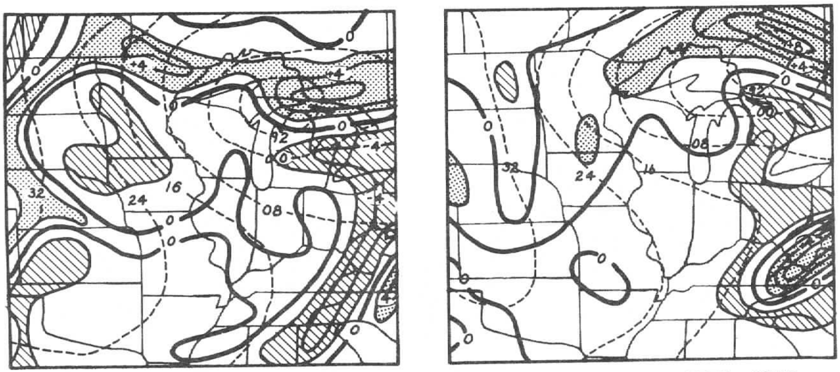

c. VERTICAL MOTION TIME 54 HR d. VERTICAL MOTION TIME 60 HR

Figure 7. Same as Figures 5b-d except times as indicated.

the strong subsidence over Kansas. The 30 hr output of the model will be examined in detail in this section and in Section 5. The vertical motion at 36 hr again lacks correspondence to fronts which can be inferred from the isobaric troughs. The strong sinking continues on the southwest side of the low.

As the storm reaches the occluded stage, the vertical motion field becomes of less interest. With the low over southern Lake Michigan, in Figure 7a, the pattern of ascent is becoming symmetric with respect to the storm center, which is typical of an occluded cyclone. In the same figure the upward motion that appears over the Carolinas is due to the development of a secondary low near the edge of the grid. The remainder of Figure 7 depicts the decay of the storm. The atmosphere again returns to its quiet state and, although the model is run out to 84 hr, no output after 60 hr is presented here. Of interest in the occluded stage is the elongation of the upward motion pattern over the Great Lakes in the vicinity of the curved isobars. The lack of large pressure gradient changes during the dying stage essentially reduces this numerical solution to the analytic TTW solution.

Relating Forecast Vertical Motion to Weather and Precipitation

Since the vertical motion is not directly observed, the most useful way of qualitatively verifying the accuracy of the vertical motion forecast is to examine the observed weather pattern and check for correlation with the vertical motion forecast. In Figure 8a the low clouds (bases 2000 m or lower) and the surface weather are shown at 31 hr (the closest Weather Depiction chart that is available for comparison to the 30 hr forecast). Comparing this figure to Figure 8c, we see that the cloud distribution does not correspond closely to the upward motion forecast. However, cold advection is occurring at 850 mb throughout much of the area of downward motion in the Central Great Plains, and thus the clouds shown there could be formed by turbulent mixing rather than by systematic upward motion. The encouraging sign is that the axis of precipitation through Illinois, Indiana and Ohio roughly corresponds to the upward motion forecast.

In examining the correlation between forecast vertical motion and observed precipitation in Figure 8a, it is important to note that precipitation may occur despite some downward motion. Perhaps a more meaningful relationship is found by comparing Figure 8b with Figure 8c. Here we find that the precipitation amount on the northern Great Plains is almost all light and thus may not be well correlated with the actual vertical motion, let alone with the model forecast vertical motion. Admittedly, the precipitation is overforecast over Missouri. Note, however, that the southern boundary of the precipitation over the Great Plains agrees with the strong increase in downward motion.

More important, however, is the similarity between the axes of forecast ascent and precipitation rate which extend toward the east, northwest and south from the low in Figures 8b and 8c. The lack of ascent over Illinois is only temporary and can be ignored, for Figure 8d shows that considerable upward vertical displacement

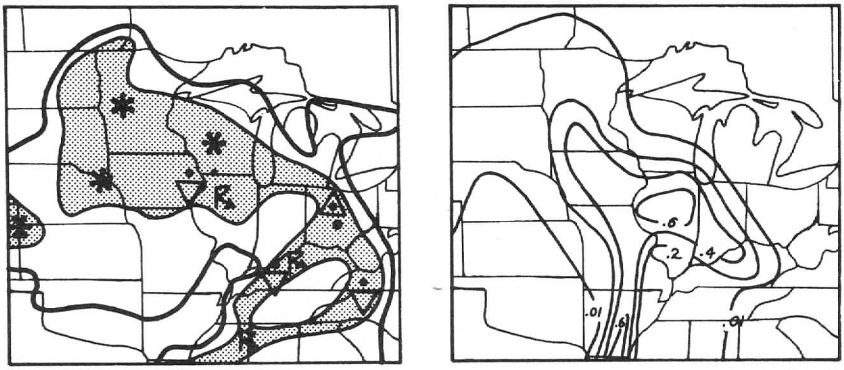

a. CLOUDS AND WEATHER TIME = 31 HR

b. 6-HR RAINFALL ENDING AT TIME = 30 HR

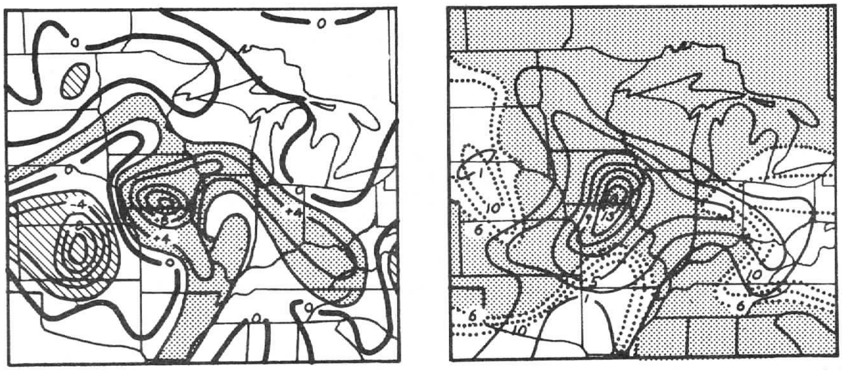

c. VERTICAL MOTION TIME = 30 HR

d. 6-HR POSITIVE VERTICAL DISPLACEMENT ENDING AT TIME = 30 HR.

Figure 8a. Observed clouds with bases less than 2000 m and weather.

8b. Observed precipitation (inches) during the past 6 hr.

8c. Model-forecast vertical motion (cm sec^{-1}) at 1500 m. Shaded area represents vertical motion greater than +2 cm sec^{-1} and hatched area depicts vertical motion less than -2 cm sec^{-1}.

8d. Model-forecast 6-hr positive vertical displacement shown by solid lines. Observed surface $T - T_d$ (temperature-dewpoint depression (°F)) in dotted lines. Shaded area represents $T - T_d$ 6°F .

occurred in this area during the previous six hours. The discrepancy between the lack of large upward vertical motion and the observed heavy rainfall is due to convection. Of course, for precipitation to occur in an area of upward motion, there must be sufficient moisture. Qualitatively, moisture is accounted for in Figure 8d by isoplething the observed surface temperature-dewpoint spread. For example, the dewpoint spread is so large in southwest Missouri that despite the large upward motion forecast, little if any precipitation can be expected, as is observed.

The relationship between forecast vertical motion and observed precipitation rate becomes more apparent by examining the relation between these two quantities at fixed points.

Figure 9 shows area averages of slightly time-smoothed forecast ascent at 1500 m, observed 6 hr precipitation rate, and observed surface dewpoint spread. Each graph is placed at its proper location relative to the instantaneous storm center. Notice the very good correlation over central Michigan, central Missouri and central Tennessee. Over south-central Missouri (Figure 9c) the agreement is still good and even more plausible when one qualitatively includes the available moisture variations.

Shifting from an Eulerian to a Lagrangian reference frame, we consider, in Figure 10, the precipitation rate and the vertical motion forecast with respect to the moving storm center over a two-day period. The correlation between ascent and dR/dt is best at the storm center and fairly good at the other points, which are 400 km from the center, when moisture is considered. If points 200 km from the moving low center are considered (not shown), the correlation is even better, but this is not surprising since Ekman convergence near the low center is to be expected.

Profiles of Vertical Motion

Having presented the horizontal map distribution of vertical motion, we next consider the vertical distribution which, for Columbia, Missouri, is shown in Figure 11. For the first 21 hr the vertical motion is negligible. For the period from 24 to 30 hr, the vertical motion is nearly linear with height, suggesting a substantial isallobaric effect (Young, 1972). At 33 hr the profile is nearly Ekman-like, as can be seen by noting that the 2 cm sec^{-1} isopleth is nearly vertical above 500 m (indicating little convergence above this level). The Ekman-like profile is also found shortly after the downward motion begins and again after 48 hr. Notice that the largest vertical motion always occurs at the top of the model.

As in the last section, a Lagrangian reference frame is also used in looking at the vertical motion profiles. Only a brief summary of the results is presented here. The profiles are Ekman-like within a 200 km radius of the center regardless of the stage of the storm. However, the magnitude of the model forecast vertical motion is larger than that due to the TTW. If a 400 km radius of the moving storm center is considered, large departures from Ekman-induced vertical motion are apparent in the mature stage, where the vertical

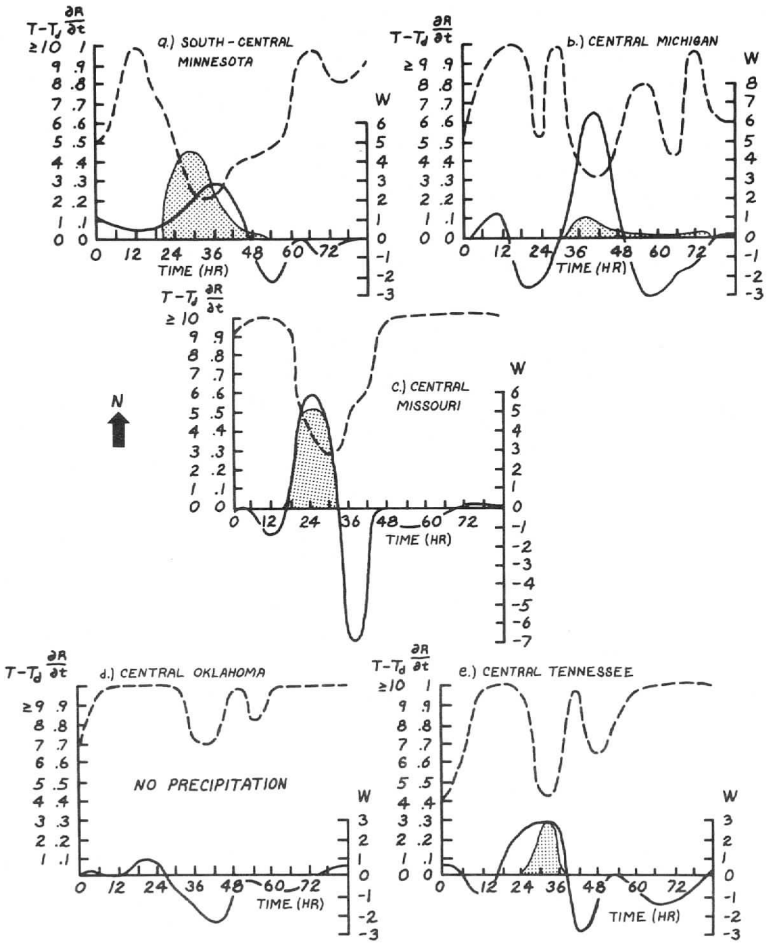

Figure 9. Model-forecast vertical motion at 1500 m, W (cm sec^{-1}), shown by thick, solid lines; observed 6 hr precipitation rate, ∂R/∂t(inches/ 6 hr), shown by shaded area; and observed surface temperature-dewpoint depression, T - T_d (°F), shown by dashed lines for the various locations.

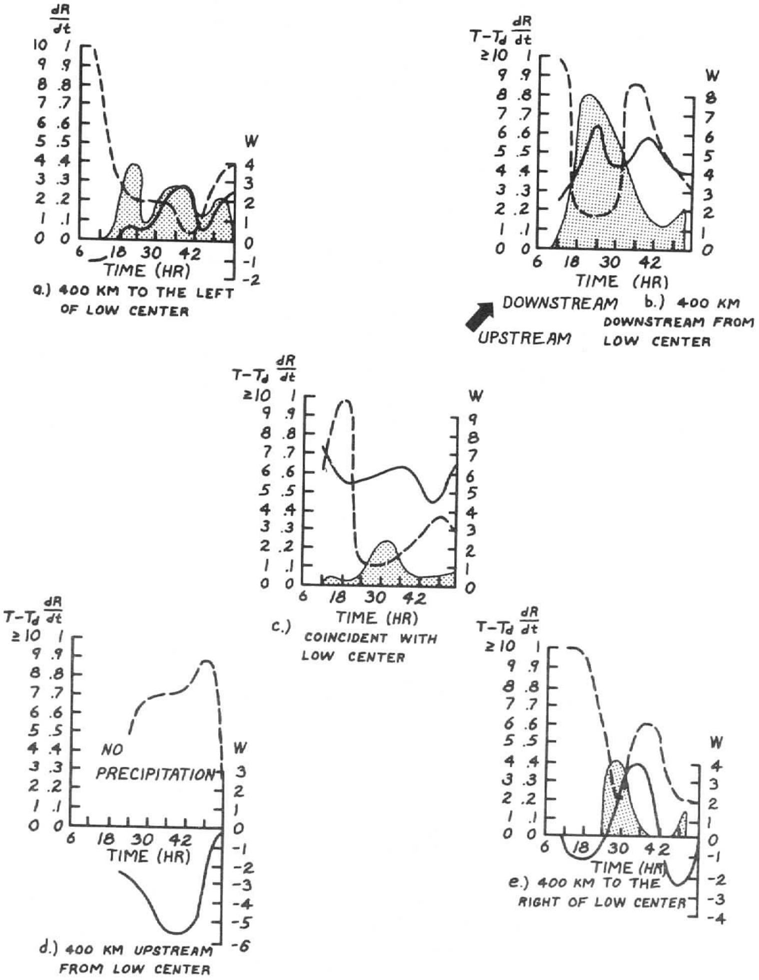

Figure 10. The following quantities are depicted with respect to the moving storm center: the model-forecast vertical motion at 1500 m, W (cm sec^{-1}), shown by thick, solid lines; observed 6 hr precipitation rate, dR/dt (inches/6 hr), shown by shaded area; and observed surface temperature-dewpoint depression, $T - T_d$ (°F), shown by dashed lines.

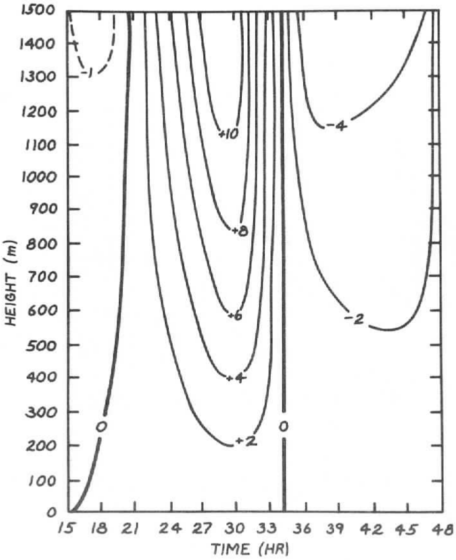

Figure 11. Model-forecast vertical motion (cm sec^{-1}) for Columbia, Missouri.

motion increases linearly in height similar to the 24-30 hr period in Figure 11. Again the vertical motion is larger than that due to the TTW with the largest departures from the TTW vertical motion occurring during the mature stage.

The Model Vertical Motion Forecast vs. the TTW Forecast

In this section the departures of the model forecast vertical motion from that due to the TTW are examined in Figure 12. Notice that at 500 m the departures are already evident. Striking differences in magnitude occur at 1000 m. As shown in the section on precipitation rates, the 1000 m model-forecast ascent appears reasonable in connecting the area of upward vertical motion from southern Wisconsin to eastern Tennessee. Notice also that the maximum value of ascent in the model appears north-northeast of the TTW ascent maximum, over southern Iowa, in closer agreement to the observed weather. Third, the model indicates strong subsidence over the Central Plains which is not at all expected from TTW considerations. Radiosonde observations at Dodge City, Kansas, and North Platte, Nebraska, indicate the formation of a strong subsidence inversion which suggests that the model forecast of strong descent is accurate. Because the radiosonde observations also show the cloudiness over the Plains to be low and thin, the explanation that the clouds are formed by turbulent mixing due to cold advection rather than ascent seems reasonable.

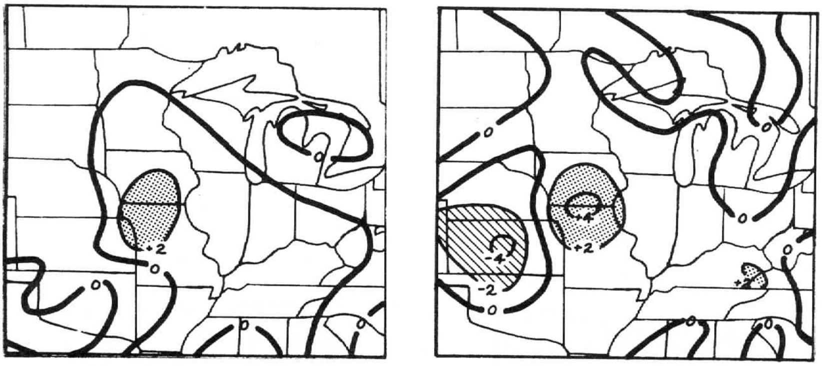

a.) TTW-FORECAST VERTICAL MOTION AT 500 M

b.) MODEL-FORECAST VERTICAL MOTION AT 500M

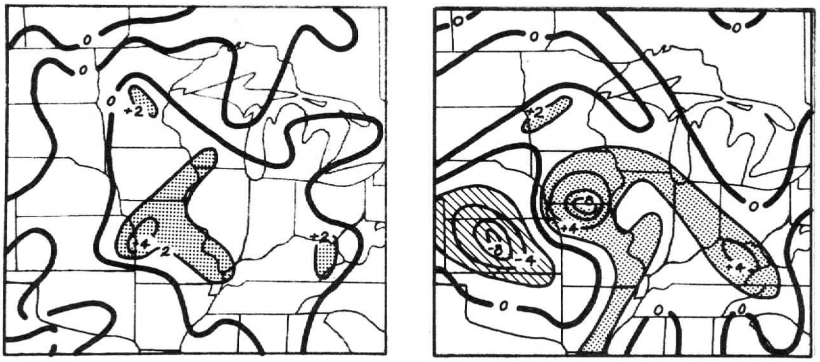

c.) TTW-FORECAST VERTICAL MOTION AT 1000 M

d.) MODEL-FORECAST VERTICAL MOTION AT 1000 M

Figure 12. Forecast vertical motion (cm sec^{-1}) by model or by TTW, as indicated, valid at 30 hr for given level.

5. Model-Predicted Winds and Related Quantities

Winds

In this section the winds from the model are compared to both the observed wind field and those that are expected from a simpler theory. Using these forecast winds, three-dimensional trajectories, vorticity and the isallobaric wind are derived. All figures in this section refer to 1200 GMT, 17 March 1965 (30 hr), unless otherwise stated.

As was shown in the hodograph for Columbia, Missouri (Figure 4), the winds in the lowest 100 m are not predicted well. Figure 13 shows that in general the TTW solution is slightly better than the model at the surface. In interpreting the results in this paper,

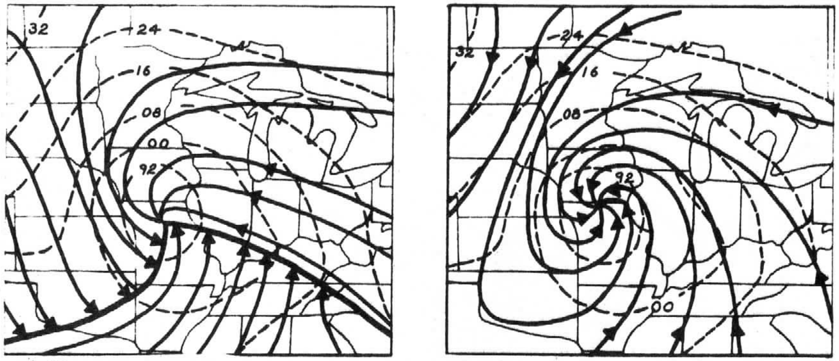

a.) OBSERVED-SURFACE

b.) MODEL - SURFACE

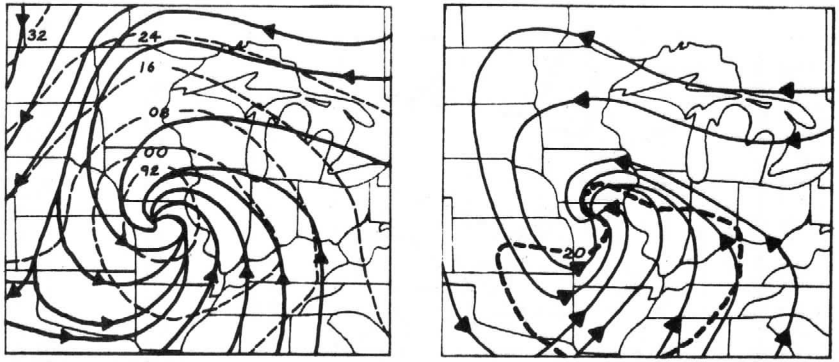

c.) TTW - SURFACE

d.) OBSERVED - 500M

Figure 13a-d. Observed or forecast streamlines (thin, solid lines) valid at the surface for 30 hr. Observed isobars are shown with dashed lines and observed wind shift lines in (a) by thick, solid lines.

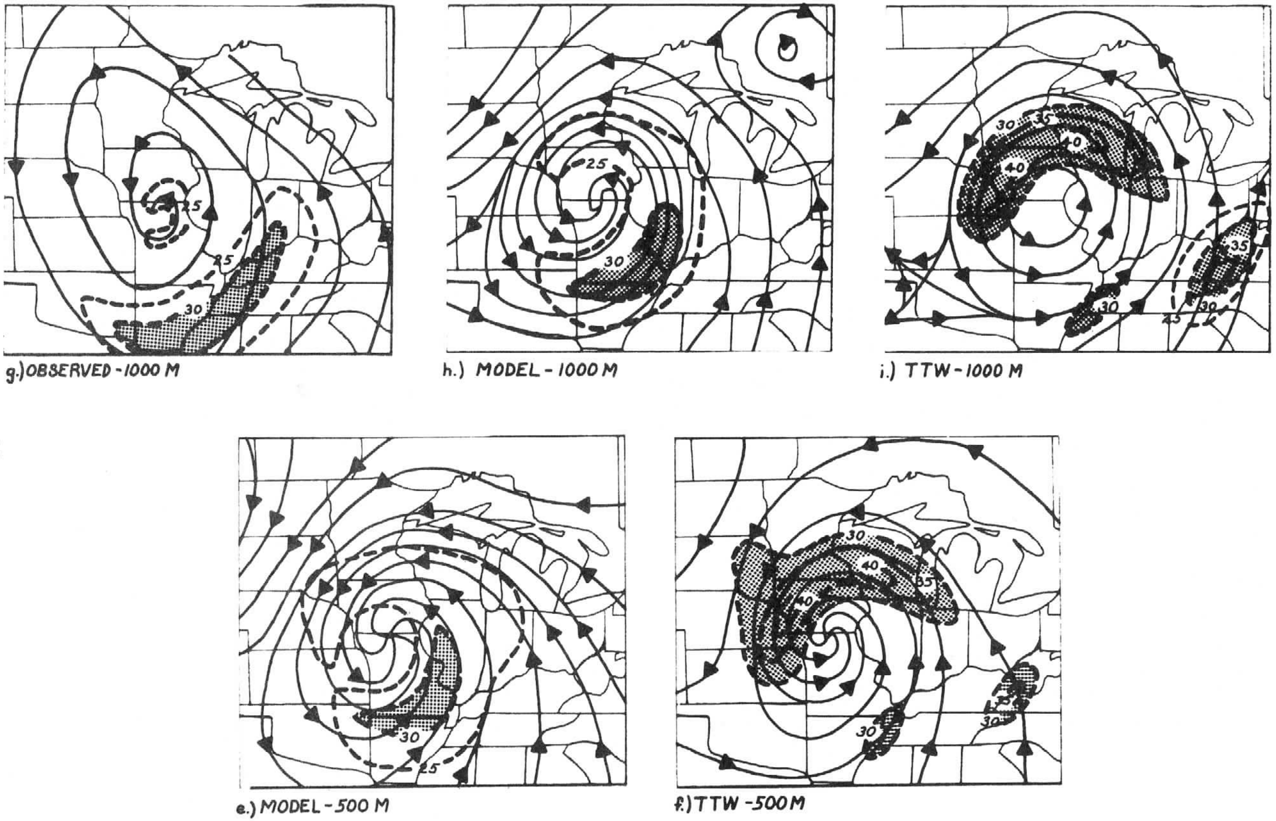

g.) OBSERVED - 1000 M h.) MODEL - 1000 M i.) TTW - 1000 M

e.) MODEL - 500 M f.) TTW - 500 M

Figure 13e-i. Observed or forecast streamlines (thin, solid lines) and isotachs (m sec^{-1}) shown by dashed lines valid at given level at 30 hr. Shaded areas represent wind speeds greater than 30 m sec^{-1}.

recall that "surface" refers to the base of the Ekman layer and not the surface of the earth. The wind in both models lacks the strong shear in the horizontal that is observed across the lower Midwest. Especially puzzling and disappointing are the results over the northern Great Plains where strong cross-isobaric flow does occur, while in the model the cross-isobaric wind is almost negligible. Ironically, the isallobaric component of the wind over the northern Great Plains is such that it mostly cancels the normally frictionally induced ageostrophic wind. Despite this failure at 30 hr, the model does correctly predict the 90° cross-isobaric flow at 18 hr over Kansas (not shown).

At higher levels the model-forecast-wind becomes more like the real atmosphere. Comparing Figures 13d,e, and f, we see that 500 m jet cores are forecast, by both the TTW and the model, and are observed. Notice that the jet core in the model extends somewhat around the northwest side of the storm, unlike the actual jet core. This is probably due to the damping effect which forces the model toward the TTW solution which, as can be seen from Figure 13f, has a very strong and anomalous jet core from Wisconsin to eastern Kansas. This suggests the damping used in the model causes some overemphasis of the geostrophic flow. The jet maximum over eastern Kentucky predicted by the TTW formulation is neither forecast by the model nor observed. Over the lower Midwest the model's wind directions are becoming more accurate while those of the TTW are not.

The anomalous jet core shown at 500 m is more evident at 1000 m, as shown in Figure 13g, h, and i. In contrast to the 500 m level, however, the 1000 m TTW directions are becoming similar to the model's 1000 m directions.

Trajectories

As previously discussed, the model's output contains both horizontal winds and vertical motion. Therefore, trajectories can be computed and are presented in this section. Before examining them, it is important to realize that in this model (and probably in the real atmosphere) large horizontal gradients in vertical motion and large vertical wind shear are forecast. Thus, a small error in the predicted wind and vertical motion fields yields an important error in the trajectory. In this section, the trajectories that are shown were manually computed from the three-hourly output of the model.

In Figure 14, air parcels that were initially at either 500 m or 1500 m at 30 hr were followed until they passed through either of these surfaces. The 500 m surface was chosen as a lower boundary for depicting these trajectories since there was little vertical motion below this level and hence the motion was quasi-horizontal. Figure 14 shows that most of the ascending parcels were cyclonically curved while descending parcels curved anticyclonically. Notice that some of the parcels that were initially ascending from 500 m later descended back down through the 500 m level as the low passed by.

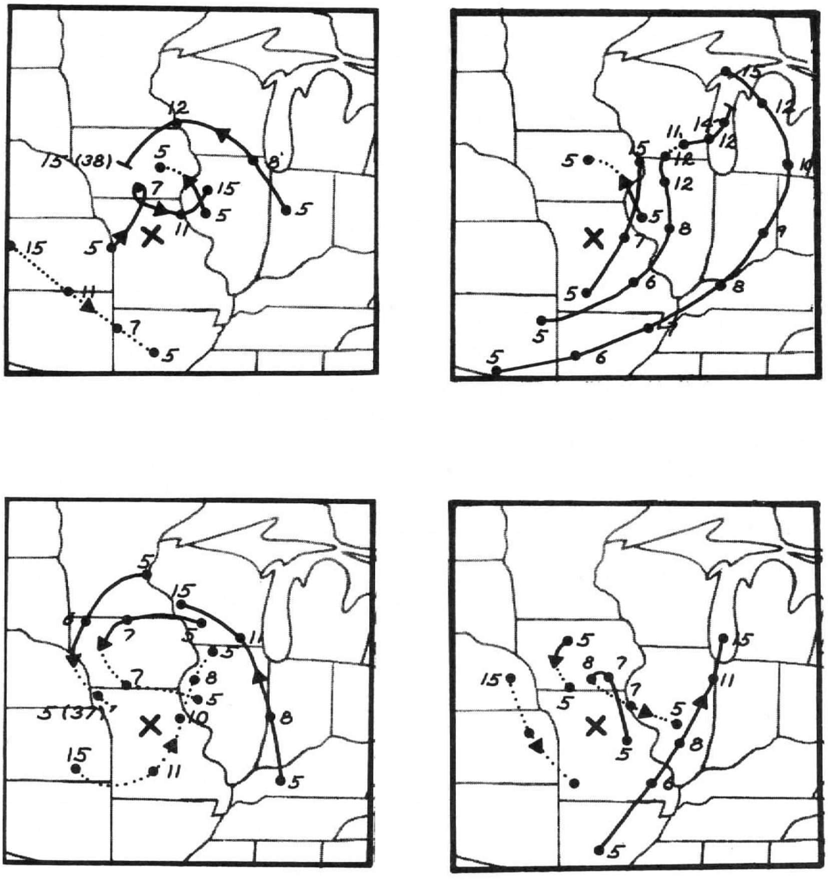

Figure 14. Model-forecast trajectories beginning at 30 hr at either 500 m or 1500 m. Numbers indicate height × 100 of parcel (in m) at 3 hr intervals (shown by dots). The hour that a parcel goes through either the 500 m or 1500 m level, if other than indicated by a dot, is shown in parentheses. Location of low center at 30 hr is shown by ✕.

Vorticity

Another quantity that is useful in examining horizontal winds is the vertical component of vorticity. In Figure 15, the forecast vorticity at the bottom and top of the model is shown. Direct comparison to the observed vorticity pattern was not attempted due to the lack of a sufficiently dense surface station network. Qualitatively, however, we can see from Figure 13a that the actual surface vorticity center is located in northwest Missouri and this is forecast in Figure 15a. Notice also that the observed surface fronts shown in Figure 13a (corresponding to wind shift lines) are approximately oriented like the forecast surface vorticity pattern in Figure 15a.

Moreover, the vorticity in the boundary layer and the vertical motion at the top of the boundary layer are related. Charney and Eliassen (1949) have shown that the vertical motion at the top of an Ekman-Taylor layer is proportional to the geostrophic vorticity when the atmosphere is barotropic. In an extension of their work, Young (1970) has shown that in a baroclinic atmosphere, the vertical motion is proportional to the geostrophic vorticity at some intermediate level in the boundary layer. By comparing Figure 15b with Figure 8c, it can be seen that a fairly good correlation exists between the 1500 m forecast vorticity and the 1500 m forecast vertical motion over the Midwest. However, the strong subsidence over Kansas (Figure 8c) does not agree with these simple relationships between vorticity and vertical motion and is thought to be an isallobaric effect. Surprisingly, analysis of the 1500 m vorticity computed from the TTW (not shown) corresponds better to the model's vertical motion than to its own vertical motion field.

The Isallobaric Wind

As a final discussion of the model's results, we look at the component of the wind associated with the changing pressure gradient. In Figure 16a the isallobaric field at 30 hr is shown. According to Brunt and Douglas (1928), the isallobaric wind is strongest where the isallobaric gradient is largest and the wind blows parallel to the isallobaric gradient. Likewise, the local acceleration should be oriented along the isallobars with lower values to the left. As can be seen from Figure 16, the local acceleration is largest over western Missouri where the isallobaric gradient is largest. Notice that the direction of the local acceleration is deviated toward the left of that expected from the Brunt-Douglas theory, in apparent accord with the theoretical results of Young (1972).

Related to the local acceleration is the local Rossby number which can be defined as

$$R_0 \equiv \frac{\left|\frac{\partial \vec{V}}{\partial t}\right|}{|f\vec{V}|}$$

which is the ratio of the local acceleration to the Coriolis force. In Figure 17, surface values of R_0 are shown to be largest, in

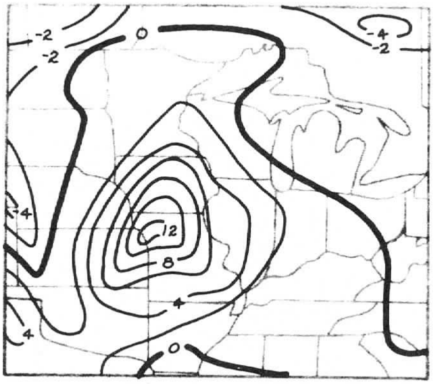

a.) MODEL-FORECAST RELATIVE VORTICITY AT SURFACE

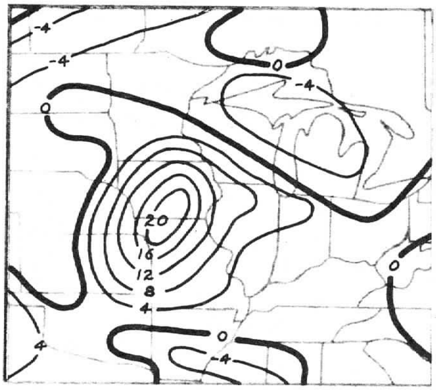

b.) MODEL-FORECAST RELATIVE VORTICITY AT 1500 M

Figure 15. Model-forecast relative vorticity (10^{-5} sec^{-1}) at given level for 30 hr.

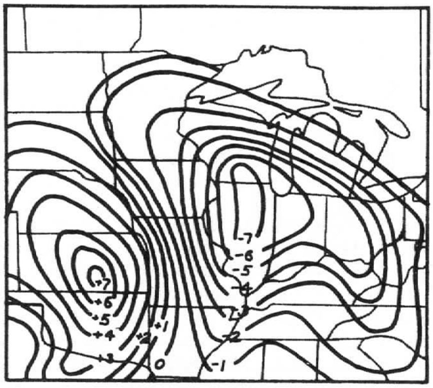

a.) OBSERVED ISALLOBARIC PATTERN AT 30 HR

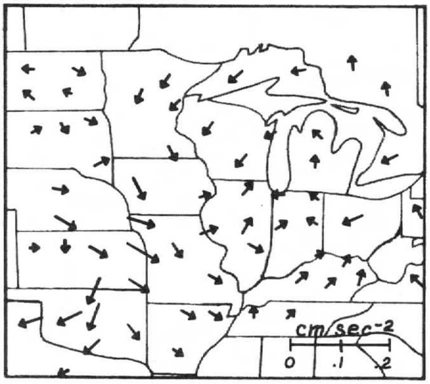

b.) MODEL-FORECAST LOCAL ACCELERATION AT 30 HR

Figure 16a. Observed isallobars (mb/3 hr) for 30 hr.

16b. Model-forecast local acceleration (cm sec^{-2}) for 30 hr. Arrow lengths indicate magnitude of local acceleration.

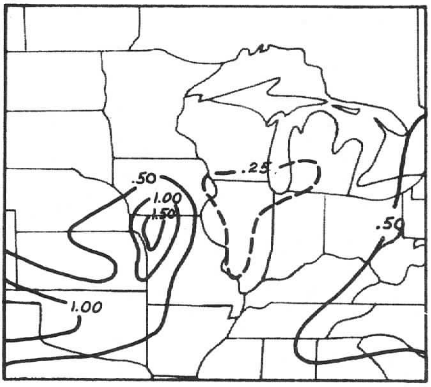

Figure 17. Model-forecast local Rossby number evaluated at the surface at 30 hr.

general, where the isallobaric gradient is large except over the Great Lakes. The importance of R_0 is that its departure from zero is a dynamically significant measure of the unsteadiness of the flow at the surface during this storm.

6. Conclusions and Discussion

This model has shown that integration of the horizontal equations of motion with the local accelerations included and inertial terms neglected produced some realistic results in a storm situation, provided the inertial-like oscillations resulting from an imbalance between the Coriolis and pressure gradient forces were controlled. The determination of a reasonable damping coefficient in forcing the model solution toward the steady-state solution was critical. In this model, a hyperbolic tangent profile of the damping coefficient from zero to the Coriolis parameter as height increased proved to be a useful formulation.

The results from the model showed that baroclinicity cannot be ignored in the boundary layer during a storm. In the case studied, the turning of the geostrophic wind with height was frequently much stronger than the normal veering of the wind found in the Taylor wind spiral.

The surface winds forecast in the model were, in general, slightly stronger than the corresponding observed winds; however, this resulted partly from the lower boundary condition, which was appropriate for the base of the Ekman layer and not the base of the surface layer. Conceivably, the results could be reduced downwards to a surface value by use of a logarithmic wind profile. However, since the main emphasis in the paper was to compute the vertical motion profile and since the contribution to this motion was negligible in the surface layer for large-scale systems, the wind reduction was not performed. Furthermore, the forecast surface winds lacked enough cross-isobaric components.

The vertical motion forecasts that were computed from the model appeared consistent with the observed precipitation rate. Forecast ascent resulting from the convergence produced by the model occurred near the low pressure center and also, in general, in the isallobaric fall center which is qualitatively verified by synoptic experience.

The relation between the observed precipitation rate, the surface-temperature dewpoint spread, and the forecast ascent was so useful that the author believes that this model could be used operationally as guidance if reasonably good surface pressure and temperature gradients and surface moisture forecasts were available from a larger numerical model. Alternatively, the results suggested that current prediction models would benefit from improved vertical resolution in the boundary layer. Obviously improvements could be made in the model. First, inclusion of the inertial terms are important since they are frequently of the same magnitude as that of the local acceleration. Furthermore, the inertial terms are needed in order to model the boundary layer supergeostrophic flow that partially results from the downward advection of momentum from the free atmosphere. Second, inclusion of a thermal wind due to the slope of the Great Plains might account for some of the poor wind results forecast over the northern Great Plains. Third, a spatially and temporally varying eddy exchange coefficient could replace the constant K used in this model. However, the determination of how K should vary in a changing pressure and temperature field could be a very difficult problem to overcome.

In conclusion, there are problems remaining in modelling the boundary layer under realistic conditions. In this paper we have considered only a storm situation in which departures from the steady state are large. While this simple model has produced some reasonable results, the modelling of the surface layer, the Ekman layer and the free atmosphere above require continued research.

Acknowledgments

Suggestions made by Professor Donald R. Johnson and Professor Frank Sechrist are appreciated.

This research was supported by the National Science Foundation under Grant GA-30676 and the National Oceanic and Atmospheric Administration under Grant E-230-68-(G) to the Space Science and Engineering Center at the University of Wisconsin, Madison.

Finally, we express our appreciation to the National Weather Service for granting R. J. Naistat a year of leave in order to pursue this research.

References

Blackadar, A. K., 1962: "The Vertical Distribution of Wind and Turbulent Exchange in a Neutral Atmosphere," J. Geophys. Res., 67, 3095-3102.

Blackadar, A. K., 1965: "A Single Layer Theory of Vertical Distribution of Wind in a Baroclinic Neutral Boundary Layer," Final Rept., Contract No. AF(604)-6641, Penn. State Univ., AFCRL-65-531, pp. 1-22.

Blumen, W., 1967: "Energy Partition in a Barotropic Atmosphere," Tellus, 19, 174-182.

Brunt, D. and Douglas, C. K. M., 1928: "The Modification of the Strophic Balance for Changing Pressure Distribution, and Its Effect on Rainfall," Mem. R. Meteor. Soc., 3(22), 29-51.

Businger, J. A. and Ching, J. K. S., 1968: "The Response of the Planetary Boundary Layer to Time Varying Pressure Gradient Force," J. Atmos. Sci., 25, 1021-1025.

Cahn, A., 1945: "An Investigation of the Free Oscillation of a Simple Current System," J. Meteor., 2, 113-119.

Charney, J. G. and Eliassen, A., 1949: "A Numerical Method for Predicting the Perturbations of the Middle-Latitude Westerlies," Tellus, 1(2), 38-54.

Cressman, G., 1960: "Improved Terrain Effects in Barotropic Forecasts," Mon. Wea. Rev., 88, 327-342.

Ekman, V. W., 1905: "On the Influence of the Earth's Rotation on Ocean Currents," Ark. Mat. Astr. Fys., 2(11), 52 pp.

Eliassen, A. and Kleinschmidt, E., 1957: "Dynamic Meteorology," Handbuch der Physik, 48, Berlin, Springer-Verlag, 1-154.

Estoque, M. A., 1963: "A Numerical Model of the Atmospheric Boundary Layer," J. Geophys. Res., 68, 1103-1113.

Green, R. A., 1965: "The Weather and Circulation of March 1965," Mon. Wea. Rev., 93, 392-398.

Gross, E., 1970: "The National Air Pollution Potential Forecast Program," ESSA Technical Memorandum WBTM NMC 47, National Meteorological Center, Washington, D.C., May, 1970, 28 pp.

Haltiner, G. J., 1971: Numerical Weather Prediction, New York, John Wiley and Sons, Inc., 317 pp.

Hess, S. L., 1959: Introduction to Theoretical Meteorology, New York, Holt, Rinehart and Winston, 362 pp.

Holton, J. R., 1967: "The Diurnal Boundary Layer Wind Oscillation above Sloping Terrain," Tellus, 19, 199-205.

Kuo, H. L., 1971: "Axisymmetric Flows in the Boundary Layer of a Maintained Vortex," J. Atmos. Sci., 28, 20-41.

Larkin, B. K., 1964: "Some Stable Explicit Difference Approximations to the Diffusion Equation," Math. of Comp., 18, 196-202.

Lettau, H. H., 1962: "Theoretical Wind Spirals in the Boundary Layer of a Barotropic Atmosphere," Beit. Phys. Atmos., 35, 195-212.

Lorenz, E. N., 1963: "Deterministic Nonperiodic Flow," J. Atmos. Sci., 20, 130-141.

Ludlum, D. L., 1965: "Weatherwatch," Weatherwise, 18(3), 132-146.

Ludlum, D. L., 1966: "The Snowfall Season of 1964-65," Weatherwise, 19(1), 124-131.

Mahrt, L. J. and Schwerdtfeger, W., 1970: "Ekman Spirals for Exponential Thermal Wind," Boundary-Layer Meteorol., 1(2), 137-145.

McCracken, D. D. and Dorn, W. S., 1964: Numerical Methods and Fortran Programming, New York, John Wiley and Sons, 457 pp.

Ooyama, K., 1957: "A Study of Diurnal Variation of Wind Caused by Periodic Variation of Eddy Viscosity," Final Rept., Contract No. AF 19(604)-1368, New York Univ., College of Engineering, 80-135.

Palmen, E. and Newton, C. W., 1969: Atmospheric Circulation Systems, New York, Academic Press, 603 pp.

Pandolfo, J. P. and P. S. Brown, Jr., 1967: "Inertial Oscillations in an Ekman Layer Containing a Horizontal Discontinuity Surface," J. Marine Res., 25(1), 10-28.

Petterssen, S., 1956: Weather Analysis and Forecasting (Vol. 1, 2nd ed.), New York, McGraw-Hill, 428 pp.

Saul'ev, V. K., 1957: "Numerical Integration of Parabolic Equations," Dokl. Akad Nauk SSSR (NS), 117-36-39.

Schlichting, H., 1968: Boundary-Layer Theory, New York, McGraw-Hill, 747 pp.

Shuman, F. G. and Hovermale, J. B., 1968: "An Operational Six-Layer Primitive Equation Model," J. Applied Meteor., 7(4), 525-547.

Taylor, G. I., 1916: "Skin-friction of the Wind on the Earth's Surface," Proc. Roy. Soc., A(92), 196-199.

Washington, W. M., 1964: "A Note on the Adjustment Towards Geostrophic Equilibrium in a Simple Fluid System," Tellus, 16(4), 530-534.

Young, J. A., 1968: "Comparative Properties of some Time Differencing Schemes for Linear and Nonlinear Oscillations," Mon. Wea. Rev., 96(6), 357-364.

Young, J. A., 1970: "Mass Convergence in a Baroclinic Ekman Layer," Studies of the Atmosphere Using Aerospace Probings, Annual Report 1969, Contract No. ESSA E-230-68-G, Space Science and Engineering Center, Univ. of Wis., 211-223.

Young, J. A., 1972: "Isallobaric Air Flow in the Planetary Boundary Layer," Submitted to J. Atmos. Sci., 1972.

A NUMERICAL STUDY OF THE PRESSURE RESPONSE TO LIQUID-WATER DRAG IN A THREE-DIMENSIONAL CONVECTIVE SYSTEM

Robert D. Abbey and John A. Young

ABSTRACT:

The effects of pressure in deep convection have been studied with respect to a particular forcing mechanism: the weight of liquid water. The cardinal feature of the study was numerically solving a nonhomogeneous partial differential equation for pressure (a form of the anelastic balance equation). The forcing function of this equation was derived by a conversion of radar reflectivity values to a three-dimensional distribution of liquid-water content (LWC).

Individual vertical pressure (gradient and buoyancy) forces were computed and analyzed. The additive effect of the pertinent forces produced analyzed fields of net vertical accelerations. The three-dimensional character of the pressure response was seen to be significantly hydrostatic, but the sum of the pressure and drag forces produced a three-dimensional field of vertical accelerations which were highly irregular. This feature was attributed to the dynamic pressure contribution.

This first attempt to explicitly examine the dynamic effects of pressure demonstrated the need to properly take them into account in prognostic studies of convection. A discussion of the technique and its future application has been included.

1. Introduction

Convection is a common word in the lexicon of the meteorologist. As a topic of classical and modern scientific interest, the varieties of physical application which the word implies has suffered no dearth of investigators. The modern literature is particularly voluminous.

Long before Sir Isaac Newton rigorously developed the notions which led to the modern understanding of gravity and motion, Archimedes accountably understood the basis of the principle that a body wholly or partially immersed in a fluid is "buoyed up" by a force equal to the weight of the displaced fluid. It is important to realize, however, that this principle is independent of any internal forces of the fluid. If the immersed body is a hypothetical parcel of air and if the ambient fluid is also air, the parcel must remain coherent, not interacting with the environment. Also, in this case, pressure differences between parcel and environment are not allowed. This restriction on pressure has the effect, by virtue of the equation of state, to identify weight differences solely with temperature contrasts. In view of this, it would seem that an accurate description of a buoyant parcel should not only permit dilution by environmental air but also the modifying influences of pressure forces.

While for many years investigators sought mathematical and physical formulations to improve upon the classical parcel theory (a short but excellent review through 1959 is provided by Squires in the first chapter of Fletcher's The Physics of Rainclouds), it was only with the advent of the electronic computer that a more comprehensive view of atmospheric convection began to emerge. The numerical model provided an excellent vehicle to predict the consequences of mathematical constructions. Of course, the method proved to be fraught with intrinsic problems related to numerical techniques and the practicable limitations of the physical dimensions of the machine itself. For these reasons, most convection models have tended to be only one- or two-dimensional in space.

The simple but useful conceptual approach offered by the parcel theory serves as the foundation of the one-dimensional models. Limited to the vertical coordinate, however, parcel-environment interactions must be described through parameterizations. For example, Simpson and Wiggert (1969, 1971) modify the (thermal) buoyancy force by an "apparent mass coefficient based upon an inverse cloud-radius law (functionally related to altitude), and an aerodynamic (form) drag coefficient." This requires specifying the mass coefficient and two proportionality constants related to the other two parameterizations. The most attractive feature of this and other numerical models like it is the speed of calculation and relatively small machine storage requirements. They fail to demonstrate in any definite fashion, nevertheless, the fundamental forces which modify parcel (thermal, plume, etc.) accelerations associated with temperature contrasts.

Adding a horizontal dimension allows considerable relaxation of the necessity to parameterize so that forces and accelerations may be represented in exact, unparameterized form. Such models usually involve determination of the changing stream function by solution of the vorticity equation. While this procedure ensures proper handling of the implicit pressure forces, their explicit role in producing parcel accelerations is not immediately evident.

In a unique study, Arnason et al. (1968) have attempted to recover the pressure effects explicitly by way of the diagnostic balance equation in a slab-symmetric model, 3 km on a side (i.e. shallow convection). A simulated precipitating roll cloud was achieved after initially introducing an axially symmetric, small warm bubble into a quiescent, stably stratified environment. After eight minutes of convection, the subsequent pressure field was decidedly "dynamic" in nature, differing dramatically from the associated hydrostatic field.

As a consequence of a systematic scale analysis, Ogura and Phillips (1962) have partitioned convection into two categories: shallow and deep. The convection is classified according to whether or not its vertical extent is much less than the dry adiabatic scale height (about 30 km). For both scales, a generalized Boussinesq approximation is applied to a perturbation form of the vector equation of motion, but there is an important physical and mathematical distinction associated with this approximation which is a direct result of the scale analysis. In the case of shallow convection, temperature fluctuations combined with gravity (thermal buoyancy) may be identified exactly with the analogous density changes. This is inappropriate in the case of deep convection where the pressure perturbations ("pressure buoyancy") must be taken into account. For a consistent set of equations, too, the two scales differ in the manner in which continuity of mass is expressed. For what is commonly referred to as the Boussinesq system (or shallow convection), the flow is simply nondivergent. For deep convection, while acoustic wave modes are suppressed through elimination of local density fluctuations, the vertical stratification of mean density is retained and the continuity equation reduces to a statement of nondivergent mass flux. This has been referred to as the anelastic approximation.

The three-dimensional, anelastic balance equation may be obtained by taking the divergence of the vector equation of motion (including a liquid-water drag force) and simultaneously applying the constraint of a nondivergent mass flux. The result may be considered as a diagnostic equation for pressure, the nonhomogeneous part of which is expressed as functions of thermal buoyancy, liquid-water drag and velocity. A spatial solution of the equation establishes values from which pressure forces and thus net forces may be computed.

It is against this background that a novel technique is here presented. The primary objective was to provide explicit information on the relationship of pressure and pressure forces to the dynamical properties of deep convection. As a necessary consequence of this relationship, an instructive link was established between a typical three-dimensional, spatial distribution of liquid-water content (LWC) in convective cells and the atmosphere's attendant disturbed pressure state.

Radar measurements were used to establish the three-dimensional liquid-water field of a system composed of two cumulonimbi; the data processing is discussed in Section 3. This field was then used to calculate the nonhomogeneous terms of the partial differential equation for pressure (a form of the balance equation). The mathematical derivation together with boundary conditions and numerical solution techniques for this equation are the topics of Section 2. Once pressure fields were obtained, the pertinent forces (in particular, the vertical forces), were investigated and are discussed in Section

4. The concluding section summarizes and indicates a direction for further study. Unless identified specifically in context, the variables used are defined in a list at the beginning of Section 2. All references to forces infer per unit mass.

2. Theory and Method

List of Symbols

The following list defines those variables and constants used most often in this study and not identified in context. For the state variables, density, pressure and temperature, and for accelerations and velocities, a zero subscript denotes "reference state," a subscript $\underline{t}$ denotes "total" and no subscript denotes "perturbation."

$p,\ \rho,\ T$	pressure, density and temperature
ρ_L	liquid-water content (grams of liquid water per unit volume of air)
$\underset{\rightarrow}{V},\ \dot{\underset{\rightarrow}{V}}$	three-dimensional velocity vector and total time derivative
$\underset{\rightarrow}{V}$	horizontal velocity vector
$\dot{u},\dot{v},\dot{w}$	acceleration components in x, y and z directions
L,M,N	maximum extent in length of the domain in x, y and z directions
$\nabla_H,\ \nabla_3$	two- and three-dimensional del operators
∇_3^2	three-dimensional Laplacian operator
δ_k	first order finite difference operator in z (or k) direction
δ_3^2	second order finite difference operator in all three coordinate directions
G	mesh or grid spacing except in Eq. (3.3) where it represents the radar antenna gain (38.1 db)
g	acceleration of gravity (980 cm/sec^2)
R	gas constant for dry air (2.87×10^6 ergs$\cdot$gm$^{-1}\cdot$deg^{-1})
$\bar{P}_r$	average power returned to radar antenna (see Table 1)
θ,ϕ	radar beam widths, horizontal and vertical measured to half-power points ($\theta = \phi = 2$ deg.)

h	radar beam pulse length (4 μsec)
P_T	radar peak power transmitted (450 Kw)
λ	radar wavelength (10 cm)

The Balance Equation

As discussed in Section 1, a scale analysis determines the proper form of the governing relationships. Coriolis forces are unimportant, and, for deep convection, the anelastic assumption applies. Further ignoring viscous forces and Reynolds' stresses but including a liquid-water drag term $\rho_L(z)g$, the three-dimensional, vector equation of motion may be written

$$\rho_t \dot{\underset{\to}{V}}_t = -\nabla_3 p_t - (\rho_t + \rho_L) g\hat{k} \;. \qquad (2.1)$$

Since the cloud and precipitation elements quickly reach a state of terminal fall, the downward drag force is equal to the weight of liquid water (see Arnason, et al., 1968; Ogura, 1963; and Takeda, 1965, 1966).

The dependent variables may be expressed as a sum of reference values and their much smaller perturbations (e.g., see Dutton and Fichtl, 1969). This may be expressed (for convenience, about a reference state of no motion) as

$$\begin{array}{lcll} \rho_t(x,y,z,t) & = & \rho_0(z) + \rho(x,y,z,t) & \rho/\rho_0 \ll 1 \\ p_t(x,y,z,t) & = & p_0(z) + p(x,y,z,t) & p/p_0 \ll 1 \\ \underset{\to}{V}_t(x,y,z,t) & = & \underset{\to}{V}(x,y,z,t) \;. & \end{array} \qquad (2.2)$$

Substituting Eqs. (2.2) into Eq. (2.1), allowing the approximation, $1 + \rho/\rho_0 = 1$ except in terms involving gravity (i.e., the Boussinesq approximation), and noting that a hydrostatic reference state implies $\nabla_3 p_0 = -\rho_0 g\hat{k}$, results in the disturbance equation

$$\rho_0 \dot{\underset{\to}{V}} = -\nabla_3 p - (\rho + \rho_L) g\hat{k} \;. \qquad (2.3)$$

Consistent with the anelastic approximation, the proper continuity of mass relationship is

$$\nabla_3 \cdot (\rho_0 \underset{\to}{V}) = \rho_0 \nabla_H \cdot V_H + \frac{\partial}{\partial z}(\rho_0 w) = 0 \;. \qquad (2.4)$$

Taking the scalar product of the operator and Eq. (2.3) simultaneously imposing the constraint represented by Eq. (2.4) results in a diagnostic equation for pressure, the anelastic balance equation:

$$\nabla_3 \cdot (\rho_0 \underset{\to}{V} \cdot \nabla_3 \underset{\to}{V}) + g\frac{\partial}{\partial z}(\rho + \rho_L) + \nabla_3^2 p = 0 \;. \qquad (2.5)$$

Rather than apply this equation in this form, it was found convenient to retain the <u>total</u> derivative of the velocity vector (note that $\nabla_3 \cdot \frac{\partial}{\partial t} \underset{\rightarrow}{V} \neq 0$), and eliminate it at a later phase in the development. Again applying the ∇_3 operator to Eq. (2.3), the result may be written

$$\rho_0 \nabla_3 \cdot \underset{\rightarrow}{V} + \dot{w} \frac{\partial \rho_0}{\partial z} = -\nabla_3^2 p - q \frac{\partial}{\partial z}(\rho + \rho_L) \tag{2.6}$$

where the vertical equation of motion

$$\dot{w} = -\frac{1}{\rho_0}\frac{\partial p}{\partial z} - \frac{g}{\rho_0}(\rho + \rho_L) \tag{2.7}$$

is obtained by dotting Eq. (2.3) by the vertical unit vector k. Perturbations in density may be expressed in terms of temperature and pressure perturbations through the linearized equation of state,

$$\rho = \rho_0 \left(\frac{p}{p_0} - \frac{T}{T_0}\right) . \tag{2.8}$$

Performing the indicated substitutions, collecting like terms and rearranging yields

$$-\nabla_3^2 p + \frac{1}{\rho_0}\frac{\partial \rho_0}{\partial z}\frac{\partial p}{\partial z} - \rho_0 g \frac{\partial}{\partial z}\left(\frac{p}{p_0}\right) = -\rho_0 g \frac{\partial}{\partial z}\left(\frac{T}{T_0}\right) + \rho_0 g \frac{\partial}{\partial z}\left(\frac{\rho_L}{\rho_0}\right) + \rho_0 \nabla_3 \cdot \underset{\rightarrow}{\dot{V}} . \tag{2.9}$$

Equation (2.9) is the desired equation. It is, for pressure, a linear, second-order, nonhomogeneous, elliptic partial differential equation with variable coefficients. Thus, each of the terms on the right-hand side may serve independently as diagnostic "forcing functions" for instantaneous pressure. Only the drag term will be retained in the numerical phase of this study.

Before proceeding, it is instructive to consider the similarity in form between the first term (gradient of thermal buoyancy) and the second term (gradient of liquid-water drag) on the right-hand side of Eq. (2.9). To investigate their relative magnitudes, let $T = 3$ deg. K, $T_0 = 300$ deg. K, $\rho_L = 3$ gm/m^3, and $\rho_0 = 1000$ gm/m^3 be typical values found in a well-developed convective cloud at low levels. Then the ratio of accelerations due to drag over thermal buoyancy is of the order of 30%. Significantly, though, while T_0 in an extreme case may vary as much as 100 deg. K over the depth of the cloud, ρ_0 may vary routinely by as much as six or seven times T. If, for example, at the top of the cloud (say 200 mg.) the reasonable values of $\rho_L = 0.3$ gm/m^3, $T = 0.2$ deg. K, $T_0 = 220$ deg. K, and $\rho_0 = 300$ gm/m^3 are selected, then the ratio of the two terms approaches 100%. But, although the drag force (always negative) and the thermal buoyancy are generally opposed in sign in the generating part of the updraft and may augment each other in downdrafts, order-of-magnitude arguments of this sort are not very useful in predicting areas of significant flow. It will be seen in Section 4 that pressure forces must also be taken into account.

Equation (2.9) may be further simplified if we focus just upon the influence of the drag term. Let us assume that $\nabla_3 \cdot \frac{\partial}{\partial t}(\underset{\rightarrow}{V}) = 0$ and ignore the thermal buoyancy and inertial terms. Then performing the indicated operation on the second pressure term (pressure buoyancy) and selecting the standard substitutions, scale height $H = RT_0/g$, lapse rates: autoconvective, $\gamma_A = g/R$, and reference state, $\gamma_0 = -\frac{\partial T_0}{\partial z}$, letting $\Gamma = \gamma_0/\gamma_A$, Eq. (2.9) becomes

$$H\nabla_3^2 p + (2-\Gamma)\frac{\partial p}{\partial z} + \frac{1}{H}\,p = -p_0\frac{\partial}{\partial z}\left(\frac{\rho_L}{\rho_0}\right) . \tag{2.10}$$

With proper boundary conditions on p and the forcing term involving ρ_L specified, Eq. (2.10) may be solved for pressure. From Eq. (2.3), it is seen that the proper boundary conditions are

$$x = 0,L\colon\ \dot{u} = 0;\quad \frac{\partial p}{\partial x} = 0$$

$$y = 0,M\colon\ \dot{v} = 0;\quad \frac{\partial p}{\partial y} = 0$$

$$z = 0,N\colon\ \dot{w} = 0;\quad \frac{\partial p}{\partial z} = -\frac{p}{H} - \rho_L g \ . \tag{2.11}$$

The first two conditions are statements that the model results should be influenced only by internal forcing. The third condition corresponds to hydrostatic balance at a rigid, flat earth surface.

Numerical Technique

The finite difference approximation to Eq. (2.10) may be written

$$\left(\frac{2H}{G}\right)_k \delta_3^2 p + (2-\Gamma)_k \delta_k p + \left(\frac{2G}{H}\right)_k p + (p_0)_k \delta_k\left(\frac{\rho_L}{\rho_0}\right) = 0 \tag{2.12}$$

where the subscript k indicates functional dependence in the vertical coordinate. The equation has been solved by the well-known, numerical method of sequential overrelaxation. This relatively uncomplicated application is particularly well adapted for elliptic partial differential equations being approximated over a large domain. Briefly, it is an iterative process where the object is to reduce "residuals," that is to say, excesses above a specified tolerance at all grid points in the domain of computation. The specified tolerance would be ideally zero, in fact, the same zero of Eq. (2.12) but, in practice, it is a small finite value. Progressively smaller residuals are generated iteratively at all points in the mesh (here, three-dimensional) through improved estimates of the solution values obtained by successive corrections.

Let R^m be the residual for an arbitrary point in the mesh at the mth iteration, p^m the corresponding value of p at the same point, and p_n^m and p_n^{m+1} current values of p at neighboring points for either the mth or m+1st iteration (see Figure 1). Equation (2.12) is then modified to

$$S_1(p_1^m+p_2^m+p_3^{m+1}+p_4^{m+1}) + (S_1+S_2)p_5^m + (S_1-S_2)p_6^{m+1} + S_3p^m$$

$$+ (p_0)_k\delta_k\left(\frac{\rho_L}{\rho_0}\right) = R^m \qquad (2.13)$$

where

$$S_1 = \frac{2H}{G}\ ; \quad S_2 = 2 - \Gamma, \quad S_3 = \frac{2}{S_1} - 6S_1 \quad .$$

If, at a successive iteration, p^m is changed to p^{m+1} without adjustment in the surrounding p_n, apparently

$$S_3(p^{m+1} - p^m) = \omega(R^{m+1} - R^m), \qquad (2.14)$$

where ω, the so-called relaxation factor, has been introduced and is optimally, in magnitude, somewhere between 1 and 2. (If $\omega < 1$, then the process is termed underrelaxation.) The best value for p^{m+1} would result if $R^{m+1} = 0$; hence

$$p^{m+1} = p^m - \frac{\omega}{S_3}R^m \ . \qquad (2.15)$$

In practice, the mesh is swept in some organized fashion (by rows, columns, spiral, etc.); a residual is calculated from Eq. (2.14) and thus a new solution value using Eq. (2.15) is obtained at each grid point. The process is repeated until all residuals are reduced below the specified tolerance and, thus, a final "converged" solution value appears at every grid point. The specified tolerance for the residual, R^m, in this case, was 0.01 mb. which produced a maximum of about 4×10^{-4} mb. between the final two successive values of pressure. Figure 1 schematizes any one successive star in the mesh; subscripts and superscripts are consistent with Eqs. (2.13) and (2.14). The order of computation proceeded through the mesh from top to bottom and, at each level, first in the positive j direction and then in the positive i direction.

It can be shown that an elliptic equation of the form being considered here will always converge to a solution if the appropriate boundary conditions are specified. These conditions are either the value of the function's normal derivative (Neumann) or the value of the function itself (Dirichlet). The boundary conditions, Eqs. (2.11), are Neumann on the lateral boundaries but of a different sort on the upper and lower boundaries. The condition, physically signifying hydrostatic balance, is mathematically termed "mixed." This boundary condition itself is a nonhomogeneous form if $\rho_L \neq 0$ at the surface.

The mixed-Neumann conditions constitute a problem in application when coupled with the numerical technique described above. It

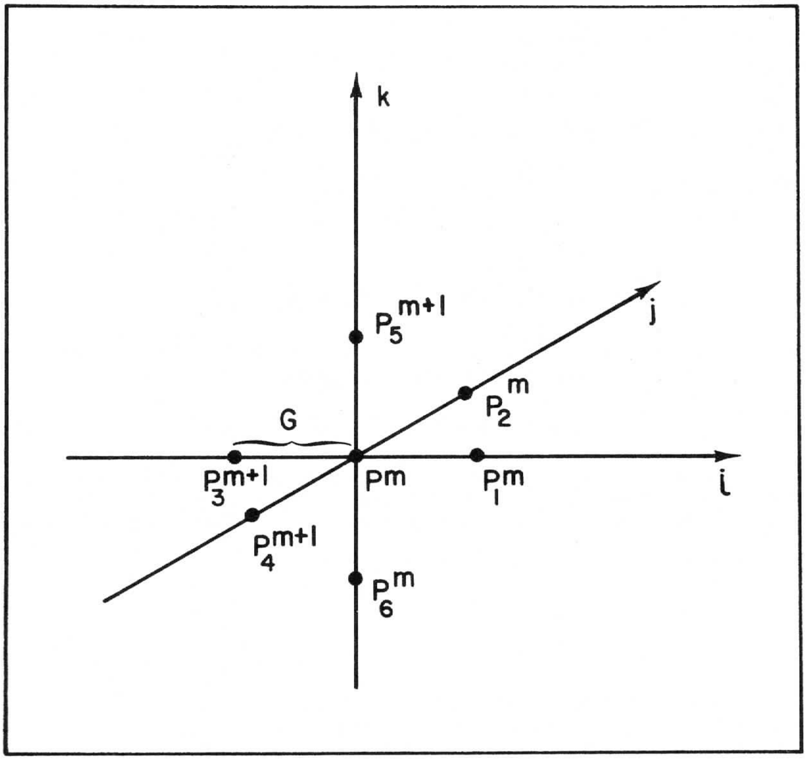

Figure 1. One star in the finite-difference mesh. The i (north-south), j (east-west), and k (vertical) coordinate directions are positive in the direction of the arrows. Subscripts and superscripts are consistent with Eq. (2.10). G is the mesh increment (equal to 1 n. mile).

is not clear, for example, whether a centered difference approximation to the boundary conditions should be substituted in Eq. (2.13) at each boundary point encountered during successive sweeps through the mesh (i.e., relaxation on the boundaries), or Eq. (2.13) should be applied only in the interior of the mesh with a combination of forward and backward difference approximations made at the boundaries. In the latter case, it must be decided when during the iterative process to apply the boundary constraint: uniformly before each sweep through the grid or before and after calculation of each adjacent interior point.

The Dirichlet condition, however, appears more attractive. For then it is necessary only to determine the boundary values of the function itself which would remain constant for the entire iterative process. Fewer iterations for convergence would be an additional benefit. For the physical problem under consideration here, the pressure-perturbation response may be realistically considered zero at a sufficiently large distance from the cloud which is the origin of the forcing-function disturbance.

As a consequence of the above considerations, Dirichlet boundary conditions were adopted on all boundaries except the rigid, lower boundary. In order to simultaneously insure available core storage in the Univac 1108 and provide an adequate volume into which values would naturally damp to zero, a further embellishment proved necessary. The restraints were satisfied by first seeking a solution on a coarse grid including the original data domain. Figure 2 demonstrates schematically the geometry in a cross-sectional view of the three-dimensional domain. The shaded area depicts the region containing nonzero values of the forcing-function; this "fine mesh" was in turn embedded within the "coarse mesh." The boundary values were as indicated in the figure; the hydrostatic relationship in finite difference form is

$$p_B = \frac{H_B(p_{B+1} + \rho_L gG)}{H_B - G} \tag{2.16}$$

where the subscripts B and B + 1 denote, respectively, boundary values and contiguous interior values in a normal direction. Equation (2.16), a forward difference, was applied after each iteration.

Given a first fully converged field throughout the coarse mesh, the iterative scheme was reapplied to the fine mesh using as a first approximation a combination of the coarse mesh solution and linearly interpolated values to fill out the additional points. The top and lateral boundary values for the fine mesh thus determined were held constant during subsequent iterations. Once the pressure field was secured, the individual forces on the right side of Eq. (2.7) were computed and added to produce a field of net vertical accelerations.

In order to apply the above numerical scheme, values of the forcing function are required. This involves determining a spatial distribution for LWC. This is the topic of the next section, which includes a discussion of solution nonuniqueness.

3. Data Processing

The Forcing Function

A practicably elegant, albeit theoretically cumbersome, procedure to determine LWC distributions involves first obtaining quantitative values of radar echo returns. The implied conversion is made by assuming or measuring independently a reflecting particle distribution. Because these types of conversion mechanisms have been displayed and reviewed extensively by many radar meteorologists, the development which follows excludes detailed discussion of the

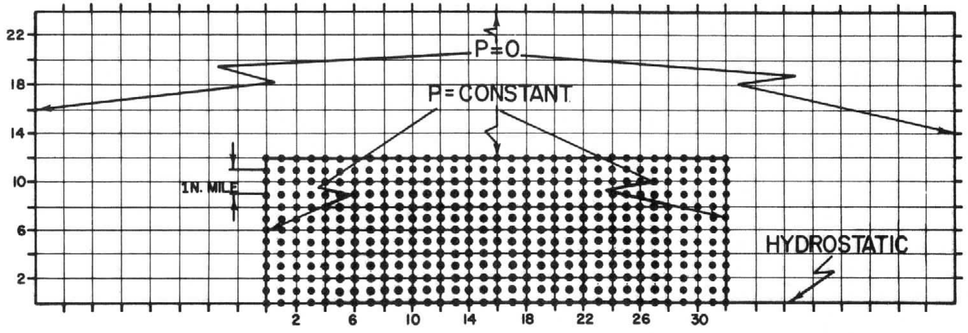

Figure 2. Cross-sectional view of the three-dimensional, finite-difference mesh. The view is north-south where north is on the right side of the figure. Every intersection of grid lines corresponds to a data point in the coarse mesh. Dots indicate the additional data points present in the fine mesh. Shading depicts the area outside of which no nonzero forcing values (LWC) appeared. Boundary conditions are as indicated. (Note: the fine mesh lateral boundary condition is constant only for the numerical relaxation of the fine mesh.)

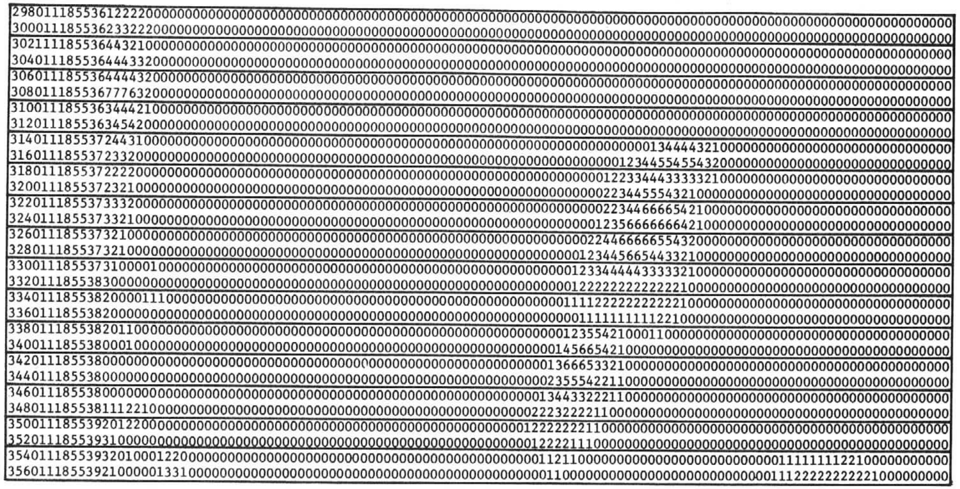

```
29801118553612222000000000000000000000000000000000000000000000000000000000000000000000000000000000000000000000000000000000
300011185536233222000000000000000000000000000000000000000000000000000000000000000000000000000000000000000000000000000000000
30211118553644321000000000000000000000000000000000000000000000000000000000000000000000000000000000000000000000000000000000
304011185536444332000000000000000000000000000000000000000000000000000000000000000000000000000000000000000000000000000000000
306011185536444432000000000000000000000000000000000000000000000000000000000000000000000000000000000000000000000000000000000
308011185536777632000000000000000000000000000000000000000000000000000000000000000000000000000000000000000000000000000000000
310011185536344421000000000000000000000000000000000000000000000000000000000000000000000000000000000000000000000000000000000
31201118553634542000000000000000000000000000000000000000000000000000000000000000000000000000000000000000000000000000000000
31401118553724431000000000000000000000000000000000000000000000000000000000000000000000134444321000000000000000000000000000000
31601118553723320000000000000000000000000000000000000000000000000001234455455432000000000000000000000000000000
31801118553722220000000000000000000000000000000000000000000000000122334443333321000000000000000000000000000000
32001118553723210000000000000000000000000000000000000000000000000223445554321000000000000000000000000000000000
32201118553733320000000000000000000000000000000000000000000000000223446666542100000000000000000000000000000000
32401118553733210000000000000000000000000000000000000000000000001235666666642100000000000000000000000000000000
32601118553732100000000000000000000000000000000000000000000000002244666665543200000000000000000000000000000000
32801118553732100000000000000000000000000000000000000000000000012344566544332100000000000000000000000000000000
33001118553731000010000000000000000000000000000000000000000000012334444433333210000000000000000000000000000000
33201118553830000000000000000000000000000000000000000000000000012222222222222100000000000000000000000000000000
33401118553820000111000000000000000000000000000000000000000000111122222222222100000000000000000000000000000000
33601118553820000000000000000000000000000000000000000000000000011111111112210000000000000000000000000000000000
33801118553820110000000000000000000000000000000000000000000012355421000110000000000000000000000000000000000000
34001118553800010000000000000000000000000000000000000000000145665421000000000000000000000000000000000000000000
34201118553800000000000000000000000000000000000000000000001366653321000000000000000000000000000000000000000000
34401118553800000000000000000000000000000000000000000000002355542211000000000000000000000000000000000000000000
34601118553800000000000000000000000000000000000000000000013443322211000000000000000000000000000000000000000000
34801118553811122100000000000000000000000000000000000000002223222211000000000000000000000000000000000000000000
35001118553920122000000000000000000000000000000000000000001222222211000000000000000000000000000000000000000000
35201118553931000000000000000000000000000000000000000000001222211100000000000000000000000000000000000000000000
35401118553932010001220000000000000000000000000000000000000112110000000000000000000000000011111111221000000000000
35601118553921000001331000000000000000000000000000000000000011000000000000000000000000000111222222222210000000000
```

Figure 3. Reproduced sample of digitized radar data provided by the National Severe Storms Laboratory (NSSL), Norman, Oklahoma. The data are in B-scan (azimuth vs. altitude) format. Each column represents 1 n. mile in slant range beginning with the thirteenth column (which corresponds, in this case, with the thirteenth n. mile), and each line represents two degrees of azimuth (both measured with respect to the radar antenna. The first twelve columns indicate: azimuth (three digits); elevation (two digits); a range normalization indicator (one digit); and time (CST) in hours, minutes, and seconds (six digits). Numbers in the data field correspond to echo intensities where zero indicates no echo.

more common assumptions inherent in the analysis. For references pertinent to these assumptions (not specifically included in context), Atlas (1963, 1964), Batton (1959), Mason (1971), and Wilk and Kessler (1970) together provide a comprehensive view in textbook or monograph form.

For some years, the National Severe Storms Laboratory (NSSL) has conducted an ambitious program in weather radar data aquisition at Norman, Oklahoma. Using the WSR-57, averaged echo intensities of convective activity have been converted through a system of analogue and digital circuitry to digitized form. Figure 3 is a reproduced sample of the digitized data. It represents an approximately north-through-northwest segment of the PPI scope in B-scan (slant range, azimuth) format. Each line represents 2° of azimuth and each column 1 n. mile in slant range beginning with the 13th column which marks the first sampling gate after the delay (in this case, 13 n. miles). The data values are represented by a single digit which symbolizes an "echo contour" level, in turn uniquely identified with a calibrated echo intensity. Each B-scan corresponds to one of five levels (antenna tilt angles) of digitized data used in the analysis which follows. For a complete description of the NSSL Weather Radar Data System, see Wilk and Kessler (1970).

The numerical scheme outlined in Section 2 is most simply executed in a Cartesian coordinate system. Also, results are most graphically illustrated in a linear reference frame. For these reasons and because the digitized data were in essentially spherical coordinates, the following familiar transformation was employed:

$$\begin{aligned} &\text{north-south:} \quad && y = R \sin\theta \cos\phi \\ &\text{east-west:} \quad && x = R \sin\theta \sin\phi \\ &\text{altitude:} \quad && z = R \cos\theta \end{aligned} \tag{3.1}$$

where, in this particular case

$\theta = 90-\Theta; \quad \phi = 360-\Phi$

Θ = antenna tilt = 0,1,2,4,6 degrees

Φ = antenna azimuth = 2,0,358,356,... 312 degrees

R = slant range = 65,66,67,... 94 n. miles

No correction was made for the curvature of the radar beam (due to refraction). This procedure is consistent with the successively larger atmospheric volumes sampled by the radar beam at 1 n. mile increments. The nearest nonzero values recorded by the radar were averaged across a beam width of approximately 2 n. miles. The farthest sampled volume occurred where the beam width was about 3 n. miles. Therefore, data values were slightly readjusted in space and vacant data points occurred in the transformed mesh. A linear interpolation provided the missing values and established a resolution of 1 n. mile in all three transformed coordinate directions. Because the objective was to expediently provide a representative distribution, these simplifying procedures were of little consequence unless the radar beam had suffered significant variable refraction. The magnitude of this effect is, by and large, unpredictable. The original data, in any case, indicated neither anomalous propagation nor interference of any kind.

Concurrently with the coordinate transformations, the contour values were converted to values of the equivalent (i.e., measured) reflectivity factor Z_e . To apply Rayleigh scattering principles, Z_e is commonly identified with Z, defined by

$$Z = \sum_{\text{vol.}} D^6 \ . \tag{3.2}$$

The echo intensity or average power returned to the radar antenna and the reflectivity factor are related through the radar equation. The form of the equation selected here was derived by Probert-Jones (1962). It is

$$\bar{P}_r = \left(\frac{\pi^3 \theta \phi h G^2 |K|^2 P_T}{1024 \ln 2 \lambda^2 R_n^2} \right) Z \ . \tag{3.3}$$

The dimensionless factor K is a function of the reflecting particles' complex index of refraction. For liquid water, $|K|^2 = 0.930$ and for ice, $|K|^2 = 0.197$ to close approximation. For an ice-water mixture, the value is unknown, a subject of continuing research. However, Kerker et al. (1951) have shown that an ice sphere surrounded by a water film greater than one-fifth its original radius will scatter radar energy the same as a water sphere of the same mass. Further considerations (shape, quality of the ice, etc.) introduce complications beyond the scope of this study. Reasonable results for this study were obtained by simply adopting the liquid-water value. Equation (3.3) may now be written

$$\bar{P}_r = cZ \tag{3.4}$$

where c is a constant peculiar to a particular radar set for which the signal has been range-normalized ($R_n = 100$ n. miles for the data). Substituting the radar parameters and making the appropriate units conversions yielded a value for c of approximately 3.26×10^{-15} $m^3 \cdot$ watt/mm^6. Thus, if each P identified with a contour level is substituted in Eq. (3.4), a reflectivity factor is also identified with that contour level.

A number of assumptions inherent in Eqs. (3.2), (3.3), and (3.4) should be noted. Equation (3.2) is a derivative of the well known Rayleigh scattering law. For target particles whose diameters are $\gtrsim$ 4 mm. to 6 mm. (for a radar wavelength, $\lambda = 10$ cm), the more precise and considerably more mathematically cumbersome Mie scattering theory should be used. Ignoring the possibility of large graupel and the like, and since the typical raindrop is about 1 mm in diameter (tending to become unstable and break up into smaller fragments at about 5 mm), the Rayleigh assumption appears reasonable if hail is not present. The possibility of hail is discussed later.

Equation (3.3) contains the usual uncertainties characteristic of its kind. They are predominantly: 1) energy losses due to scattering or absorption between radar and target, 2) attenuation of the signal, 3) the effects of the particles within the beam not uniformly illuminated, and 4) the beam not filled with scattering particles. A discussion of the first and third sources of error are beyond the scope of this study; they did not noticeably affect the resultant LWC fields. Signal attenuation is apparently small for 10 cm radar; it was also ignored. The problem of non-beam filling becomes significant in determining echo tops. The familiar "rule-of-thumb," subtraction of half the beam width, has been shown in one study to overcorrect actual cloud tops. The overcorrection, however, is less than the maximum 1 n. mile resolution in the NSSL data. Applying the rule-of-thumb correction produced cloud-top altitudes in close agreement with the tropopause level of the reference atmosphere (presented in the next subsection).

Equation (3.2) may be expressed in a more mathematically tractable form. An integration is suggested, viz:

$$Z = \int_0^{D_n} N(D)\,dD \tag{3.5}$$

where $N = N(D)$ is the number density. A common approach establishing an expression for N is to employ the Marshall-Palmer (1948) exponential expression

$$N = N_0 e^{-\Lambda D} \tag{3.6}$$

where now N is the number of drops of diameter D per unit volume of air in the interval ΔD, N_0 is the number of drops at zero size, and is a parameter to be determined. Equation (3.6) fits most drop-size distributions in stratiform rain and closely approximates showery rain overestimating rain drops $\gtrsim 5$ mm. and those $\lesssim 1$ mm. Following Kessler (1969), substitution of Eq. (3.1) into Eq. (3.5) and integration by parts over all diameters yields

$$Z = \int_0^{\infty} N_0 e^{-\Lambda D} D^6 dD = N_0 \Lambda^{-7} 6! \tag{3.7}$$

The two ends of the drop spectrum then contribute only about 15% of the total magnitude of Z, within the error of most estimates of Z (Wilk and Kessler, 1970). To eliminate Λ a similar integration for the LWC yields

$$\rho_L = \int_0^{\infty} \frac{\pi \rho_\ell}{6} D^3 N_0 e^{-\Lambda D} dD = \pi \rho_\ell N_0 \Lambda^{-4} \tag{3.8}$$

where the density of water, $\rho_\ell = 10^6$ gm/m^3. A widely-accepted value for N_0 is 10^{-7} m^{-4} . See Simpson and Wiggert (1969) for a discussion of this last parameter. Combining Eqs. (3.7) and (3.8), substituting in the appropriate values, and making a units adjustment so that Z is expressed in mm^6/m^3 determines the simple expression

$$Z = c\rho_L^{7/4} \qquad (3.9)$$

where c is treated as a proportionality constant approximately equal to 1.73×10^4 mm^6 $gm^{-7/4}$ $m^{9/4}$.

Equipped with Eqs. (3.4) and (3.9), along with the coordinate transformations (3.1), a three-dimensional distribution of LWC was determined in a cartesian frame. No allowance for hail was made in the conversion. Table 1 is a summary of the results. The largest value for ρ_L was 3.98 gm/m^3 corresponding to a log Z value of 5.3. These values all occurred at the lowest level in the cloud area; they are large but not unlikely values for LWC in a cumulonimbus, and contributed to less than 0.1% of the total volume sampled. Moreover, while there is no universally accepted critical value of log Z above which hail is definitely identified, values from about 5.0 to 5.5 for 10 cm radar appear in various sources. Atlas (1963) has provided a summary. In view of the above and consistent with the previously defined objective, "no hail" was a reasonable assumption.

Table 1

Summary of Results of Conversion
from Radar Echo Values to LWC Values

Contour Level	Power Level (DBM)	Reflect Factor, Z (mm^6/m^3)	Log (Z)	LWC (gm/m^3)
1	-98.0	48.7	1.69	0.035
2	-94.0	122	2.09	0.059
3	-84.0	1.22×10^3	3.09	0.220
4	-78.0	4.87×10^3	3.69	0.485
5	-70.0	3.07×10^4	4.49	1.39
6	-67.0	6.13×10^4	4.79	2.06
7	-62.0	1.94×10^5	5.29	3.98

The final distributions consisted of a three-dimensional mesh (the intersections of which were equally spaced at 1 n. mile intervals), 10 levels in altitude (thus, the highest cloud top was 9 n. miles), 25 slabs in the north-south direction, and 73 slabs in the east-west direction. Figures 4 through 7 show the results for five selected levels (plan view), two north-south slabs, and one east-west slab. The slabs selected are indicated in the lowest plan view, Figure 4. In all cases, the cloud boundary (heavy, unlabeled line) is the delineator outside of which all values less than 0.02 gm/m were arbitrarily set to zero. The various views taken as a whole reveal a domain consisting of most conspicuously two isolated storm cells, the larger of which shows evidence of "spawning" two smaller cells. Most importantly, the three-dimensional, asymmetrical character of the implied convection is striking and cannot be repre-

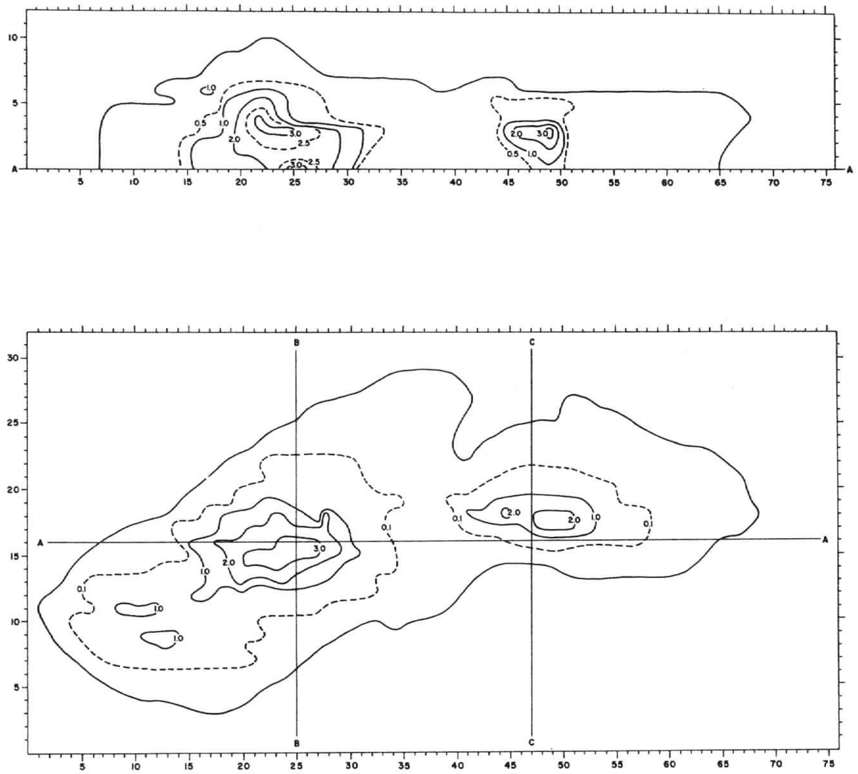

Figure 4. (top) East-west, vertical cross-section of LWC in the storm system. The left side of the figure is west, and both scales are incremented in nautical miles. The line labeled AA is the same as the line labeled AA in the bottom panel of this figure. Solid and dashed curves are in units of grams of liquid water per kilogram of air. The outside solid curve (unlabeled) marks the cloud edge as defined in the text.

(bottom) Ground level plan view of LWC in the storm system. The top of the figure is north and both scales are incremented in nautical miles. The superimposed straight lines labeled AA, BB, and CC mark the cuts through which cross-sectional views are displayed in the top of this figure and the figures which follow. Solid and dashed curves are in units of liquid water per cubic meter. The solid outside curve marks the cloud boundary as defined in the text.

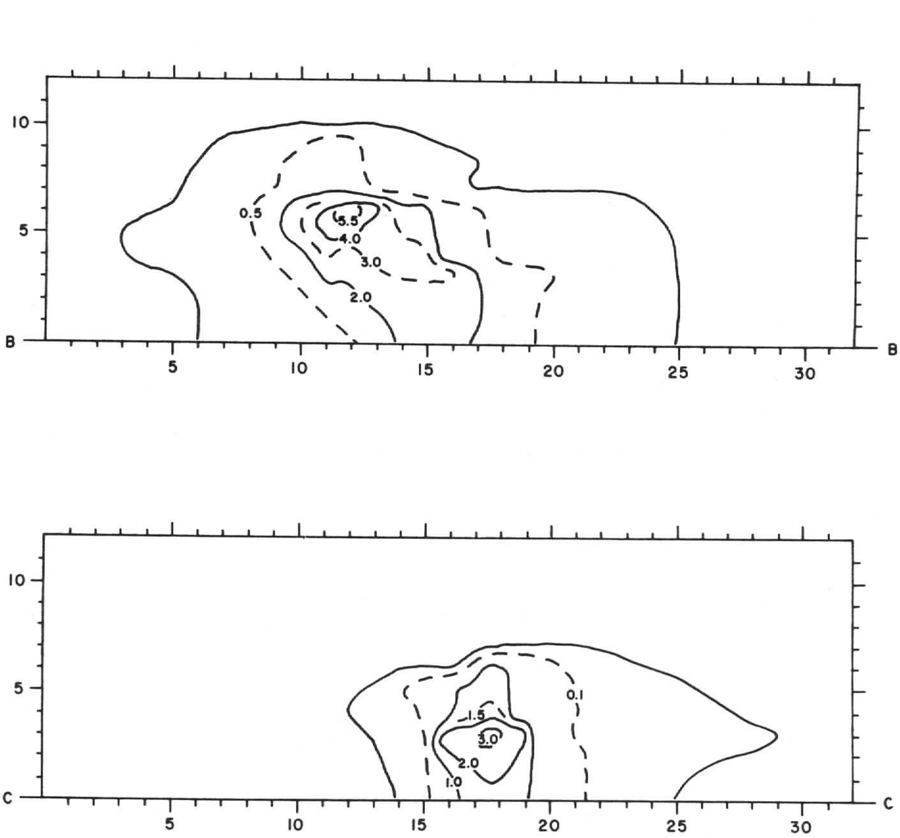

Figure 5. (top) North-south, vertical cross-section of LWC through CC (small cell). See Figure 4 (bottom). The right side of the figure is north. Cloud boundary and LWC units are the same as in the top panel of Figure 4.

(bottom) Same as top panel of this figure, except the view is through BB (large cell).

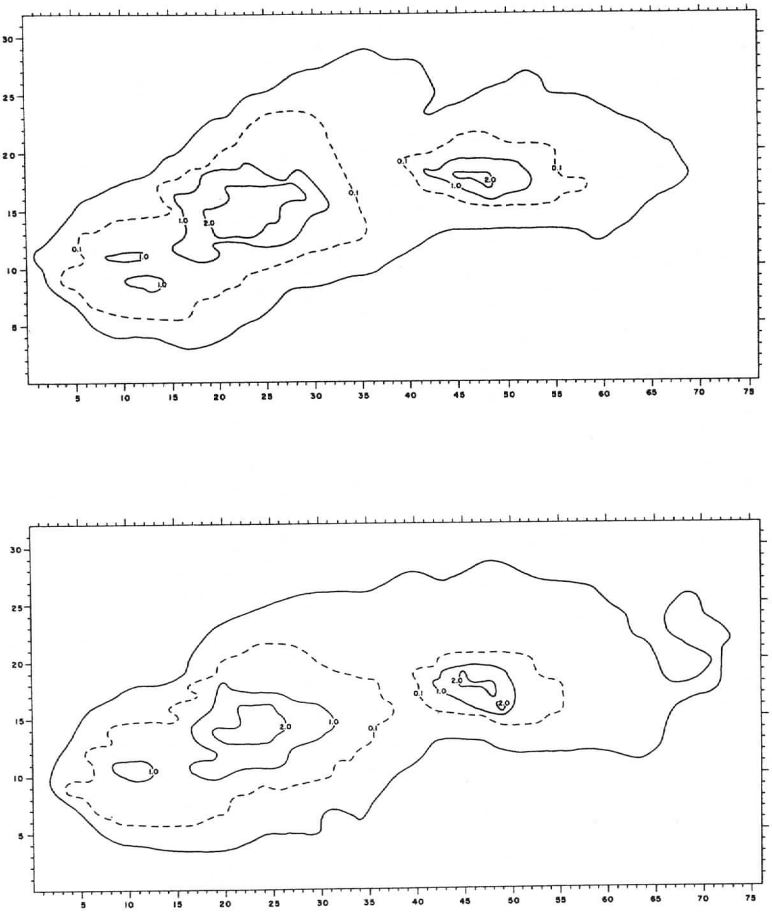

Figure 6. (top) Same as bottom panel of Figure 4, except the view is at 1 n. mile in altitude.

(bottom) Same as bottom panel of Figure 4, except the view is at 3 n. miles in altitude.

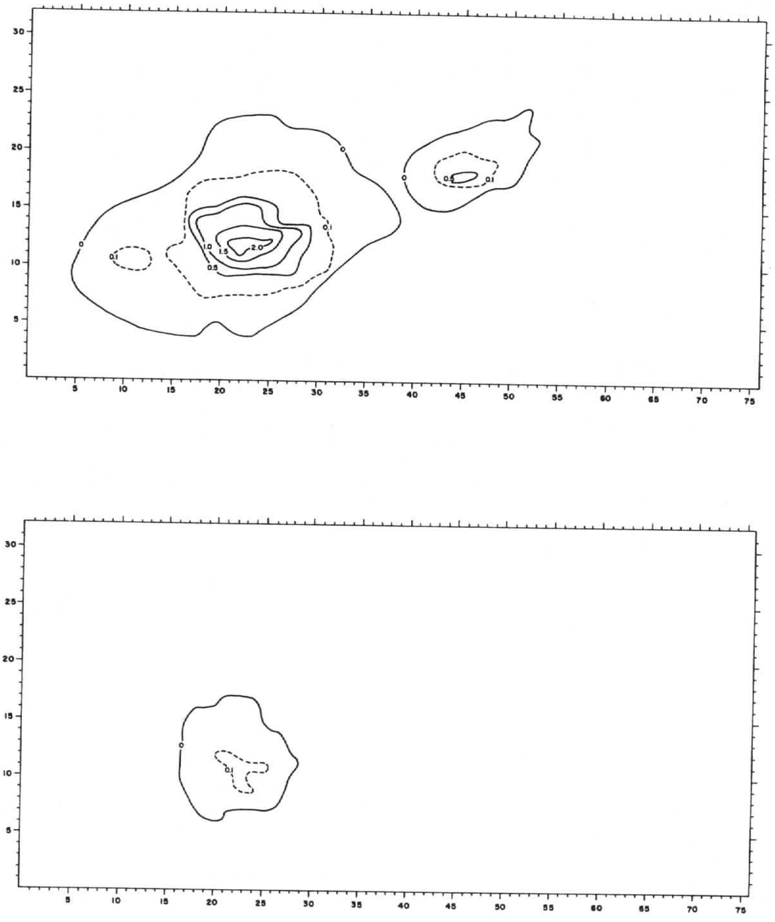

Figure 7. (top) Same as bottom panel of Figure 4, except the view is at 6 n. miles in altitude.

(bottom) Same as bottom panel of Figure 4, except the view is at 9 n. miles in altitude.

sented by a simple theoretical distribution containing only two scales of variation.

Notice that the plan views display isopleth spacings of one gram of liquid water per cubic meter of air whereas the vertical sections are analyzed in units of grams of liquid water per kilogram of air. This is convenient. The plan views thus demonstrate volumetric distributions. The slab views display, with a units adjustment, two additional distributions. By multiplying all values in the slab view fields by the negative of the acceleration of gravity ($\sim - 10^3$ cm/sec^2), the magnitudes of the mixing ratios of liquid water in grams to air in kilograms are approximately conserved and become measures of the drag force in cgs units.

Reference State Variables

To derive Eq. (2.9), the hydrostatic approximation was applied to the base, or reference state variables. Therefore, if a representative thermal stratification and ground-level pressure are known, the coefficients of Eq. (2.12) may be calculated. This could have been achieved somewhat arbitrarily but to close approximation by simply choosing reasonable values for surface temperature and pressure and applying any consistent set of formulas derived from a hydrostatic condition. One such set describes a "constant lapse-rate" atmosphere (Hess, 1959) in finite difference form:

$$(p_0)_k = (p_0)_{k-1}[(T_0)_k/(T_0)_{k-1}]^{\frac{1}{\Gamma}}; \quad H_k = \frac{(T_0)_k}{\gamma_A} = \frac{(T_0)_{k-1} - \gamma_0 G}{\gamma_A} \, . \tag{3.10}$$

Since radiosonde data were available for one hour preceding the time at which the radar data were obtained, a somewhat more accurate thermal stratification could be determined. The left graph of Figure 8 is a "smoothed" plot of the temperature soundings and selected wind barbs at Oklahoma City, Oklahoma and Dodge City, Kansas for 00Z, April 3, 1967. The storm area displayed in Figures 4 through 7 was located approximately midway between the two cities, south of and near the Oklahoma-Kansas border at approximately 01Z. It is seen that the implied tropopause occurs near 9 n. miles, agreeing closely with the radar derived, cloud-top value. The ambient flow is generally light from the southwest with no significant shear except in the lowest layers. The right graph of Figure 8 is a "fitted" curve to the plots in the left graph. The depicted lapse rates then were applied to the Eqs. (3.10). The ground pressure was taken at 1000 mb.

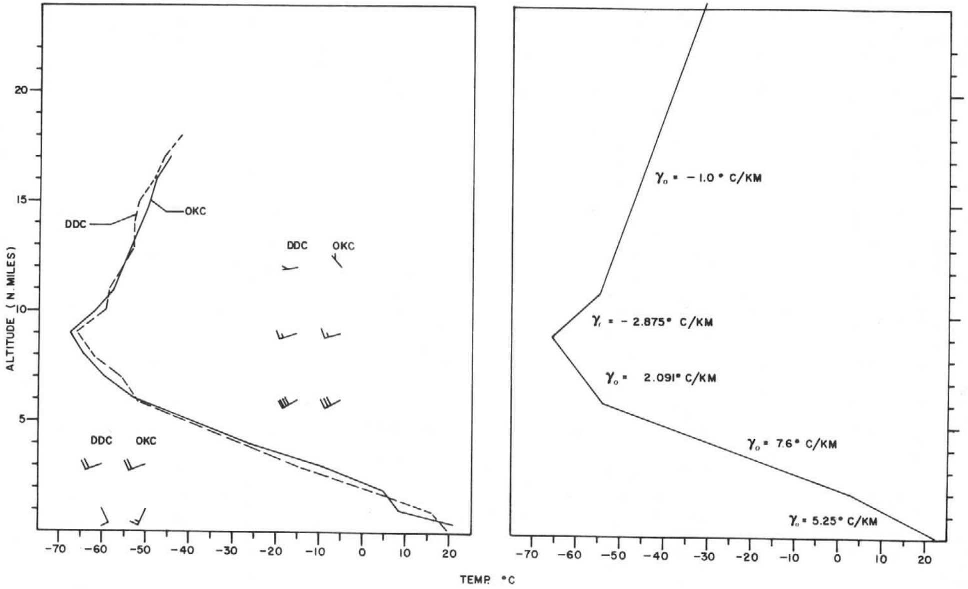

Figure 8. Temperature vs. altitude graphs for the reference state atmosphere. The graph on the left displays the temperature soundings for Oklahoma City, Oklahoma (OKC) and Dodge City, Kansas (DDC) at 00Z, April 3, 1967. Wind barbs of the ambient flow at selected altitudes are approximate. The graph on the right side is a fitted curve of the two temperature sounding curves. The resultant lapse rates are indicated in each layer.

4. Results

Discussion of the Solution

It was suggested in Section 2 that the solution to Eq. (2.9) may not be uniquely determined. While this is a disturbing consequence of the mathematical form of the equation, it does not render the results profitless. To examine some possible consequences of this problem, it is instructive to focus upon the vertical component of the equation of motion. The vertical component relates buoyancy, drag and the vertical pressure gradient force to the net vertical acceleration:

$$\dot{w} = -\frac{1}{\rho_0}\frac{\partial p}{\partial z} - \frac{p}{p_0}g - \frac{\rho_L}{\rho_0}g \quad . \qquad (4.1)$$

Equation (4.1) has been obtained by combining Eqs. (2.7) and (2.8) and then ignoring the thermal part of the buoyancy. The analogous properties of drag and thermal buoyancy were discussed in Section 2; the latter's elimination will not materially affect the following analysis. If the total disturbed pressure is defined as a summation of a hydrostatic part, $\hat{p}$ (defined for $w \equiv 0$) and a residual, non-hydrostatic (dynamic) part, p' ,

$$\hat{p} + p' = p \qquad (4.2)$$

so that

$$-\frac{1}{\rho_0}\frac{\partial \hat{p}}{\partial z} = \left(\frac{\hat{p}}{p_0} + \frac{\rho_L}{\rho_0}\right)g \qquad (4.3)$$

then substitution of Eq. (4.2) into Eq. (4.1) and subtracting out the balance represented by Eq. (4.3) yields

$$\dot{w} = \frac{1}{\rho_0}\frac{\partial p'}{\partial z} - \frac{p'}{p_0}g \quad . \qquad (4.4)$$

Equation (4.4) shows that the net vertical accelerations are equated with dynamical pressure forces. For a similar but somewhat different analysis, see List and Lozowski (1970).

The net vertical accelerations expressed in this manner, however, are useful. This can be seen by comparing them to the general solution of Eq. (4.3) which is

$$\hat{p} = \int -e^{-I} \int \rho_L g e^{I} dz + c e^{-I}, \quad I = \int \frac{1}{H}\, dz \sim \frac{z}{H} \qquad (4.5)$$

where c is an arbitrary constant of integration. The scale height, H, is a slowly varying function in the vertical, but for simplicity it will be treated as a constant in this demonstration. In terms of a boundary condition, say $\hat{p}(0) = p_B$, which determines $c = \hat{p}_B$, the term $\hat{p}_B e^{-I}$ approaches zero exponentially. Therefore, for any two solutions, their difference is dependent upon the difference in their boundary values multiplied by a transient (exponential damping), and is independent of the drag forcing (and also of thermal buoyancy). Apparently a solution to Eq. (2.9) also involves a transient, an adjunct of the hydrostatic character of the total solution. But after computation of the pertinent forces, the net vertical accelerations are unaffected.

Selected Numerical Results

In the following discussion, "perturbation pressure" will be referred to as simply "pressure" unless otherwise specified; also, accelerations will always mean <u>net</u> accelerations—again, unless otherwise specifically indicated.

Plan-view analyses of pressure and vertical accelerations are displayed in Figures 9 through 12. A quick comparison with Figures 5 and 6 clarifies the significance of the shaded areas. Thus, the darkest shading corresponds to a region of greatest liquid-water concentration. The lightest shading extends to the cloud boundaries, defined in Section 3. The four altitudes represented (one, three, six and nine nautical miles) correspond to reference pressure levels of approximately 800, 500, 225 and 100 millibars. Taken together, the four views reveal the three-dimensional intricacy to be expected of the dynamical structure associated with convection. It is clear that while the pressure surfaces are fairly smooth and centered about each of the prominent cells, the vertical accelerations similar to the pattern of LWC are highly irregular. This visual evidence agrees well with the contention that a very substantial contribution to the disturbance pressure is hydrostatic. It is not hard to demonstrate that the hydrostatic pressure is found on the largest horizontal scales, and that the pressure response is minimal on the smallest scales. Thus the net vertical accelerations result from largely uncompensated drag on small scales and partly nonhydrostatic drag on the larger scales, and tend to show greater horizontal detail than the LWC distribution would indicate. Thus we see important kinks in the isobars, most notably in relation to the smaller of the two prominent cells and in the "wake" of the larger one where, as pointed out in Section 3, two embryonic cells appear to be growing. Not surprisingly, the horizontal gradients of pressure (and, thus, horizontal accelerations) are strongest near where the vertical accelerations are also strongest.

Similar to the plan views, the vertical sections of Figures 13 through 15 should be compared to Figures 4 and 5. The shadings, however, may now be thought of as either LWC or drag forcing graduations. The three analyses of each figure are, from top to bottom, the vertical pressure gradient force, $-\frac{1}{\rho_0}\frac{\partial p}{\partial z}$, the pressure buoyancy force, $-\frac{p}{p_0}g$, and the net vertical acceleration, $\dot{w}$.

In general, the two pressure force vectors are, almost exclusively throughout the entire domain, opposed in direction. One intriguing exception to this rule occurs in the smaller cell (Figure 13) at a point located approximately 2 n. miles above the point of maximum drag forcing. The pressure buoyancy force changes sign from negative to positive just below the point in question and, for a depth of about 1 n. mile, augments the pressure gradient force in

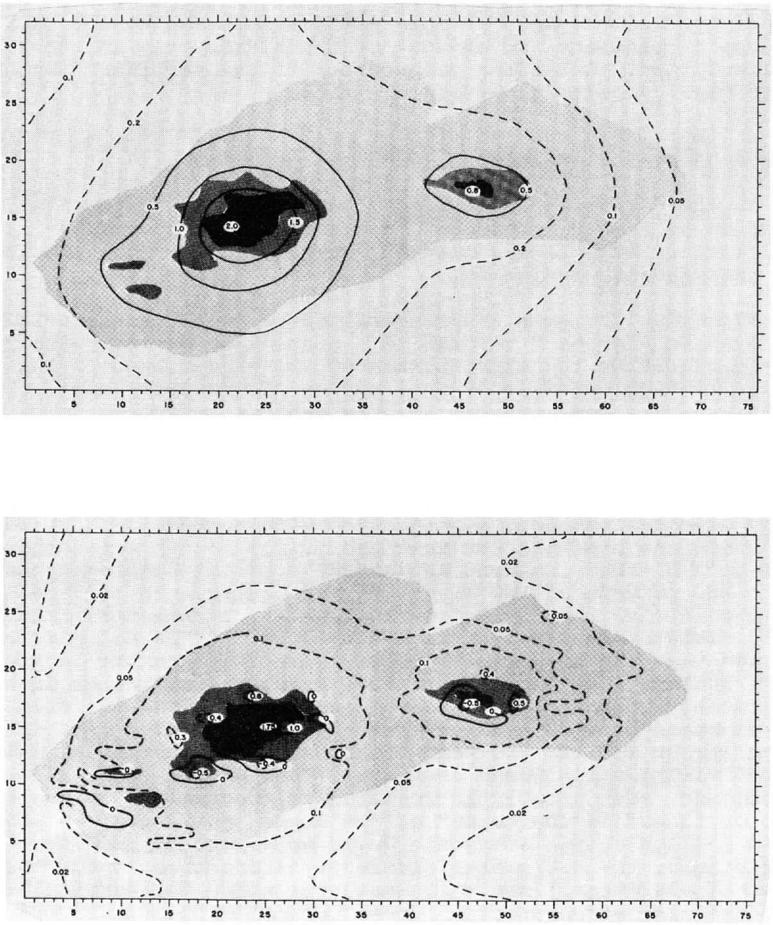

Figure 9. (top) Plan view of perturbation pressure at 1 n. mile in altitude. The top of the figure is north and the scales are incremented in nautical miles. Solid and dashed lines are perturbation isobars in millibars. The lightest shading determines the area outside of which there are no nonzero values of LWC (see Figure 4). The shading then becomes progressively darker, depicting increasing volumetric concentrations of LWC in increments of one gram.

(bottom) Plan view of net vertical acceleration at 1 n. mile in altitude. The view and LWC shading is the same as the top panel of this figure. Solid and dashed curves are incremented in units of cm/sec^2.

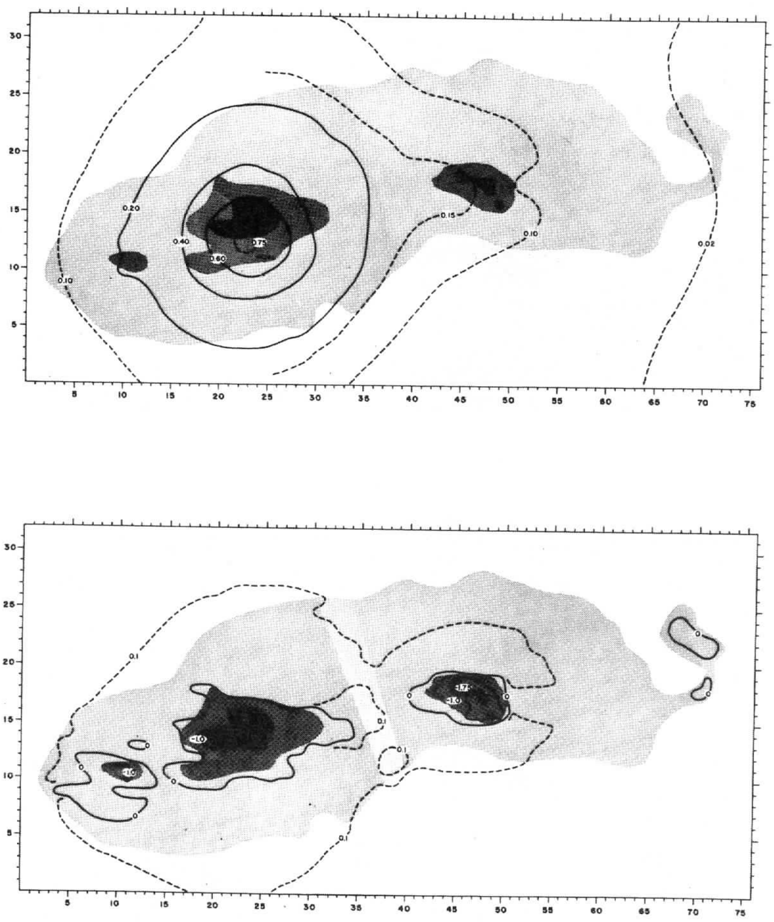

Figure 10. (top) Same as Figure 9 (top), except the view is at 3 n. miles.

(bottom) Same as Figure 9 (bottom), except the view is at 3 n. miles.

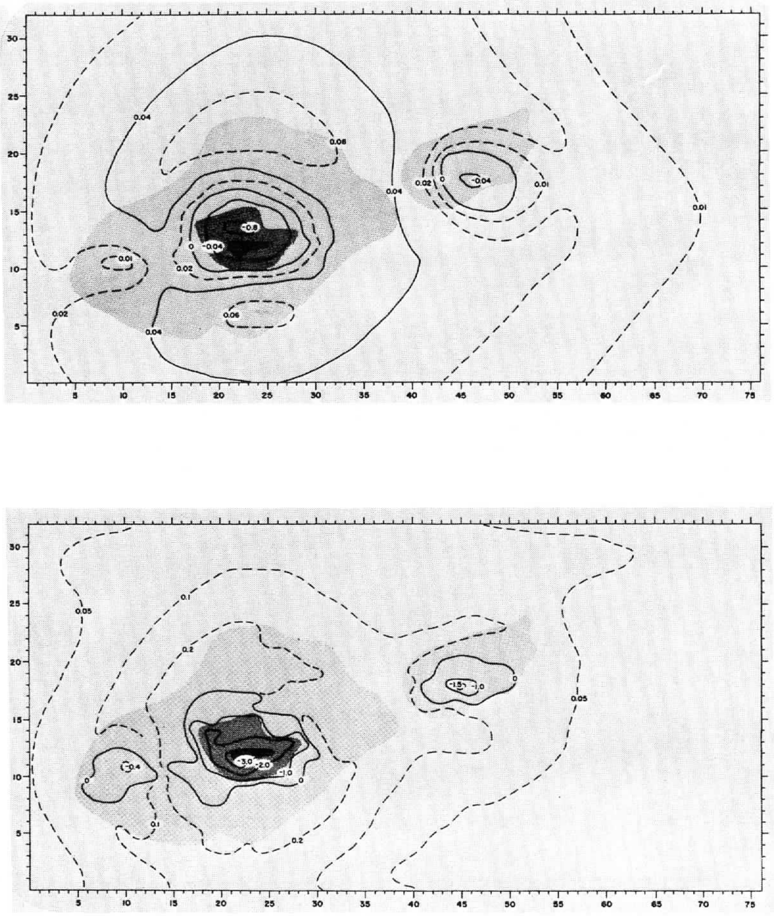

Figure 11. (top) Same as Figure 9 (top), except the view is at 6 n. miles.

(bottom) Same as Figure 9 (bottom), except the view is at 6 n. miles.

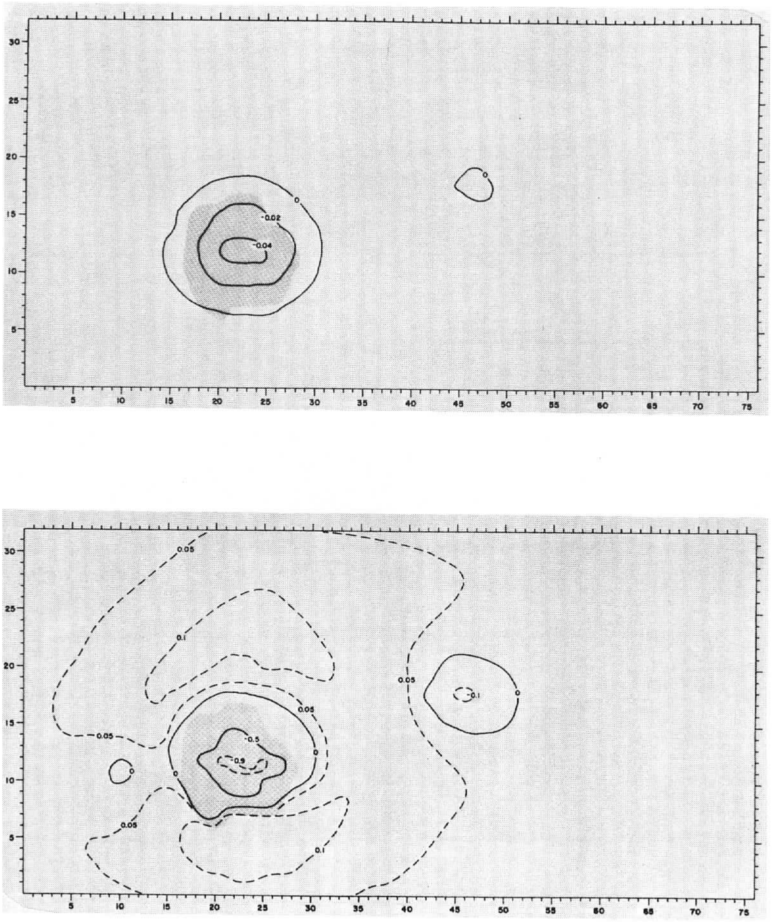

Figure 12. (top) Same as Figure 9 (top), except the view is at 9 n. miles.

(bottom) Same as Figure 9 (bottom), except the view is at 9 n. miles.

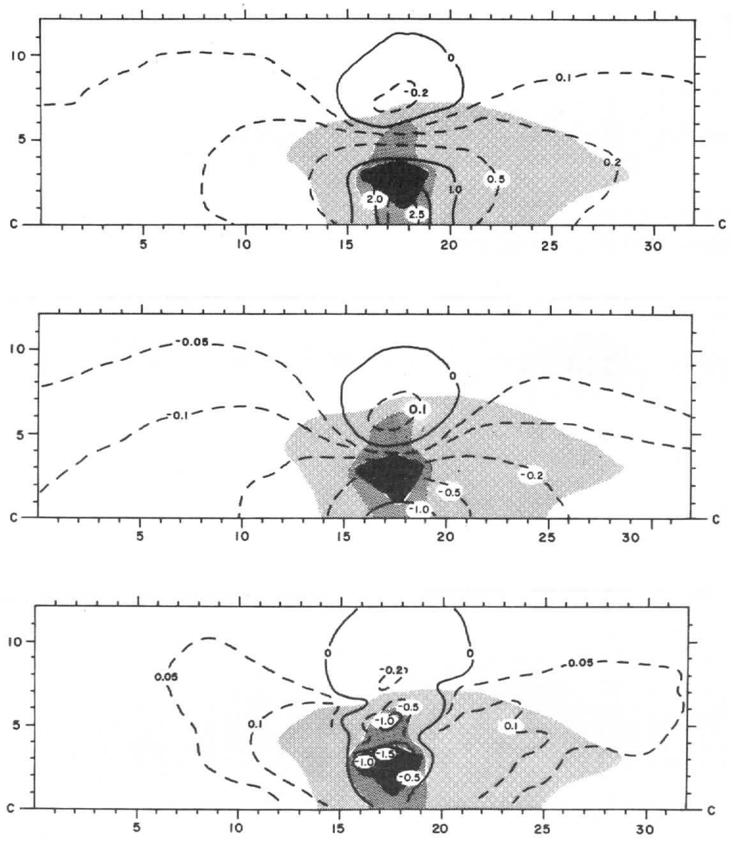

Figure 13. (top) North-south vertical cross-section through CC (small cell) of the vertical (disturbed) pressure gradient force. The right side of the figure is north and the scales are incremented in nautical miles. The shading from lightest to darkest corresponds to progressively greater concentrations of LWC in grams of liquid water per kilogram of air, or approximately, values of progressively greater drag forcing in units of dynes per gram. The values progress in increments of one unit for successively darker shades. Solid and dashed lines are force lines in units of dynes per gram or, equivalently, cm/sec^2.

(middle) Same as top panel of this diagram, except the analysis is of the (disturbed) pressure buoyancy force.

(bottom) Same as the top panel, except the analysis is of the net vertical acceleration.

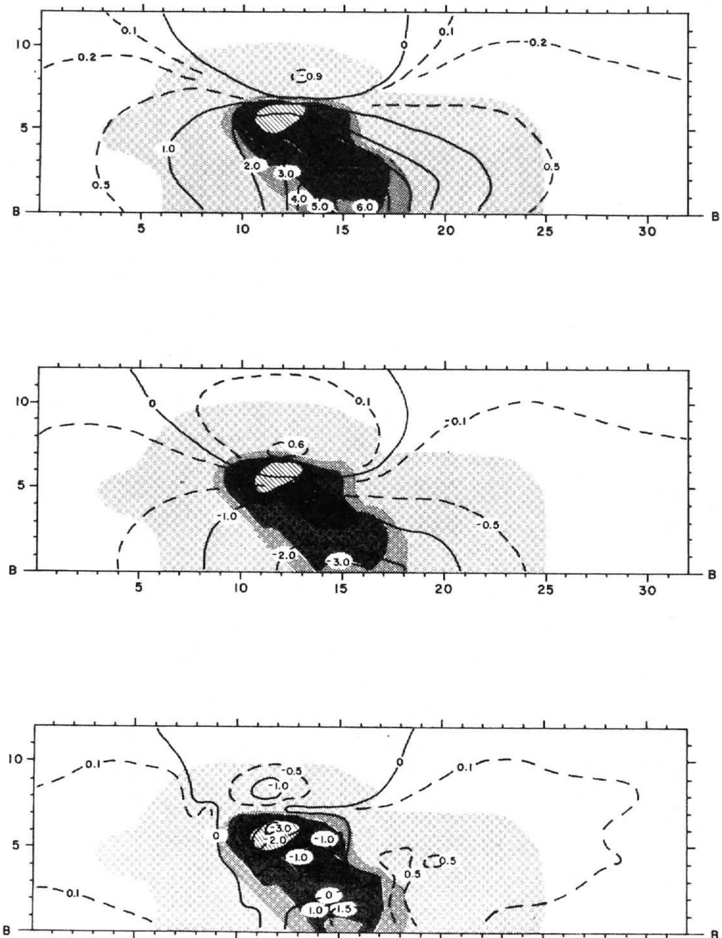

Figure 14. (top) Same as the top panel of Figure 13, except the view is through BB (large cell), and the greatest area of LWC concentration is depicted by cross-hatching.

(middle) Same as top panel of this diagram, except the analysis is of the pressure buoyancy force.

(bottom) Same as the top panel of this diagram, except the analysis is of the net vertical acceleration.

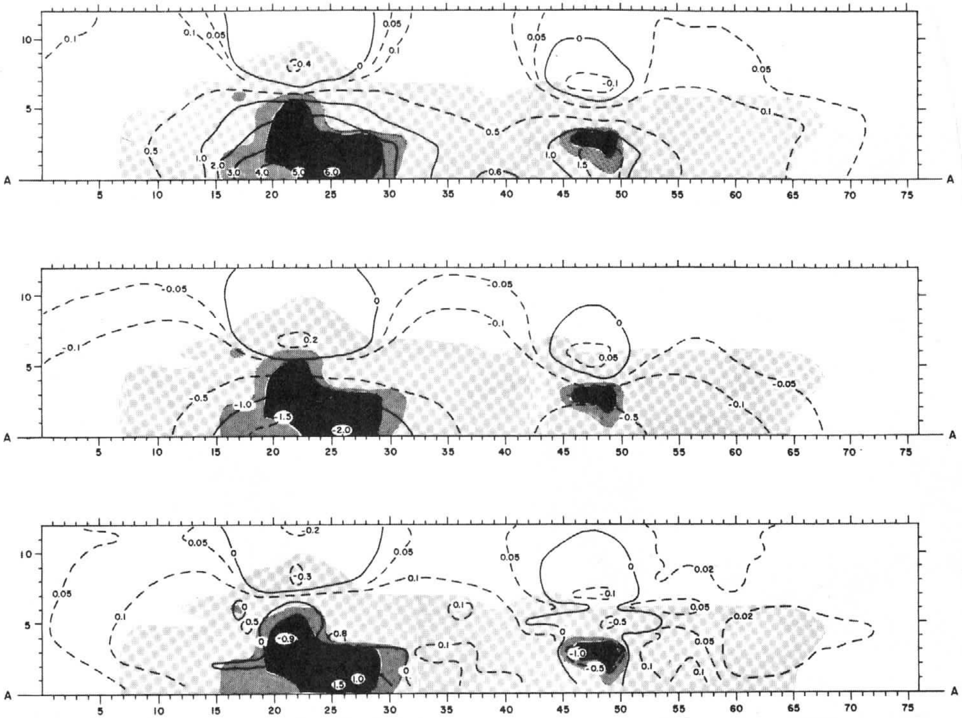

Figure 15. (top) Same as Figure 13 (top), except the view is east-west through AA (both cells). The left side of the figure is west.

(middle) Same as the top panel of this diagram, except the analysis is of the pressure buoyancy force.

(bottom) Same as the top panel of this diagram, except the analysis is of the net vertical acceleration.

a positive direction (upward) until the latter force also changes sign. But the drag force (always negative) is still relatively large throughout the layer. The effect is to produce a secondary maximum (negative) in the vertical acceleration. The primary maximum is more predictably coincident with the maximum drag force.

The complicated three-dimensional organization of convection dynamics is best illustrated by comparing slab and plan views of the vertical accelerations. A readily identifiable feature of the three-dimensionality is quite prominent at the bottom of the main cell (compare Figures 9, 14 and 15). The cell is noticeably tilted upstream relative to the ambient flow (see Figure 8). Although the drag due to the weight of the liquid water is relatively large at the base, the horizontal and vertical pressure gradients combine predominantly to produce accelerations reminiscent of a moderately strong updraft on the leading edge and two weaker downdrafts on the trailing side. This orientation of suggested updrafts and downdrafts is also reminiscent of the expected case for a cumulonimbus where not only a liquid-water drag but also a thermal buoyancy is present (see e.g., Ludlam, 1963). The similarity in form between the thermal contribution to the buoyancy and the liquid-water drag was discussed in Section 2 where the drag force was seen to be about 30% of the thermal buoyancy force near the base of the updraft. However, these two forces are opposed at the base of the cloud. In the case being considered here, a negative drag force evoked a pressure response such that an updraft was created. If temperature contrasts had been included, the influence of thermal buoyancy would have been partially compensated by the drag force. This strongly suggests that the net vertical accelerations, which are strong in the updraft base, would have been largely the result of the three-dimensional contributions of dynamic pressure forces.

5. Concluding Remarks

Summary

A first attempt has been made to particularize the three-dimensional effects of pressure and pressure forces on convection dynamics. The procedure evolved as follows. A realistic distribution of liquid-water content in a typical two-cell, deep convective system was arrived at through a conversion method using digitized radar data. The LWC values were used to force a solution for pressure of a partial differential equation which was a form of the anelastic balance equation. Sequential overrelaxation was employed. While the solution was not unique, it was shown that, through computation of the relevant forces, the resultant accelerations productively illuminated the dynamics of the implied convection.

The result of this attempt was a partial pressure field, exclusively a response to a drag force. Therefore, only a qualitative discussion of the general properties of convection dynamics could be made. Nevertheless, useful descriptions were possible due to the similarity in form between thermal buoyancy and the drag due to the weight of liquid water. In particular, the three-dimensionality of the acceleration fields was seen to be exceedingly intricate. This feature was largely contributed to the combined effects of the horizontal and vertical pressure forces.

Outlook

The direction of future research is clear. Improving and generalizing the techniques used in this study, a time-dependent investigation of the full "life cycle" of a storm system should be made. Time dependence would be handled in an implicit manner. The resolution of incremental changes of time would be limited only by the frequency with which the storm area was scanned by the radar.

Conceivably, a tornadic storm could be treated similarly. The limitation here is the usual great bulk of the parent storm. In order to attain the necessary resolution to permit the dynamic contributions to the pressures to be detected above the greater magnitude of the hydrostatic parts, interpolation between successive positions of the radar beam is necessary. The three-dimensional array so obtained may be too large to practicably "fit" into any existing computer. For the relatively small storm system investigated here, and the relatively coarse resolution of 1 n. mile, the final pressure field was included in an array exceeding 33,000 data points. (Note that two arrays, not necessarily equal because of zero data values, must be stored in the computer to solve the balance equation by relaxation.)

It would also be desirable to include perturbation temperatures. After the approach of Mount (1960), a first approximation to a temperature distribution is obtainable by assuming the air is heated to an amount proportional to $\rho_L L$ where L is the latent heat of condensation.

Finally, as an information input to conventional prognostic models, diagnostic studies of this sort can provide an invaluable service. Because of their compactness, the one-dimensional models are attractive candidates for incorporating mesoscale convection within larger, general circulation models. The present study indicates, as a first step, that parameterizations for parcel-environmental interactions must adequately allow for dynamic pressure fluctuations and that these parameterizations of three-dimensional systems will be quite complex.

ACKNOWLEDGMENTS

The authors wish to thank Dr. Frank S. Sechrist for his patient reviewing and his helpful comments. The National Severe Storms Laboratory (NSSL) at Norman, Oklahoma, generated significant impetus to this study through its provision of digitized radar data. We are, in particular, appreciative to J. T. Dooley and K. E. Wilk for a number of very helpful telephone conversations we shared during the data-conversion phase.

Finally, for what is recognized to be a vital element of this study, we sincerely thank students Leonard Hall, Ronald Dobosy, and David Barber for many hours of idea-yielding debate with one of us (R.D.A.).

Financial support was provided by the National Oceanic and Atmospheric Administration (NOAA) under Grant 1-36036 to the Space Science and Engineering Center (SSEC) at the University of Wisconsin, Madison, and by the National Science Foundation under Grant GA-30676.

Bibliography

Arnason, G., R. S. Greenfield, and E. A. Newburg, 1968: "A Numerical Experiment in Dry and Moist Convection Including the Rain Stage," J. Atmos. Sci., 25, 404-415.

Atlas, D., 1963: "Radar Analysis of Severe Storms," Meteorological Monographs, 5, No. 27, 177-223.

__________, 1964: "Advances in Radar Meteorology," Advances in Geophysics, 10 Academic Press, New York and London, 318-468.

Batton, L. J., 1959: Radar Meteorology, The University of Chicago Press, Chicago and London, 161 pp.

Dutton, J. A., and G. H. Fichtl, 1969: "Approximate Equations of Motion for Gases and Liquids," J. Atmos. Sci., 26, 241-254.

Fletcher, N. H., 1966: The Physics of Rainclouds, Cambridge University Press, London, 390 pp.

Hess, S. L., 1959: Introduction to Theoretical Meteorology, Holt, Rinehart, and Winston, New York, 362 pp.

Kerker, M., P. Langleben, and K. L. S. Gunn, 1951: "Scattering of Microwaves by a Melting, Spherical Ice Particle," J. Met., 8, 424.

Kessler, E., 1969: "On the Distribution and Continuity of Water Substance in Atmospheric Circulations," Meteorological Monographs, 10, No. 32, 26-29.

List, L., and P. Lozowski, 1970: "Pressure Perturbations in Convective Clouds," J. Atmos. Sci., 27, 168-170.

Ludlam, F. H., 1963: "Severe Local Storms: A Review," Meteorological Monographs, 5, No. 27, 1-32.

Marshall, J. S., and W. McK. Palmer, 1948: "The Distribution of Raindrops with Size," J. Meteor., 5, 165-166.

Mason, B. J., 1971: "Radar Studies of Clouds and Precipitation," The Physics of Clouds, Oxford University Press, London, 671 pp.

Mount, W. D., 1960: "An Investigation of the Liquid Water Content, Nonadiabatic Heating, and Vertical Accelerations within a Shower Using Radar Measurements," Proceedings of the Eighth Weather Radar Conference, Boston, Amer. Meteor. Soc., 287-297.

Ogura, Y., 1963: "The Evolution of a Moist Convective Element in a Shallow, Conditionally Unstable Atmosphere: A Numerical Calculation," J. Atmos. Sci., 20, 407-424.

__________, and N. A. Phillips, 1962: "Scale Analysis of Deep and Shallow Convection in the Atmosphere," J. Atmos. Sci., 19, 173-179.

Saunders, P. M., and F. C. Ronne, 1963: "A Comparison Between the Height of Radar Echoes Received from Them," J. Appl. Meteor., 1, 296-302.

Simpson, J., and V. Wiggert, 1969: "Models of Precipitating Cumulus Towers," Mon. Wea. Rev., 97, 471-479.

__________, __________, 1971: "1968 Florida Cumulus Seeding Experiment: Numerical Model Results," Mon. Wea. Rev., 99, 87-118.

Takeda, T., 1965: "The Downdraft in Convective Shower-Cloud under the Vertical Wind Shear and its Significance for the Maintenance of Convective Systems," J. Met. Soc. Japan, 44, 1-11.

__________, 1966: "The Downdraft in the Convective Cloud and Raindrops: A Numerical Computation," J. Met. Soc. Japan, 44, 1-11.

Wilk, K. E., and E. Kessler, 1970: "Quantitative Radar Measurement of Precipitation," Meteorological Monographs, 11, No. 33, 315-329.